National Library of Canada
Bibliothèque nationale du Canada

Canadian Theses Service
Service des thèses canadiennes

Ottawa, Canada
K1A 0N4

NOTICE

The quality of this microform is heavily dependent upon the quality of the original thesis submitted for microfilming. Every effort has been made to ensure the highest quality of reproduction possible.

If pages are missing, contact the university which granted the degree.

Some pages may have indistinct print especially if the original pages were typed with a poor typewriter ribbon or if the university sent us an inferior photocopy.

Previously copyrighted materials (journal articles, published tests, etc.) are not filmed.

Reproduction in full or in part of this microform is governed by the Canadian Copyright Act, R.S.C. 1970, c. C-30.

AVIS

La qualité de cette microforme dépend grandement de la qualité de la thèse soumise au microfilmage. Nous avons tout fait pour assurer une qualité supérieure de reproduction.

S'il manque des pages, veuillez communiquer avec l'université qui a conféré le grade.

La qualité d'impression de certaines pages peut laisser à désirer, surtout si les pages originales ont été dactylographiées à l'aide d'un ruban usé ou si l'université nous a fait parvenir une photocopie de qualité inférieure.

Les documents qui font déjà l'objet d'un droit d'auteur (articles de revue, tests publiés, etc.) ne sont pas microfilmés.

La reproduction, même partielle, de cette microforme est soumise à la Loi canadienne sur le droit d'auteur, SRC 1970, c. C-30.

NL-339 (r. 88/04)

Canada

THE UNIVERSITY OF ALBERTA

THE USE OF ELECTRON ENERGY-LOSS SPECTROSCOPY FOR MICROCHARACTERIZATION OF THIN SPECIMENS

by

© SHANG-CONG CHENG

A THESIS

SUBMITTED TO THE FACULTY OF GRADUATE STUDIES AND RESEARCH
IN PARTIAL FULFILMENT OF THE REQUIREMENTS FOR THE DEGREE
OF DOCTOR OF PHILOSOPHY

DEPARTMENT OF PHYSICS

EDMONTON, ALBERTA
FALL 1987

ISBN 0-315-41056-6

THE UNIVERSITY OF ALBERTA

RELEASE FORM

NAME OF AUTHOR SHANG-CONG CHENG

TITLE OF THESIS THE USE OF ELECTRON ENERGY-LOSS SPECTROSCOPY FOR MICROCHARACTERIZATION OF THIN SPECIMENS

DEGREE FOR WHICH THESIS WAS PRESENTED DOCTOR OF PHILOSOPHY

YEAR THIS DEGREE GRANTED FALL 1987

Permission is hereby granted to THE UNIVERSITY OF ALBERTA LIBRARY to reproduce single copies of this thesis and to lend or sell such copies for private, scholarly or scientific research purposes only.

The author reserves other publication rights, and neither the thesis nor extensive extracts from it may be printed or otherwise reproduced without the author's written permission.

(SIGNED) S. C. Cheng

PERMANENT ADDRESS:

P. O. BOX 2724
Beijing
China

DATED June 29 1987

THE UNIVERSITY OF ALBERTA

FACULTY OF GRADUATE STUDIES AND RESEARCH

The undersigned certify that they have read, and recommend to the Faculty of Graduate Studies and Research, for acceptance, a thesis entitled THE USE OF ELECTRON ENERGY-LOSS SPECTROSCOPY FOR MICROCHARACTERIZATION OF THIN SPECIMENS submitted by SHANG-CONG CHENG in partial fulfilment of the requirements for the degree of DOCTOR OF PHILOSOPHY.

R. F. Egerton
Supervisor

J. A. Kernahan

J. C. H. Spence
External Examiner

Date June 29 1987

DEDICATED TO

MY BELOVED PARENTS

Abstract

Electron energy loss spectroscopy (EELS) studies the energy distribution of electrons that have been transmitted through a thin sample. The kinds of information which can be obtained from this study are presented. Basic instrumentation for EELS experiments is outlined, with emphasis on the avoidance of experimental artifacts.

The inner-shell ionization edges in EELS are normally used to identify the presence of particular elements. Experiments were performed to investigate the effect on the signal/background ratio of the collection aperture and the thickness of the specimen. The results show that the core-edge signal/background ratio is increased by using dark-field illumination and thicker samples only in the case where the instrumental background is high. It appears more attractive to work under bright-field conditions and reduce the instrumental background to a low level by optimizing the design of the electron detector.

The low-loss region in EELS can be used to measure the mean free path of fast electrons in a solid. Experimental results for the mean free paths of several materials are presented, together with theoretical calculations based on atomic and plasmon models.

The thickness of a thin film is often required in microcharacterization. A method based on a Kramers-Kronig

sum rule is outlined; theory and experiments related with this method are presented in detail. The accuracy of this sum rule technique is estimated to be ±10% over the thickness range 10-150 nm. The method requires no knowledge of the physical or chemical properties of the specimen other than its refractive index. It involves only a low radiation dose, allowing good lateral resolution (<10 nm) to be achieved even by selected-area techniques.

Acknowledgement

I wish to express my sincere gratitude to my supervisor, Professor R.F. Egerton, for his constant encouragement and guidance over the past years.

I wish to thank Drs S.S. Sheinin, P.A. Crozier, B.V. Paranjape, M.J. Brett, W. Rozmus, J.A. Kernahan and J.C.H. Spence for many helpful discussions and suggestions.

I whould like to thank Mr. J.C. Brunel for technical assistance in using the equipment in the electron microscope laboratory.

I am grateful to my wife, Shaole, for typing the thesis.

Finally, I am thankful to the Department of Physics for the award of a teaching assistantship.

Table of Contents

List of Tables

List of Figures

Figure Page

Figure Page

Figure Page

CHAPTER 1

THE MICROANALYTICAL INFORMATION FROM EELS

1.1 INTRODUCTION

During the past four decades, there has been a proliferation of new physical techniques for elemental and structural analysis, with particular emphasis on the analysis of extremely small specimen volumes with high sensitivity. These physical techniques involve bombardment of the specimen with material particles or electromagnetic radiation in order to produce particular excitations of the elements [illegible] the specimen, or to obtain quantitative information about the specimen by scattering or absorption of the incident particles or radiation. By now, all of the practical methods of bombarding a specimen with particles or radiation and all of the various signals that result from this bombardment have been explored as possible methods for microanalysis. The specimen can be bombarded by electrons, ions, X-rays, light or neutrons, and various signals consisting of electromagnetic waves, charged particles, light or sound waves can be detected. In general, one studies the energy dependence of the emission or absorption of some kind of particle or field by a selected sample material. The energy dependence reveals dynamical information about the sample. In condensed matter physics, where the sample may be inhomogeneous, it is useful to study not only the energy dependence but also the spatial dependence of the emission or absorption rates.

Figure 1.1 shows a comparison between four spectroscopies of solids: photon absorption, electrons, X-rays, and neutrons, revealing the range of energies and wave vectors accessible to each of them (Schnatterly 1979). The diagonal line represents optical absorption. It is impossible to independently vary the energy and momentum of a photon. Therefore, any excitation in a solid that is created by absorption of a photon must lie on the line shown. To move off this fixed line, a scattering experiment must be performed. A beam of particles is incident on the sample and scatters through some angle, losing a certain energy. The energy lost and the momentum transfered in the sample can be ascribed to the creation of excitation. By varying the scattering angle and the energy loss, an entire region in energy-momentum space can be studied. Inelastic neutron scattering is the most powerful technique for the low-energy range (<0.1 eV). On the other hand, inelastic X-ray scattering is well suited to study high momentum and large energy transfers because the energy resolution is limited to ≃ 1 eV and the cross-section increases with the momentum transfer. Inelastic electron scattering is nicely complementary to all of the above techniques since the range in energy-momentum space which can readily be covered

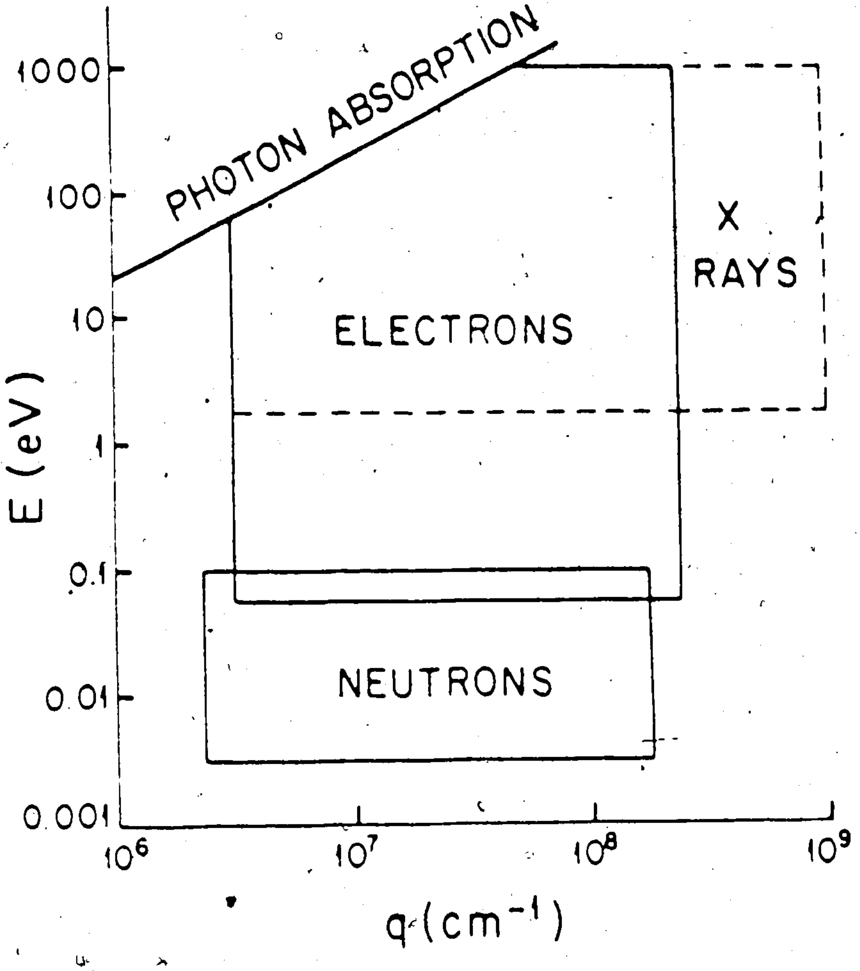

Fig. 1.1. Regions in E, q space accessible to different experimental probes presently available.

overlaps each of their regions.

Electron energy loss spectroscopy (EELS) is the study of the energy distribution of inelastic scattered electrons. In EELS, all the information that can be obtained about the specimen is contained in the angular and energy distribution of the electrons that have passed through it, as shown in Fig. 1.2. By studying this distribution, which results from interaction between the electrons and the specimen, and analyzing it in terms of an appropriate model, the required information can be found.

The most general way to characterize these interactions is to measure the momentum changes suffered by the electrons as they pass through the sample. This is done by measuring both the angle θ through which an electron is scattered, and E, the change in energy relative to the incident energy E_o (Fig. 1.2). Usually, however, it is sufficient to collect all the transmitted electrons lying within a cone of some angular width β about the incident-beam direction, and to analyze these for their energy loss. Although this approach destroys information about the momentum transfer, since the spectrometer is now integrating information from the whole angular range which it is accepting, it is the one most generally used. The information produced can be readily related to the important properties of the material by simple mathematical models of the interactions. The result obtained from such an experiment is an electron energy-loss

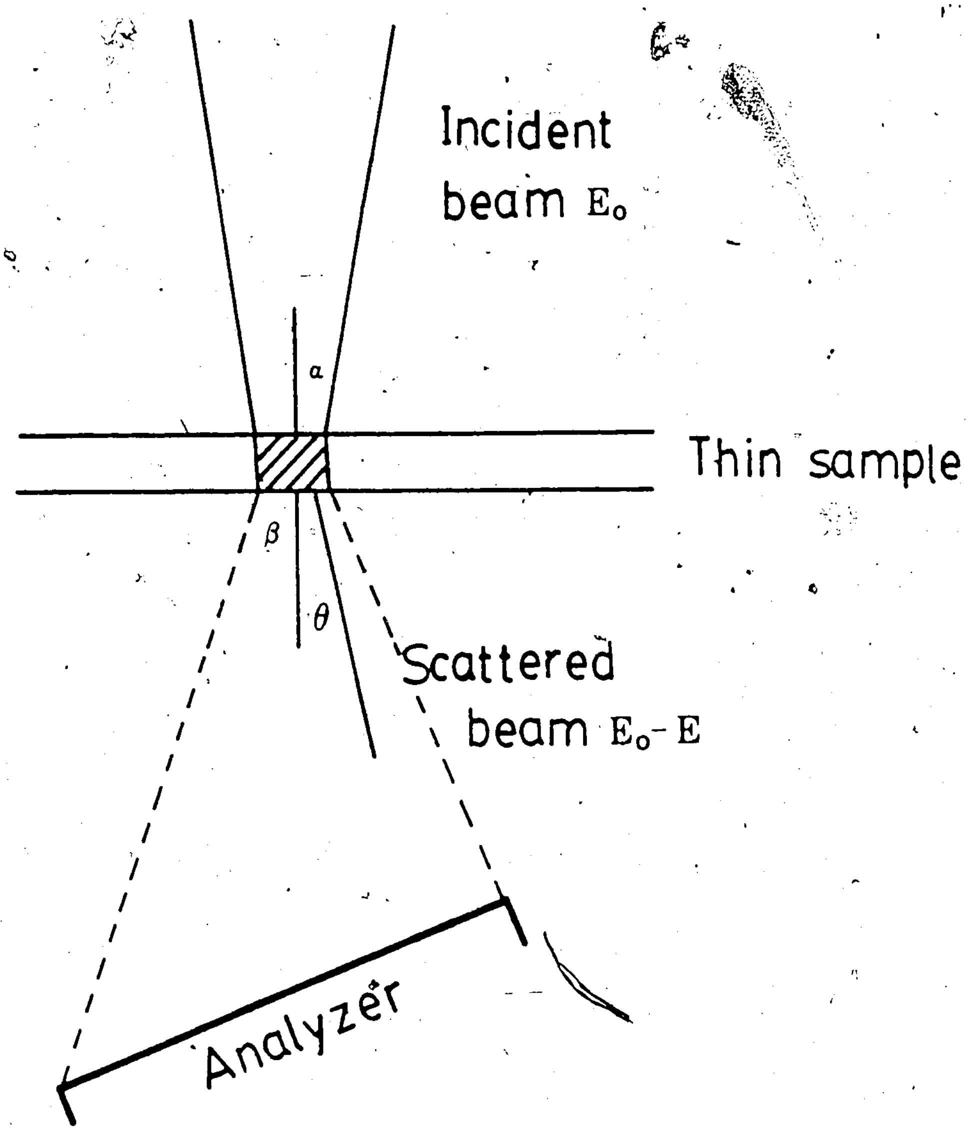

Fig. 1.2. The geometry of EELS in the electron microscope, illustrating the scattering angle θ, the spectrometer collection angle β and the incident beam convergence angle α.

spectrum, in which the transmitted signal intensity J(E) is plotted as a function of the energy loss E for all the electrons scattered within the angular cone β accepted by the spectrometer.

Typical electron energy loss spectra recorded from a thin foil of carbon using 80 keV incident electrons and with β = 10 mrad and 100 mrad, respectively, are shown in Fig. 1.3. The spectrum can be divided into the following three parts.

(1) There is a large maximum in the intensity centered at E = 0, which is usually called the 'zero-loss peak'.

(2) There are one or more peaks in a region extending from the edge of the zero-loss peak out to about 50-100 eV, which is conveniently called the 'low-loss' region.

(3) The region lying above ~50-100 eV is the high-loss region, having the general form of a rapidly falling 'background' on which are superimposed edges with various features.

The following sections will consider each part separately and discuss what useful analytical information it can yield.

1.2 THE ZERO-LOSS PEAK

As shown in Fig. 1.3, one of the important features of EELS spectra is the large maximum in the intensity centered at E = 0. Since the electron spectrometer has definite energy resolution and the incident electron beam itself has an inherent energy spread of 0.5 eV to 1.5 eV arising both from the natural energy width of the electron source and from the instabilities in the accelerating potential, the zero-loss peak has a finite energy width. The resolution of the electron energy-loss spectra is indicated by the width of the zero-loss peak.

There are three groups of electrons contributing to a zero-loss peak. One group is the unscattered electrons, these having passed through the sample without any interaction. Because they have not interacted with the specimen, they can carry no information about the sample and are no use in microanalysis. The second group is the elastically scattered electrons deflected by the nuclear charge of an atom. The elastic electrons are of limited use in the microanalysis. However, if we collect them over a sufficiently wide angular range, the elastic cross section becomes approximately proportional to $Z^{3/2}$ where Z is the atomic number (Joy 1979). This strong dependence on the atomic number makes possible an analysis of samples. Because the total signal from the inelastically scattered electrons varies as $Z^{1/2}$, the ratio of these two signals is proportional to the mean atomic number $\bar{Z}$. After calibration with a suitable standard, this technique can be used for microanalysis (Egerton et al. 1975). It has also been used for imaging and identification of single atoms (Crewe et al.

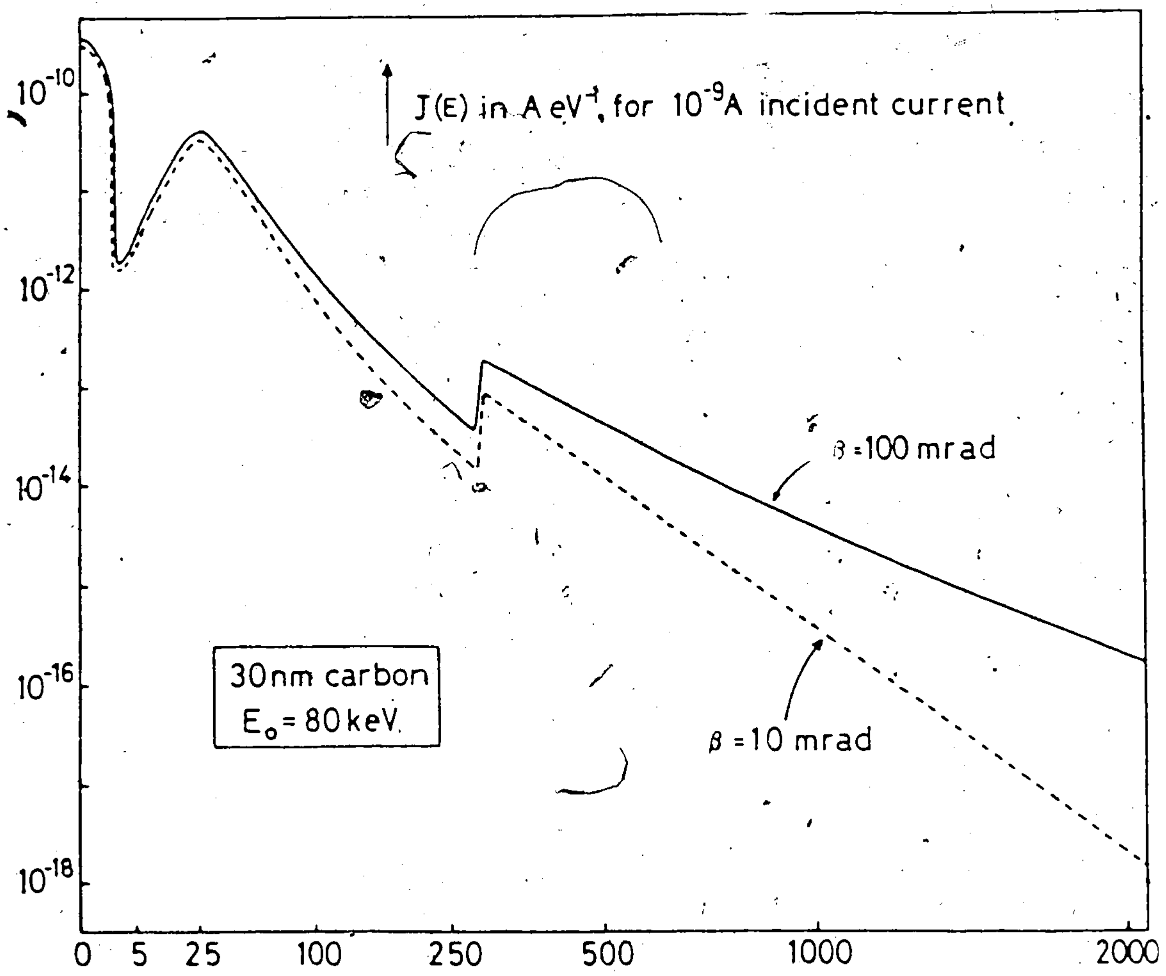

Fig. 1.3. Energy loss spectra of carbon obtained with an 80 keV incident beam and two values of β.

1975, Isaacson et al. 1979). The third group of electrons in the zero-loss peak are those that have generated phonon excitation. Phonons are vibrations of the lattice in the sample. The energy losses of electrons caused by phonons have a broad angular distribution which is centered around each Bragg diffracted beam.

The zero-loss peak of EELS is important because it provides an energy reference for the spectrum, gives a measure of the resolution of spectrometer and also provides the normalization factor required for quantitative microanalytical calculations.

1.3 LOW-LOSS REGION

The energy losses in this region are due to the interactions of incident electrons with the valence or conduction electrons in the sample. When individual atoms condense to form a solid, there is considerable rearrangement of their valence electrons, which results in binding the individual atoms together. The valence electrons may be quite localized, as in the homopolar bond and in ionic crystals; or they may wander through the entire solid as nearly free electrons in a metal. In any case, they behave in a manner which appears as a collective or wave excitation when struck by a fast, incident electron. The collective or wave excitation is called a plasmon. There is an angular frequency ω_p and excitation quantum $E_p = \hbar\omega_p$ associated with the collision where $\hbar = h/2\pi$ and h is Planck's constant. The frequency of oscillation ω_p is proportional to $n_e^{1/2}$ where n_e is ~~the number~~ of free electrons per cm^3 involved in the oscillation. Because the plasmon energy loss depends on the free electron density, it can be used to identify the material (Kunz 1966, Kloos 1973, Chen 1976). Unfortunately, materials showing sharp plasmon peaks may have similar values of E_p, so that the measured value is not unique to any one metal or alloy. However, shifts in the plasmon peak position can be used to monitor the change in concentration of one element in an alloy. As an example, Fig. 1.4 shows the sequence of spectra taken stepping across the interface between Al and AlF_3 (Isaacson and Scheinfein 1985). In this graph the aluminum metal side of the interface is denoted by the negative distances whereas the AlF_3 side of the interface is marked by the positive distances. The bulk plasmon of aluminum metal is indicated by 'a' and occurs at 15 eV. The surface plasmon of aluminum is indicated by 'b' when it occurs on the aluminum metal side and by 'c' on the AlF_3 side of the interface. The experimental results show that it is possible to detect significant changes in the electron energy-loss spectrum at a spatial resolution of better than 0.8 nm as the probe is moved across an aluminum-aluminum fluoride interface. The localization distance of plasmons obtained from this

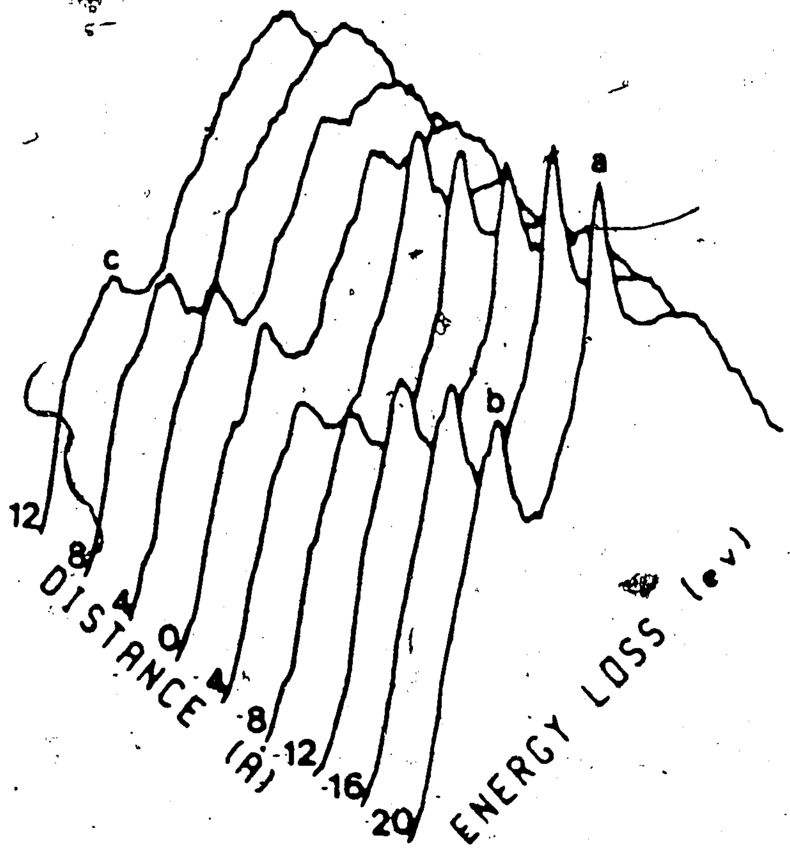

Fig. 1.4. Stepped sequence of energy loss spectra taken as the probe is moved across the Al-AlF_3 interface. The positive distances are in the AlF_3 and the negative distances are in the Al. Peak 'a' is the bulk plasmon of Al metal. Peak 'b' is the Al surface plasmon coupled to the underlying carbon film. Peak 'c' is the Al surface plasmon in AlF_3 which is shifted in energy from 'b' due to a change in dielectric constant across the interface.

experiment was compared with theoretical calculation; the experimental and theoretical results are in good agreement (Cheng 1987).

The low-loss region of EELS can also be used to measure the mean free path of fast electrons in matter. The experimental method and the theoretical calculations can be found in Chapter 4.

In addition, the spectrum in the low-loss region provides the information of the imaginary part of dielectric function. By using Kramers-Kronig analysis, the surface loss intensity present in a recorded low-loss spectrum can be found and the absolute local thickness of a sample can be measured (Egerton and Cheng 1987). This method is based on the Kramers-Kronig sum rule and is discussed in Chapter 5.

1.4 HIGH-LOSS REGION

As shown in Fig. 1.3 the spectrum in this region has the general form of a smoothly falling 'background' on which are superimposed the inner-shell 'ionization edges'. This portion of the EELS spectrum is the most important one for microanalysis because the ionization energy of an edge is a unique property of an element (Ahn and Krivanek 1983).

The 'background' contains no microanalytical information but is a dominant feature of the spectrum. It comes from a variety of effects such as excitations from valence states to vacuum and multiple plasmon losses. In a multi-element system, each successive edge will contribute to the background intensity of the edges that follow at higher energy losses. Because of this complexity no formula derived from theory is available to compute the background; but a method has been found which subtracts the background from the experimental spectrum (Egerton 1975, Maher 1979).

The 'characteristic edges' contain the elemental information. Each edge represents the energy loss associated with the ionization of an electron from a particular inner shell of a particular type of atom. An energy loss measurement can therefore be used to identify the chemical components of the sample. The advantage of using EELS for the detection of light elements has been well demonstrated. Low fluorescence yield and poor collection efficiency make the conventional X-ray microprobe technique insensitive for elements with low atomic number. In contrast, the efficiency for detecting inner shell ionization events by EELS is high and the K and L shell cross sections for the lighter elements are particularly favorable (Hall and Gupta 1983). Since the 'ionization edges' are set on a relatively high background, finding the experimental condition which improves the ratio of signal to background is an important task in microanalytical work. The theory and the experiments related to this subject are discussed in Chapter 3.

A close inspection of the ionization edges in electron energy loss spectra reveals a wide variety of shapes and structures, both near the edge and as far as several hundred volts away from the edge. Two other kinds of information can be obtained from these fine structures. The 'pre-ionization fine structure' is the form of density of unoccupied bound states into which the ionized electron can be placed. The 'extended fine structure' is a weak oscillatory structure extending for many hundreds of electron volts away from the edge. These oscillations occur because the electromagnetic wave produced by the ionization for some energy loss has a wavelength which is of the same order as an atomic spacing. The wave can be diffracted by neighboring atoms and return to interfere with the outgoing wave. An analysis of this fine structure provides important information about atomic arrangements, especially for amorphous material. The topic of the fine structure is discussed in detail in many references (Spence 1985, Leapman 1982, Disko 1981, Egerton and Whelan 1974, Isaacson 1972); it is not, however, involved in the present work.

CHAPTER 2

INSTRUMENTATION

A typical EELS system, used to obtain information on the elemental composition or structure of a specimen, consists of the following components: an electron source, a suitable sample of material to be studied, a spectrometer for analysing the energy of the transmitted electrons, a detector and a spectrum storage/display system (Fig. 2.1). In general, these components can take a variety of different forms but we are mainly interested in an experimental arrangement which is compatible with the operation of a conventional transmission electron microscope (CTEM).

In this chapter, an overall description of experimental instrumentation is given. The description is in four sections, dealing with: (1) the JEM-100B Electron Microscope, (2) the electron spectrometer designed in the Department of Physics, the University of Alberta, and the commercial Gatan Electron Energy Loss Spectrometer, Model 607, (3) the system for recording and analysing data, (4) a standard vacuum system for sample preparation.

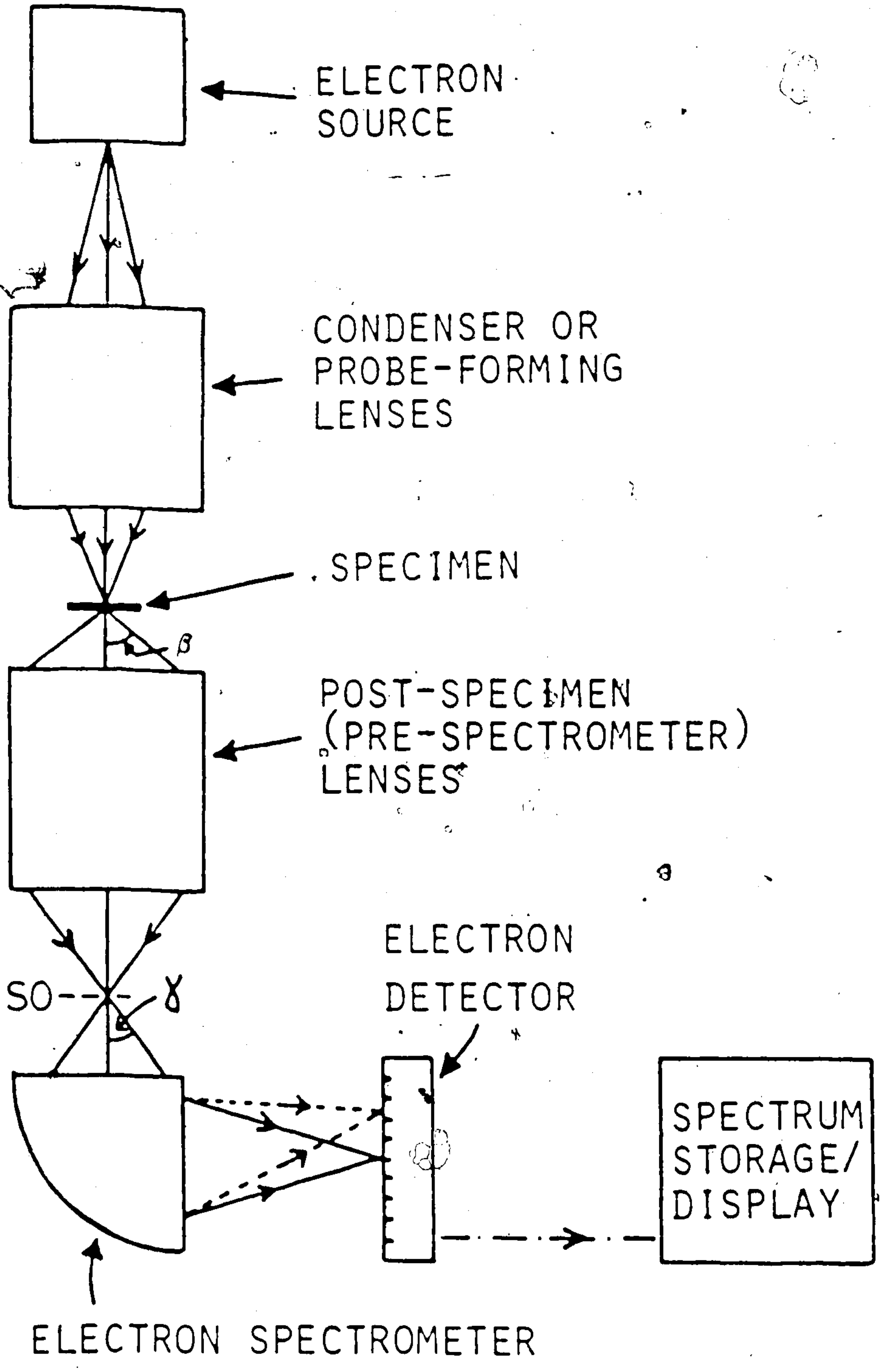

Fig. 2.1. Typical EELS system (Egerton 1982).

2.1 JEM-100B ELECTRON MICROSCOPE

Experiments described in this thesis were carried out using a JEM-100B Electron Microscope on which a spectrometer described in the next section was fitted. Figure 2.2 is the column cross section of JEM-100B. A fine beam is produced by heating a filament of tungsten wire, which emits a few tenths of a milliampere; these electrons are then accelerated through a potential difference of 20-100 kV. The combination of a filament and accelerating electrodes is known as an electron gun. The electrons then pass through two condenser lenses, with which the operator can control the size and angular spread of the beam. Since the specimen located behind the condenser lenses and immediately before the objective lens is usually thin, most electrons pass through the specimen and enter the objective lens. Within the objective lens lies a small aperture, made of a metal disc with a central hole 20-60 μm pierced in it. Electrons that have been deflected through sizable angles by the specimen will hit the wall of the aperture; only electrons that have been deflected through very small angles will pass through the aperture and continue to pass along the microscope. Beyond the objective lens the electrons pass through three magnifying lenses, two intermediate and one projector, and finally fall onto either a fluorescent screen or a photographic plate.

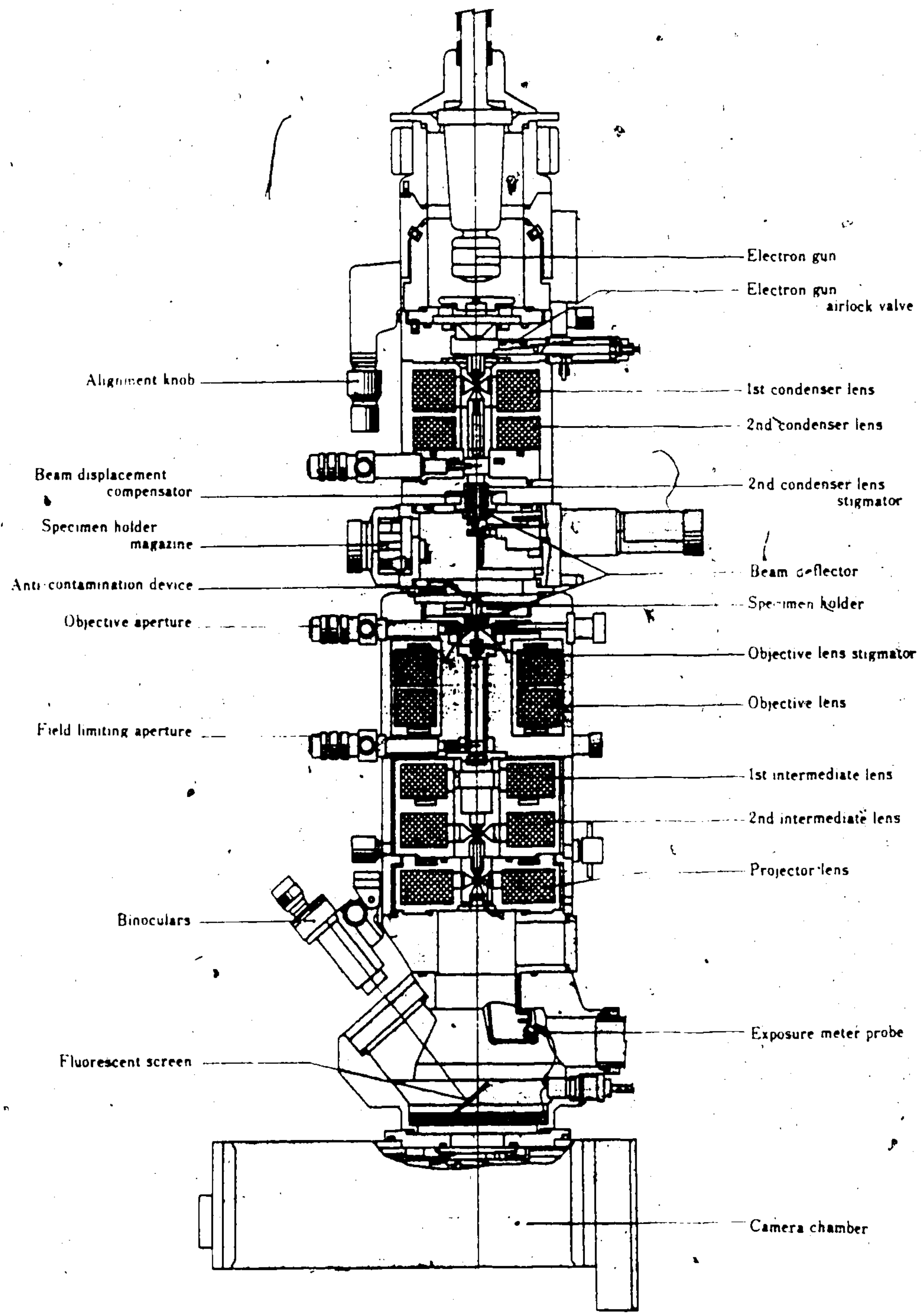

Fig. 2.2. Column cross section of JEM-100B Electron Microscope.

In the present experiments, the maximum scattering angle, limited by the objective aperture β, was measured using an aluminum diffraction standard whose diffraction pattern was recorded on a photographic plate. The radius, $R_{hk\ell}$, of each ring appearing in the diffraction pattern is given by:

$$R_{hk\ell} = \frac{\lambda_e L}{d_{hk\ell}} \qquad (2.1)$$

where λ_e is the electron wavelength; L is the effective distance of the specimen from the fluorescent screen or from the photographic plate; $d_{hk\ell}$ is the distance between adjacent planes of the crystal which have diffracted the electrons and caused the rings in the diffraction pattern. The distance $d_{hk\ell}$ can be found using the relationship for cubic structures since aluminum crystalizes in cubic system, i.e.,

$$d_{hk\ell} = \frac{a}{(h^2+k^2+\ell^2)^{1/2}} \qquad (2.2)$$

where a_o is the crystal cube edge and h, k and ℓ are the Miller indices. Thus, the diffraction constant of the microscope, $\lambda_e L$ can be found by measuring $R_{hk\ell}$ directly from the diffraction pattern. The maximum scattering angle limited by the aperture, β, can then be found by means of the relationship:

$$\beta = R/L \qquad (2.3)$$

where R is the shadow radius of the objective aperture which has been superimposed on the aluminum diffraction pattern and recorded on the photographic plate. The β values reported in this thesis were all determined using this method.

The JEM-100B Electron Microscope was equipped with the EM-BLG Goniometer Stage in order to study crystalline specimens. The specimen is mounted on gimbals in the EM-BLG tilting specimen holder (Fig. 2.3). The mechanism of the system is so designed that the directions of each tilting axis coincide with the respective directions of the EM-BGS Goniometer Stage transverse control axis. With the help of the EM-BLG Goniometer Stage, the specimen can be tilted up to ±30° in any direction by the vertical displacement of two driving shafts.

2.2 ELECTRON SPECTROMETERS

After the electrons pass through the post-specimen lenses (Fig. 2.1), a selected portion of the electron distribution will pass through the collector aperture into the electron spectrometer. The function of the spectrometer is to resolve the electrons into their different energy components and to focus this spectrum into an adjustable

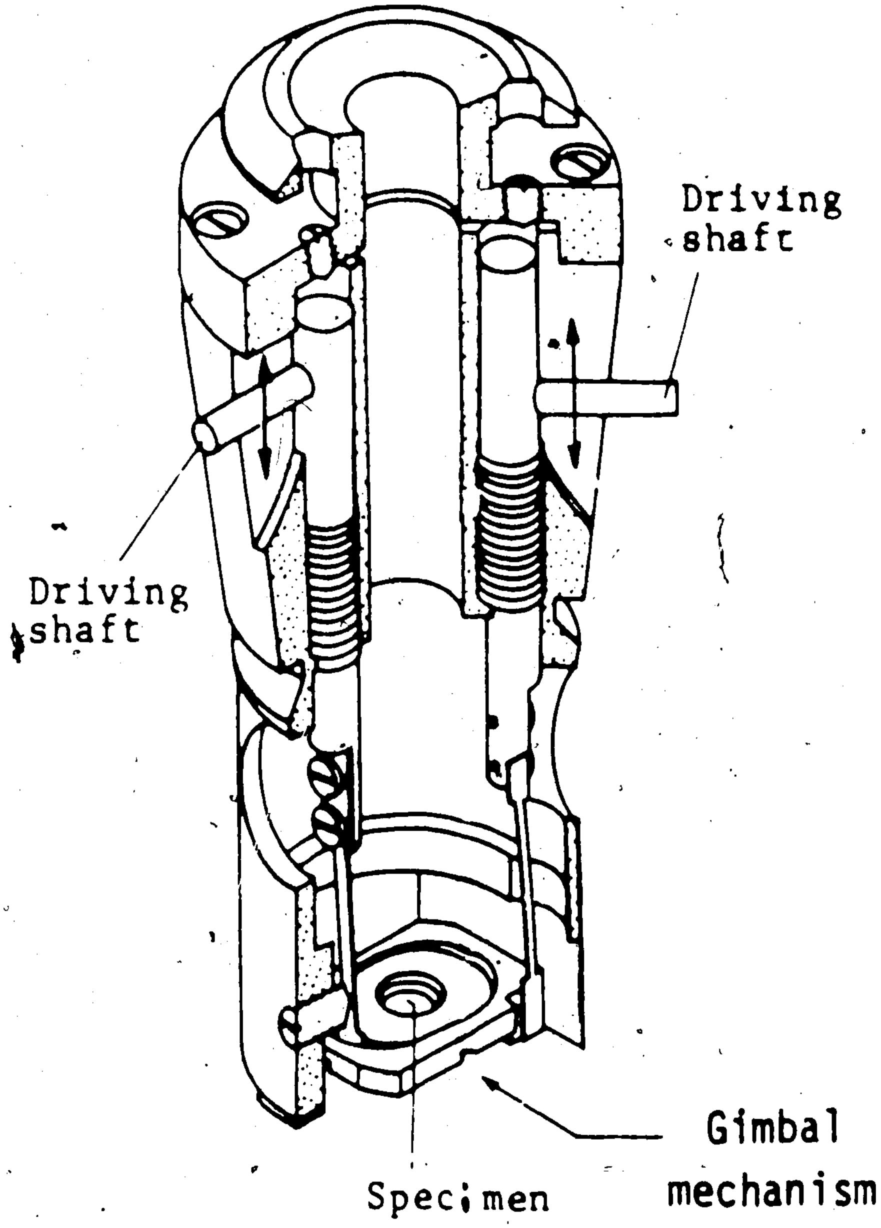

Fig. 2.3. Tilting specimen holder.

slit located in front of an electron detector.

The laboratory-made spectrometer (Egerton 1982), designed and built in the Department of Physics, the University of Alberta, was used to perform the experiments described in Chapter 3. This spectrometer was located below the viewing screen, so it was easily installed and does not impair the basic performance or ease of operation of the microscope (Fig. 2.4). The design of the spectrometer is based on a single sector magnet, in which the electron beam is bent into a circle of constant radius and dispersed into its component energies by means of a perpendicular magnetic field. Figure 2.5 shows the magnet in which the magnetic flux is generated by "window-frame" coils located in slots around each polepiece. The outside of the magnet block provides a return path for the magnetic field and shields the beam from external fields. The position of the detector slit is designed to be movable by changing the length of the focussing tube. Figure 2.6 shows the focussing tube and the slit assembly of the spectrometer which is equipped with a JEOL scintillator and photomultiplier detector system. This arrangement allows us to modify the slit easily, which was convenient when performing the experiments described in Chapter 3.

The commercial Gatan Electron Energy Loss Spectrometer, Model 607, was used to perform the experiments described in Chapters 4 and 5. This spectrometer is also of the single

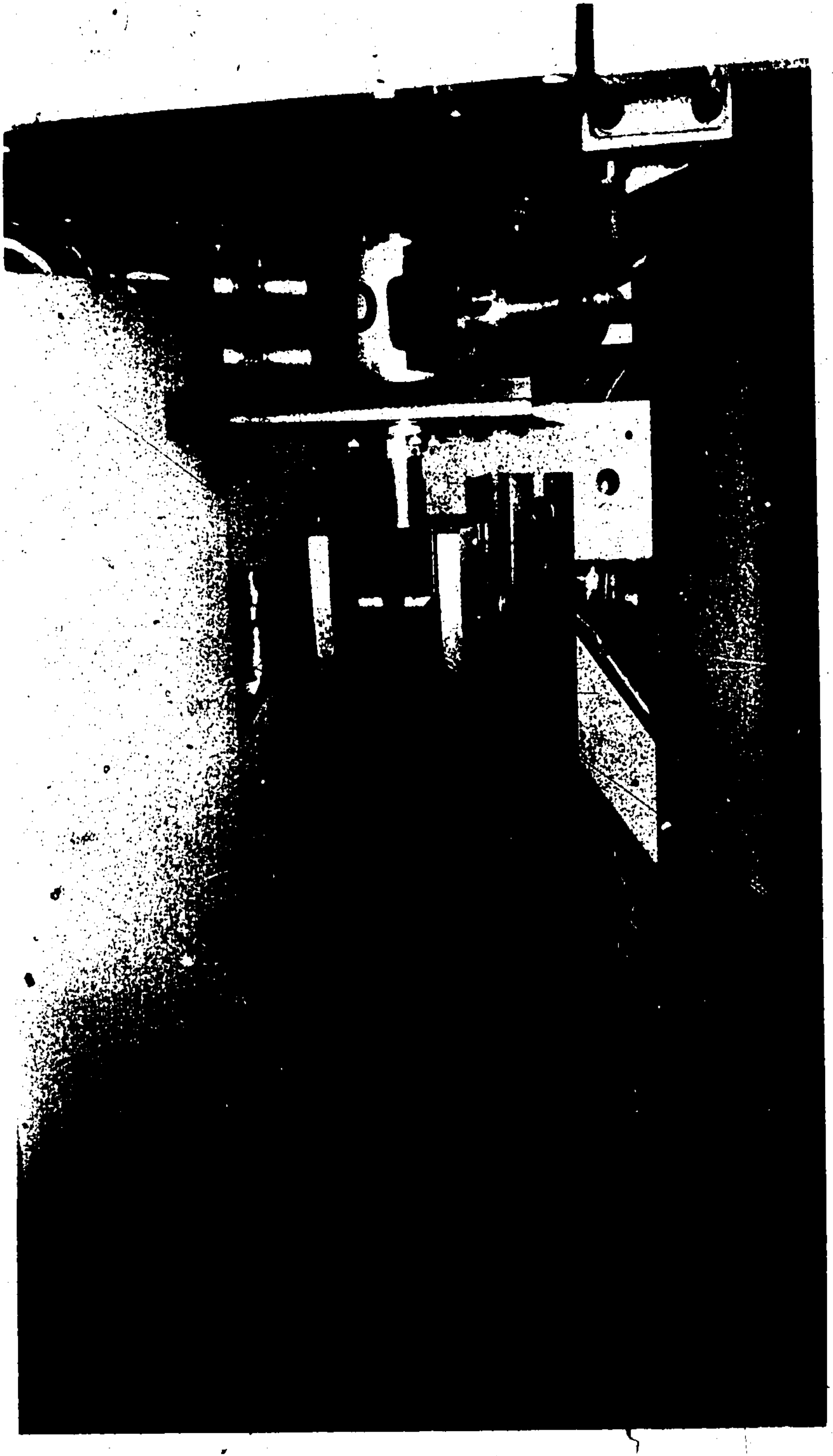

Fig. 2.4. Front view of the spectrometer. C is the camera chamber of the JEM-100B. D is the dark field detector (which is not required for energy analysis).

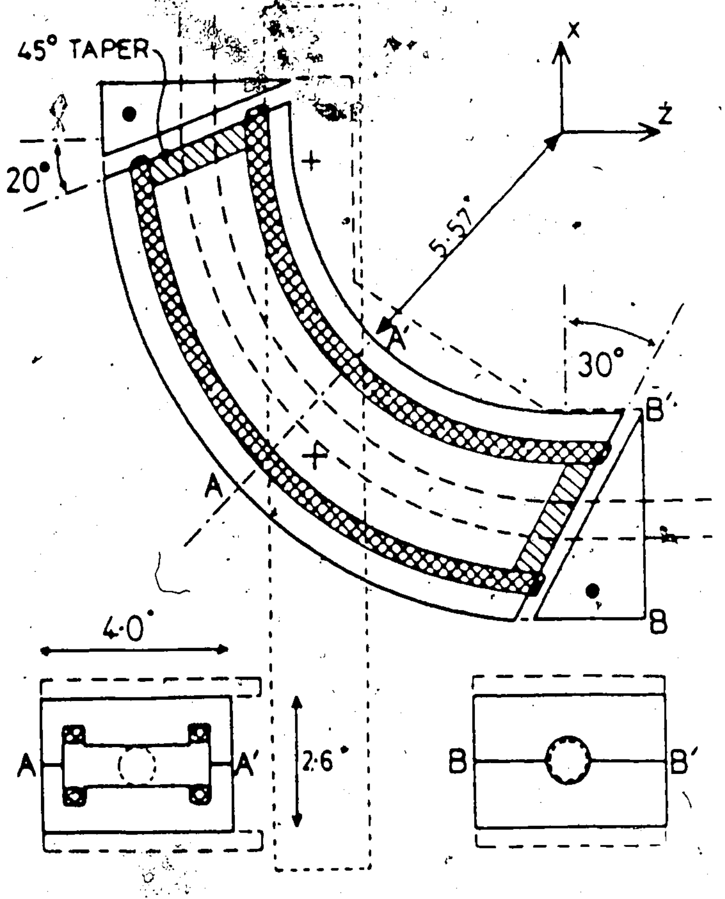

Fig. 2.5. Side view of the spectrometer. Cross sections through the magnet and field clamps are shown separately. The mounting plate, mounting girders and copper tube are outlined by dashed lines; the magnet windings appear cross hatched.

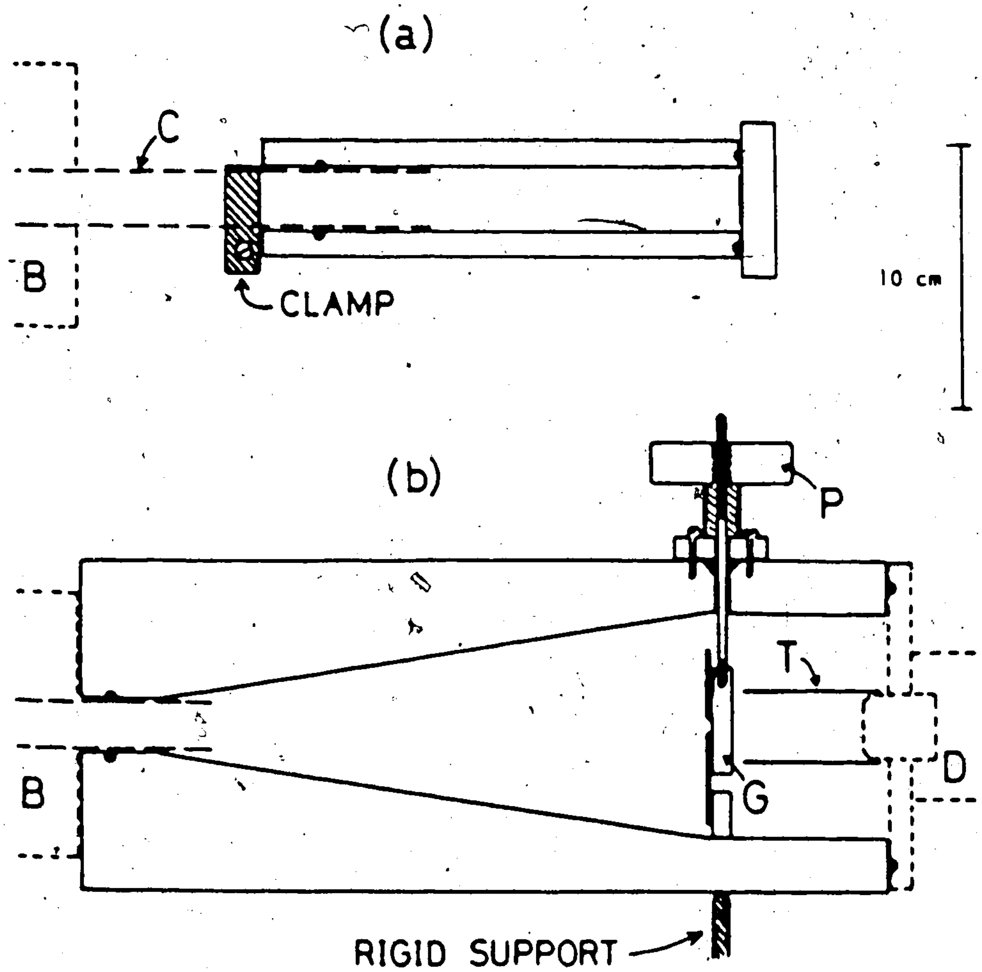

Fig. 2.6. The focussing tube (a) and the slit assembly (b) of the laboratory-made spectrometer. The exit of the spectrometer B, copper connecting tube C and JEOL detector system D are shown in broken lines.

magnetic sector type. It disperses electrons with a second-order aberration corrected magnetic prism. The important components include energy-selecting auxiliary focussing coils which fine-tune the focal properties of the prism, the electrostatically isolated drift-tube and the exchangeable entrance aperture. All the components and the accessories are shown in Fig. 2.7. Compared to other single magnetic sector spectrometers, the Gatan Electron Spectrometer, Model 607, introduces two innovations: electromagnetic focussing coils which replace the usual mechanical alignment, and a hybrid electron detection system which incorporates both single-electron counting and current measuring of the photomultiplier-tube output (Krivanek and Swann 1981). The electromagnetic focussing coils contain a dipole, two quadrupoles, and a sextupole (see Fig. 2.7). The dipole has a low inductance and is used for fast, undistorted scanning of the spectrum needed for flicker-free display of the low loss region and particularly the zero-loss peak on a videoscope display. The two quadrupoles give the two degrees of first-order focussing necessary in a magnetic spectrometer. One ensures that electrons of the same energy are focussed into a sharp line at the energy-selecting slit, the other that the line is precisely parallel to the slit. The sextupole action is similar to changing the entrance curvature of the magnetic sector. It balances one of the two important second-order aberration coefficients. In practice, these electromagnetic focussing

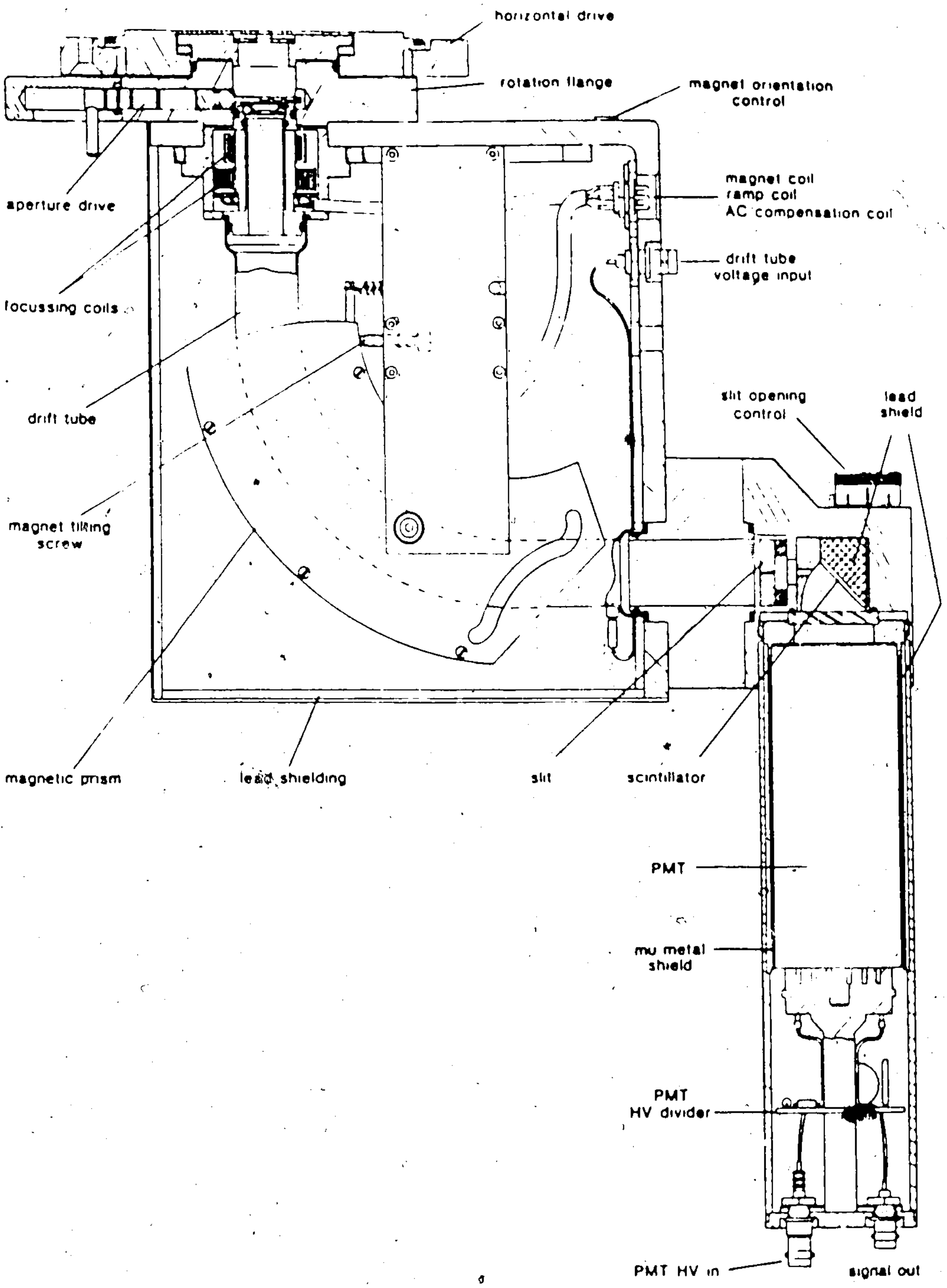

Fig. 2.7. The cross-section of Gatan Electron Energy Loss Spectrometer, Model 607.

coils ensure that the resolution of the spectrometer is limited by the third- rather than the second-order aberrations.

Like all electron-optical elements, a magnetic prism performs to its designed specifications only if it is correctly aligned relative to the incident beam of electrons. Since the energy dispersion is small for high-energy electrons, the alignment must be done carefully. The procedure of alignment and adjustment can be found from references (Egerton 1986; Gatan, Inc.).

Like many electronic devices, the spectrometer takes a certain time to warm up before it becomes stable. To minimize the influence of an unstable incident-electron beam, the spectrometer was turned on 30 minutes after the electron microscope had been turned on. The stability of the spectrometer was then tested by checking the stability of the zero-loss peak from the recorded spectrum. Figure 2.8 shows that the zero-loss intensity becomes stable after the spectrometer has been turned on for 60 minutes. Therefore, if the optimum energy resolution is required, it takes at least 60 minutes to warm up the spectrometer.

When the spectrometer is properly focused, stray magnetic fields may still degrade the resolution because these external fields may penetrate into the viewing chamber and deflect the electron beam before it enters the spectrometer. The external interference comes from

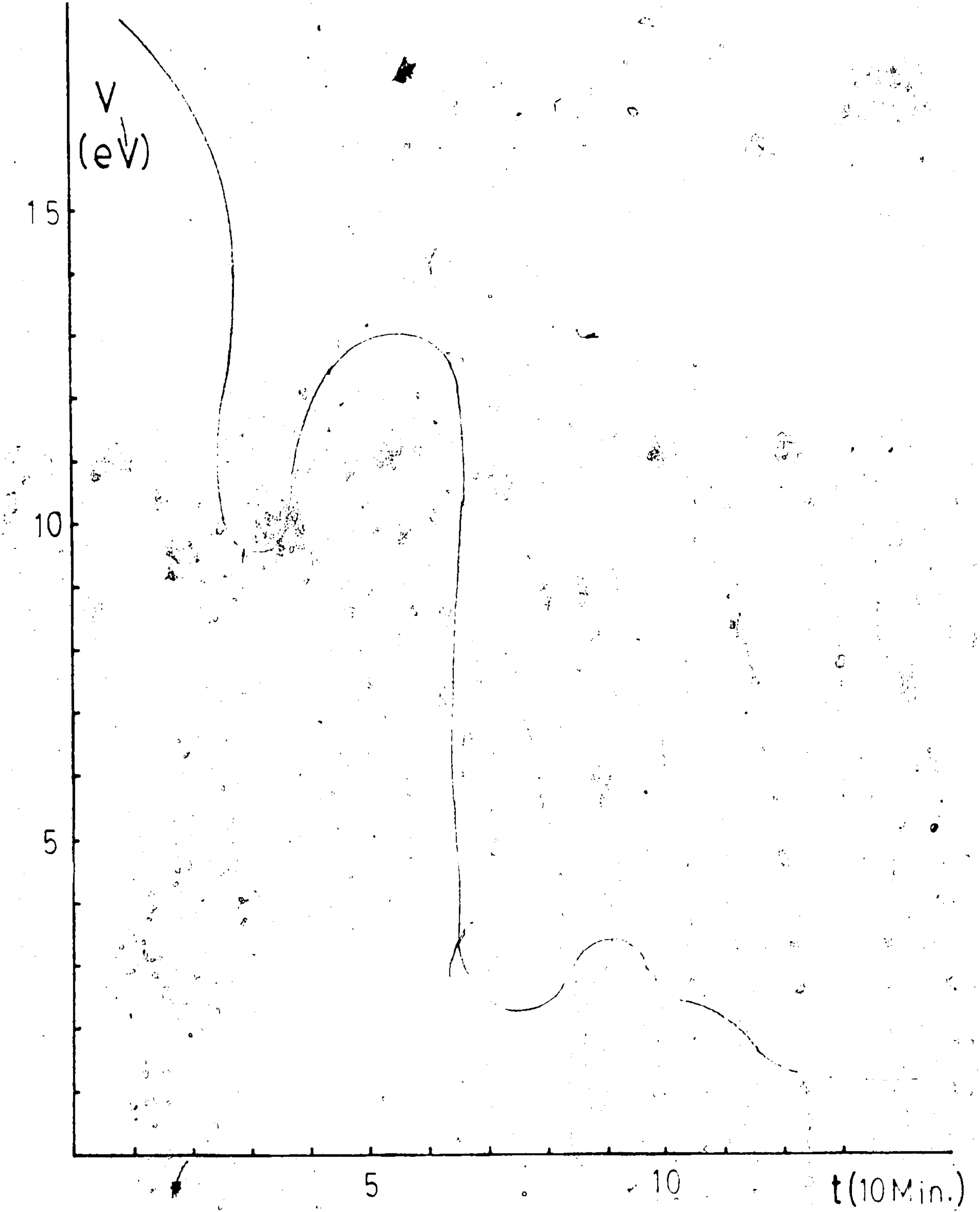

Fig. 2.8. The drift of the zero-loss peak as a function of the warming up time of the spectrometer. The zero-loss peaks were measured from the screen of the spectrum monitor.

mains-frequency fields and their effect can be compensated by using a simple circuit (Egerton 1986). Figure 2.9 shows the effect of AC compensation against stray AC fields of the main frequency.

2.3 THE SYSTEM FOR RECORDING AND ANALYZING DATA

The distribution of electron intensity at the dispersion plane produced by the spectrometer must be converted into a form suitable for a multichannel analyser (MCA). There are two possible ways to record the EEL spectrum. One is the parallel readout which has the advantage of high collection efficiency and has gained considerable interest over the past years (Shuman 1981, Egerton 1982, Cheng 1983, Ahn and Krivanek 1986, Egerton and Crozier 1987). The other is the serial readout which is more popular at the present time and was used in all the experiments described in this thesis.

The serial detector system in the Gatan Electron spectrometer, Model 607, consists of a photomultiplier tube (PMT) and a PMT signal-processing module (Fig. 2.10). The anode of the photomultiplier tube (PMT) is held close to the ground potential so that both the PMT current and pulses due to signal electrons are a valid measure of the signal strength. A simple R-C network at the input end of the

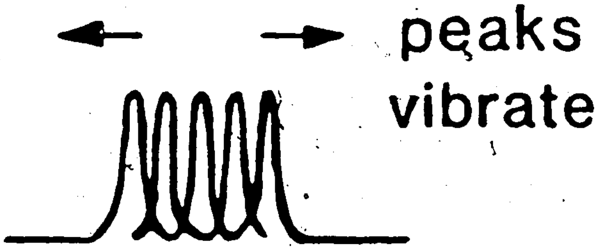

uncompensated

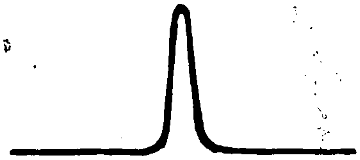

compensated

Fig. 2.9. Effect of AC compensation against stray AC field.

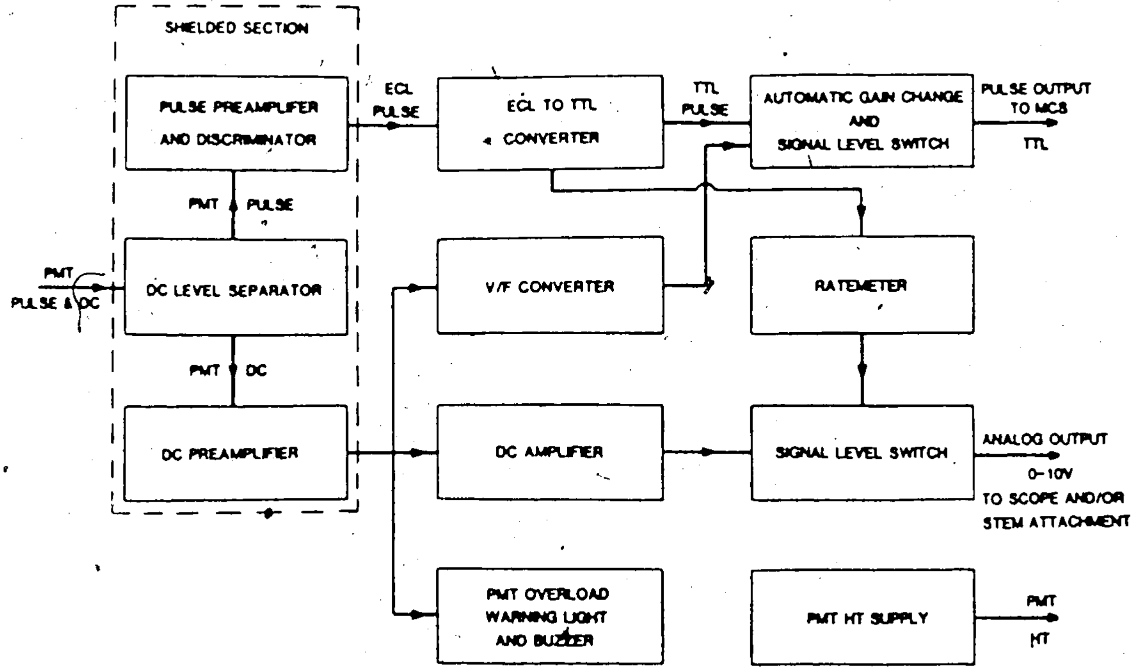

Fig. 2.10. Schematic of PMT signal-processing module.

module separates the pulses from the DC level. The two signals are then processed in parallel. One is processed by pulse-counting electronics consisting of a preamplifier, a discriminator, an emitter-coupled logic (ECL) to transistor-transistor logic (TTL) converter and a ratemeter; this is called the pulse-counting mode. The other signal is processed by current-measuring electronics consisting of a preamplifier, an amplifier and a voltage to frequency (V-F) converter, and is called the current-measuring mode. Each mode produces a train of TTL pulses to be used by the multichannel analyser (MCA) and a 0-10 V analog signal to be used by the videoscope. One or the other mode is selected as the output source by a 'signal level' switch.

In all the experiments reported in this thesis, signals obtained from the selected output source of the detector system are transferred to a TN-1710 Multichannel Analyzer (MCA), using a selected dwell time (the time for which the data is stored in each channel). After acquisition the data are processed with the help of a TN-1117 floppy disk memory system (used for recording spectra and loading the system operating program), and a Texas Instruments Silent 700 data terminal.

As in any field of spectrometry, the detection system for EELS plays an important role in determining the performance of the technique. An artifact of the detection system may appear as a systematic error in the final data unless suitable precautions or corrections are made. Because of the large range of signal intensities in EELS, both signal-processing modes mentioned above are required for recording the signal. At low-to-medium electron intensities the pulse-counting mode is preferable since it discriminates against the weak noise pulses that make up the PMT dark current. At high electron intensities the problem of the pulse overlap becomes significant in the pulse-counting mode; the current-measuring mode is therefore preferable since the PMT dark current becomes a small fraction of the total PMT current. Recently, Discko (1986) reported that for count rates below 1 MHz, the signals obtained by the pulse-counting mode and by the current-measuring mode were identical; but at higher count rates the pulse-counting signal was lower than the scaled current-measuring (V-F) signal, indicating the distortions of the pulse-counting signal. Craven and Buggy (1984) also reported that the ratio of the pulse-counting signal to the corrected V-F (analogue) signal is constant only over a limited range of signal levels. To avoid artifacts of the detection system, the linear ranges of the pulse-counting system and of the current-measuring system in the Gatan spectrometer (connected to the Tracor 1710 Multichannel Analyser) were tested.

The linear range of the pulse-counting system was determined by changing the incident beam current and observing the value of $\log_e(I_t/I_o)$ from a given specimen as a function of the counting frequency; here I_t and I_o are the integrated intensities under the whole and the zero-oss spectrum respectively. For non-distorted pulse counting, the observed $\log_e(I_t/I_o)$ values are expected to be independent of the counting frequency, since the former is related only to the specimen thickness and the mean free path which are constants for a given specimen (Chapter 4). Figure 2.11 shows that for the detection system under investigation, the $\log_e(I_t/I_o)$ values are independent of the counting frequency at counting frequencies lower than 1 MHz. This is consistent with the result reported by Disko (Disko 1986).

To understand the behavior of the cou[illegible]em, further investigation on the relationship between the expected 'true' frequency f_t and the observed frequency f_{ob} recorded by the counting system was carried out in the same EELS system mentioned above but without a specimen. Various frequencies were obtained by changing intensities of the electron beam entering the spectrometer by means of a change in the diameter of the illumination on the screen of the microscope. The electron beam currents were measured with a Faraday cup and converted into equivalent numbers of 'true' input pulses. The calibrations of the beam currents and the true frequencies were made in the linear range of the pulse-counting system (f_{ob}<1 MHz). The results are plotted

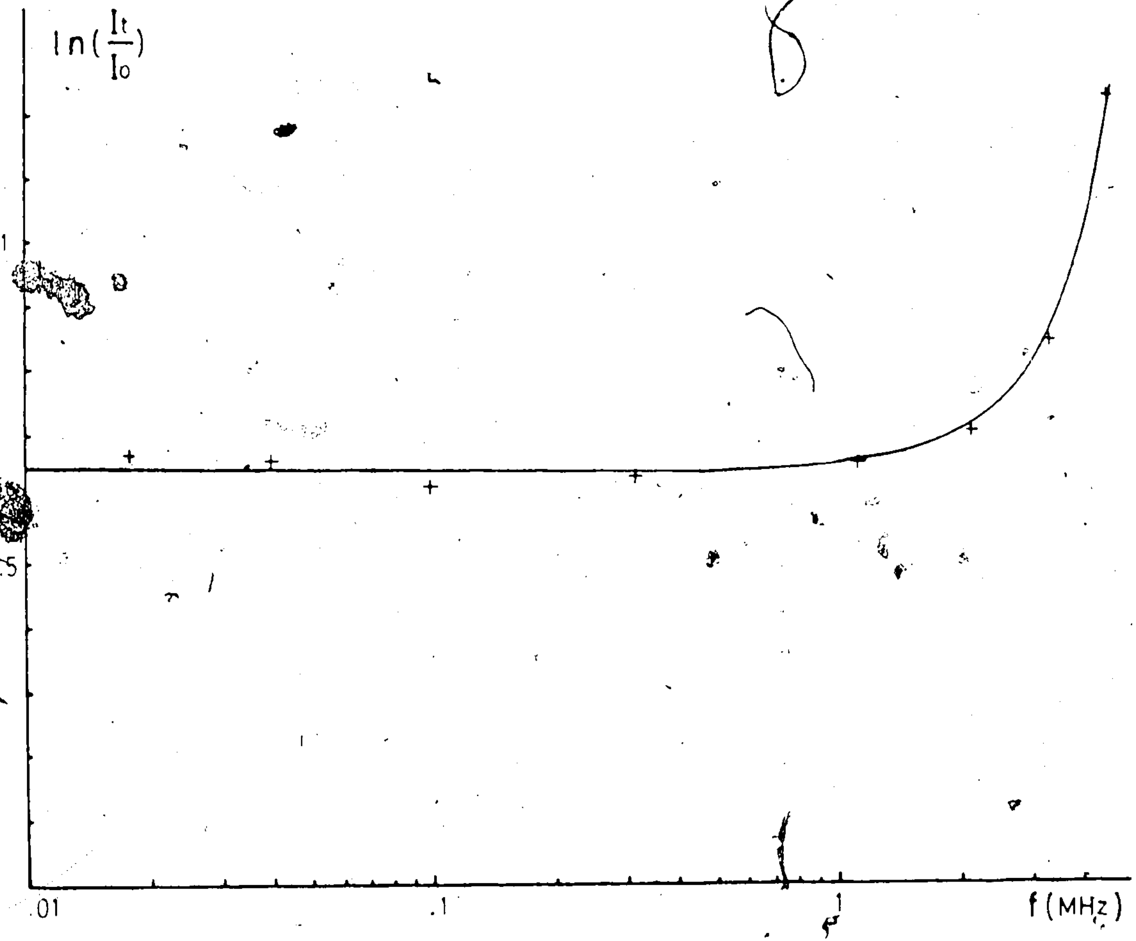

Fig. 2.11. $\log_e(I_t/I_o)$ as a function of the counting frequency.

in Fig. 2.12 (symbols). The experimental results show that f_t initially increases linearly with increasing f_{ob} at frequencies less than 1.5 MHz, then increases at a lower rate and finally becomes saturated at very high frequencies (above 20 MHz).

Some workers (Reed 1972, Craven and Buggy 1984) suggested use of the following formula to describe the behavior of the counting system:

$$f_{ob} = f_t \exp(-f_t \tau) \qquad (2.4)$$

where τ is the deadtime which is defined as the period when pulses are actually being processed. The relationship between f_{ob} and f_t according to Eq. (2.4) is also plotted in Fig. 2.12 as the dotted curve. Figure 2.12 shows that for the system under investigation, predictions of Eq. (2.4) agree well with the experimental datum only at $f_{ob}<1.5$ MHz; it fails at higher frequencies.

The following formula has also been suggested to describe the relationship between f_t and f_{ob} for a pulse-counting system (Ruark and Brammer 1937, Cheng et al. 1987):

$$f_{ob} = \frac{f_t}{1+f_t\tau} \qquad (2.5)$$

The relationship between f_{ob} and f_t according to Eq. (2.5) is plotted as the solid curve in Fig. 2.12. The reasonable

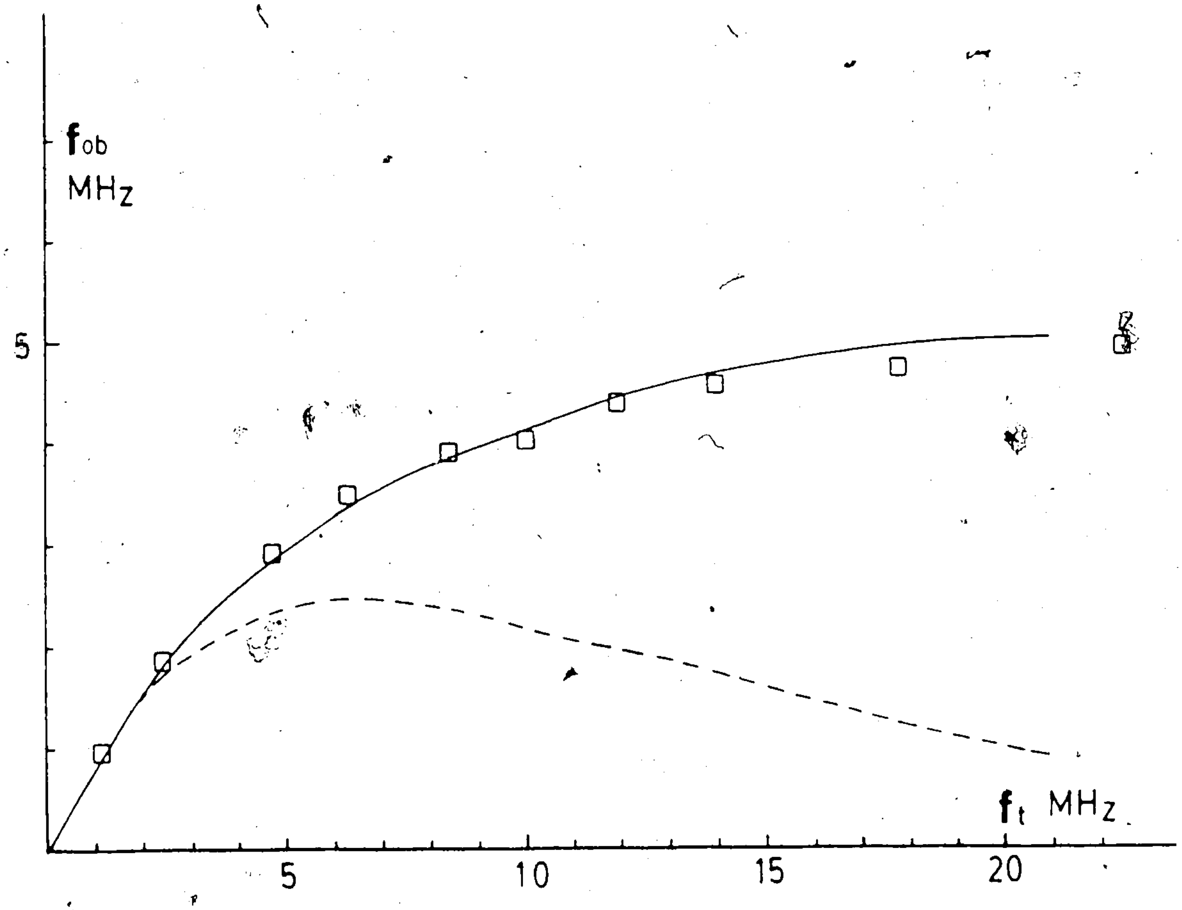

Fig. 2.12. Plot of the true frequency vs. the observed frequency of the pulse-counting system. The symbols represent the experimental results. The magnification indicated on the 'level' switch of the microscope screen was 5000. The slit of the spectrometer was widely opened. The dwell time of the Tractor 1710 Multichannel Analyser (MCA) was 10 ms. The dotted and solid curves represent the relationship according to Eqs. (2.4) and (2.5), respectively.

agreement between the experimental results and the curve predicted from Eq. (2.5) suggests that Eq. (2.5) can be used to correct the observed frequency at frequencies higher than 1.5 MHz, thereby extending the range of electron intensities which can be recorded in the pulse-counting mode.

The linear range of the current-measuring mode was obtained by plotting the curve of the incident electron beam current (measured by the Faraday cup) versus the output frequency from the V-F convertor (VFC), read out from the MCA. Figure 2.13 shows that the highest frequency in the linear range of the VFC is about 1.2 MHz.

When the current-measuring mode is used together with the low-to-high energy loss scan for recording a spectrum in the low-loss region, the intense zero-loss beam has a relatively prolonged effect on the detection system (Joy and Maher 1980). Disko (1986) has described the use of a high-to-low energy loss scan to avoid the above problem. Disko's suggestion was studied for a 35 nm thickness Ni film. In this experiment, the intensity of the incident beam, the entrance-aperture diameter and the exit slit of spectrometer were adjusted to ensure that the V-F converter was working in the linear range. Figure 2.14 shows a comparison of the spectra obtained when scanning away from the zero loss towards the higher energy losses (spectrum A) and in the reverse direction (spectrum B). In the region following the zero loss peak, the intensity of spectrum A is

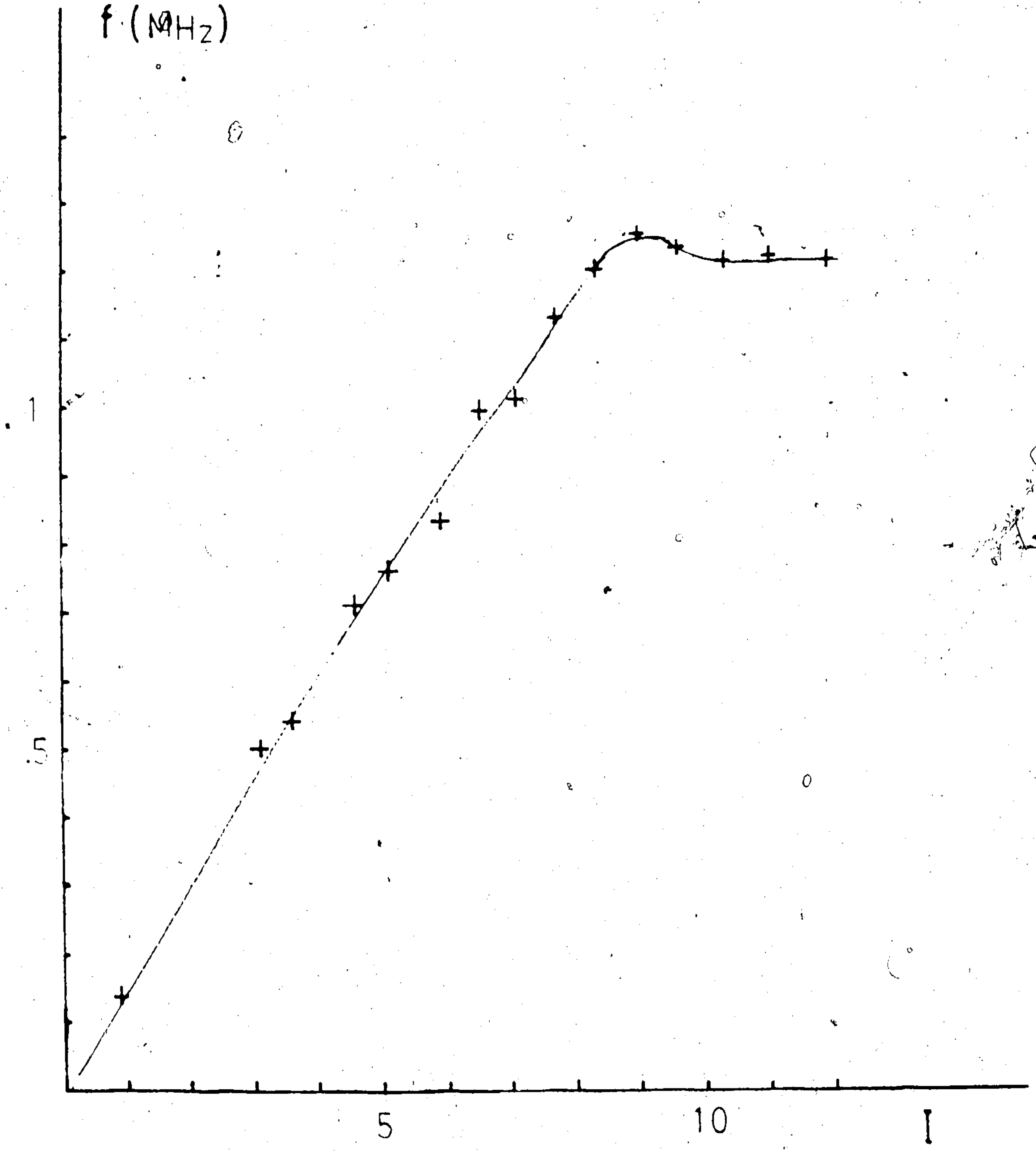

Fig. 2.13. Plot of the observed frequency of VFC vs. the incident electron-beam current. The current I is in arbitrary unit.

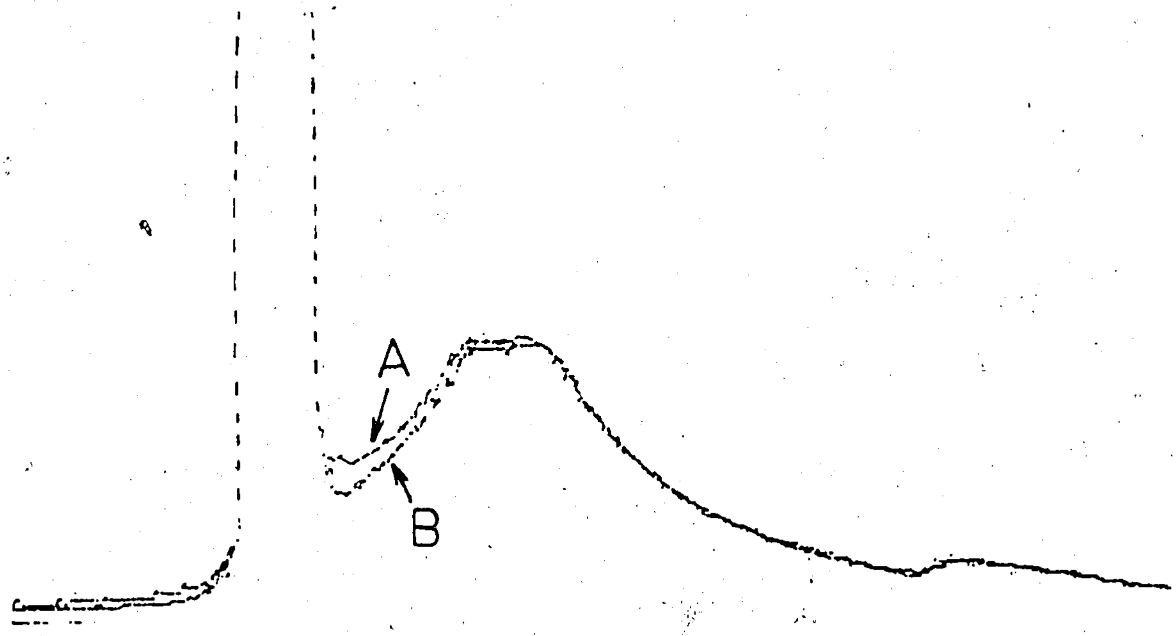

Fig. 2.14. Comparison of the Ni spectra obtained when scanning away from the zero loss to higher energy losses (spectrum A) and in the reverse direction (spectrum B).

higher than that of spectrum B. This extra intensity may cause the results of thickness measurement by the Kramers-Kronig sum rule to be 10% higher than the true value (Chapter 5). However, it may increase the measured mean free path by only 3% (Chapter 4).

In all the experiments reported in this thesis, the counting frequency was under 1 MHz when the spectrum was recorded in the pulse-counting mode; and the counting frequency was under 1.2 MHz when the spectrum was recorded in the current-measuring mode to avoid artifacts of the detection system. Also, whenever necessary, the scan in the current-measuring mode was in the reverse direction (high-to-low energy loss scan) to avoid the prolonged effects of the intense zero-loss beam.

2.4 THE VACUUM SYSTEM FOR FILM PREPARATION

The vacuum system used for film preparation is a typical oil-diffusion pump evaporation system (Fig. 2.15) A liquid nitrogen cold trap, mounted between the high vacuum valve and basesplate, was used to prevent backstreaming of oil vapour and to reduce the partial pressure of condensable gases. An ionization guage was used to measure the pressure in the evaporation bell jar. The working pressure was below $5x10^{-6}$ torr. The distance between the substrate and the the

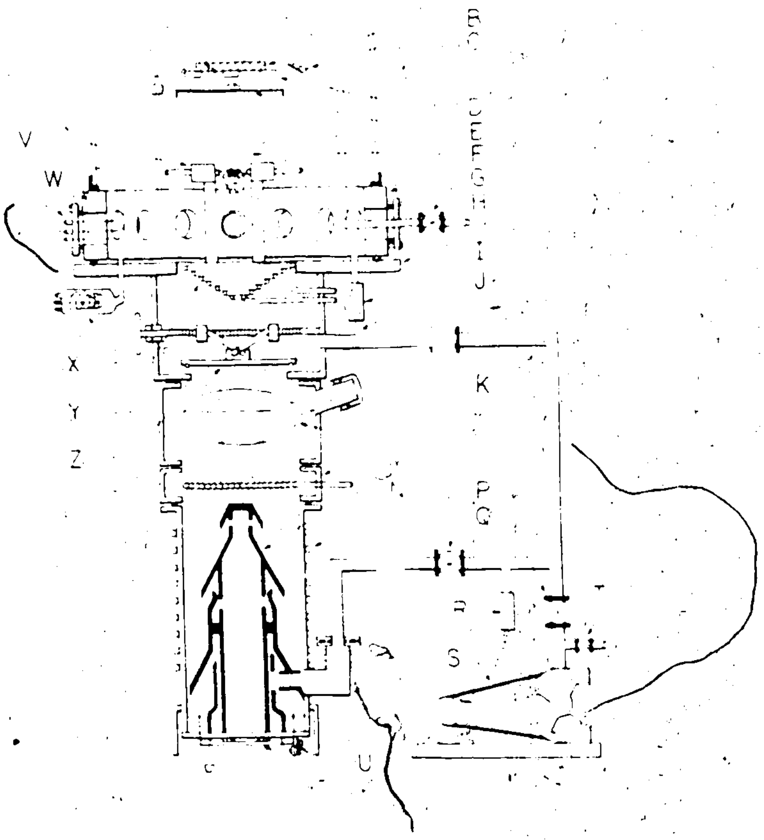

Fig. 2.15. A typical vacuum system. The notation stand for B, substrate; C, quartzcrystal rate controller and deposition monitor; D, substrate mask; E, shutter; F, vapors from evaporation source; G, adapter collar between the bell jar and the pump baseplate flange; H, air-inlet valve; I, baseplate flange; J, Pirani or thermocouple gauge; K, roughing valve; L, liquid air trap; M, cooled chevron baffles; N, diffusion pump; O, cooling coils; P and Q, backing valves; R, Pirani gauge; S, forepump with air-iinlet valve T; U, diffusion pump heater; V, filament holders; W, multiple feedthrough; X, ionization gauge; Y, Meissner trap; Z, baffle valve.

evaporation source is longer than 15 cm in order to obtain a uniform deposition. A simple calculation shows that the non-uniformity of the film (on a substrate which is 22x22 mm^2) is less than 2% under these conditions.

There is a removable shutter between the substrate and the evaporation source. The shutter was used to mask the substrate when the source was warming up. After removing the shutter, the evaporation rate could be kept constant by adjusting the heater current slightly; this was done manually.

A quartz crystal was used to monitor the thickness of the evaporated film, and was hence an important part of the system. The crystal was gold-coated and was placed above the sources at the same distance as the substrate. The quartz-oscillator calibration curve was predetermined by interferometry as follows (Munoz 1983):

$$t = 1.67 \frac{\Delta f}{\rho} \qquad (2.6)$$

where t is the thickness of the evaporated film; Δf is the change of frequency of the quartz-crystal oscillator; ρ is the density of the evaporated material. The calibration of the quartz-oscillator was made on a copper film; for other material the calibration may be slightly different because of the different sticking efficiencies. Eq. (2.6) was used only to estimate the thickness of the evaporating film and so to control the evaporation process. The actual thickness of an evaporated film relied on the method of weighing.

CHAPTER 3

THE SIGNAL/BACKGROUND RATIO OF INNER-SHELL IONIZATION EDGES IN EELS

3.1 INTRODUCTION

As mentioned in Chapter 1 the inner-shell ionization edges in EELS are normally used to identify the presence of a given element within the area of specimen defined by the incident beam of electrons. A quantitative estimation, giving the number of atoms of the element per unit area of specimen, N, is obtained from the following formula (Egerton 1978a):

$$N = \frac{1}{G} \frac{I_k(\Delta,\beta)}{I_l(\Delta,\beta)} \frac{1}{\sigma_k(\Delta,\beta)} \qquad (3.1)$$

where β is the maximum electron scattering angle, which is limited by the objective aperture; Δ is the energy window; $\sigma_k(\Delta,\beta)$ is the partial cross-section of the element, corresponding to K-shell losses between the threshold energy E_k and $E_k+\Delta$, with a scattering angle θ less than β; $I_l(\Delta,\beta)$ is the intensity in the low-loss region of the spectrum integrated up to an energy loss $E = \Delta$; $I_k(\Delta,\beta)$ is the intensity in the high-loss region of the spectrum integrated from E_k to $E_k+\Delta$; and G is a factor which allows for any difference in the detector gain between the low- and the high-energy region of the spectrum.

The intensity integral under the low-loss energy region of the spectrum, $I_\ell(\Delta,\beta)$, is obtained by straightforward summation of the channel counts. The intensity integral under the high-loss energy region of the spectrum, $I_k(\Delta,\beta)$, sits, however, on a high background which is caused by other loss processes and contains no special information. Therefore, for measurements of $I_k(\Delta,\beta)$, the background has to be stripped. The general method for background stripping and for measurement of $I_k(\Delta,\beta)$ is given below and is illustrated in Fig. 3.1.

A fitting energy window (E_1, E_2) located before the threshold energy E_k is first selected, and is typically 50 to 200 eV wide. A power law $AE^{-\gamma}$ is then adjusted to fit the data within the fitting energy window. The constants A and γ in the power law can be estimated from the following formulas (Egerton 1980):

$$\gamma = \frac{2\log(I_1/I_2)}{\log(E_2/E_1)} \tag{3.2}$$

$$A = \frac{(I_1+I_2)(1-\gamma)}{E_2^{1-\gamma} - E_1^{1-\gamma}} \tag{3.3}$$

where the fitting window (E_1, E_2) is divided in two halves of respective integrals I_1 and I_2. Once the fit is made, the

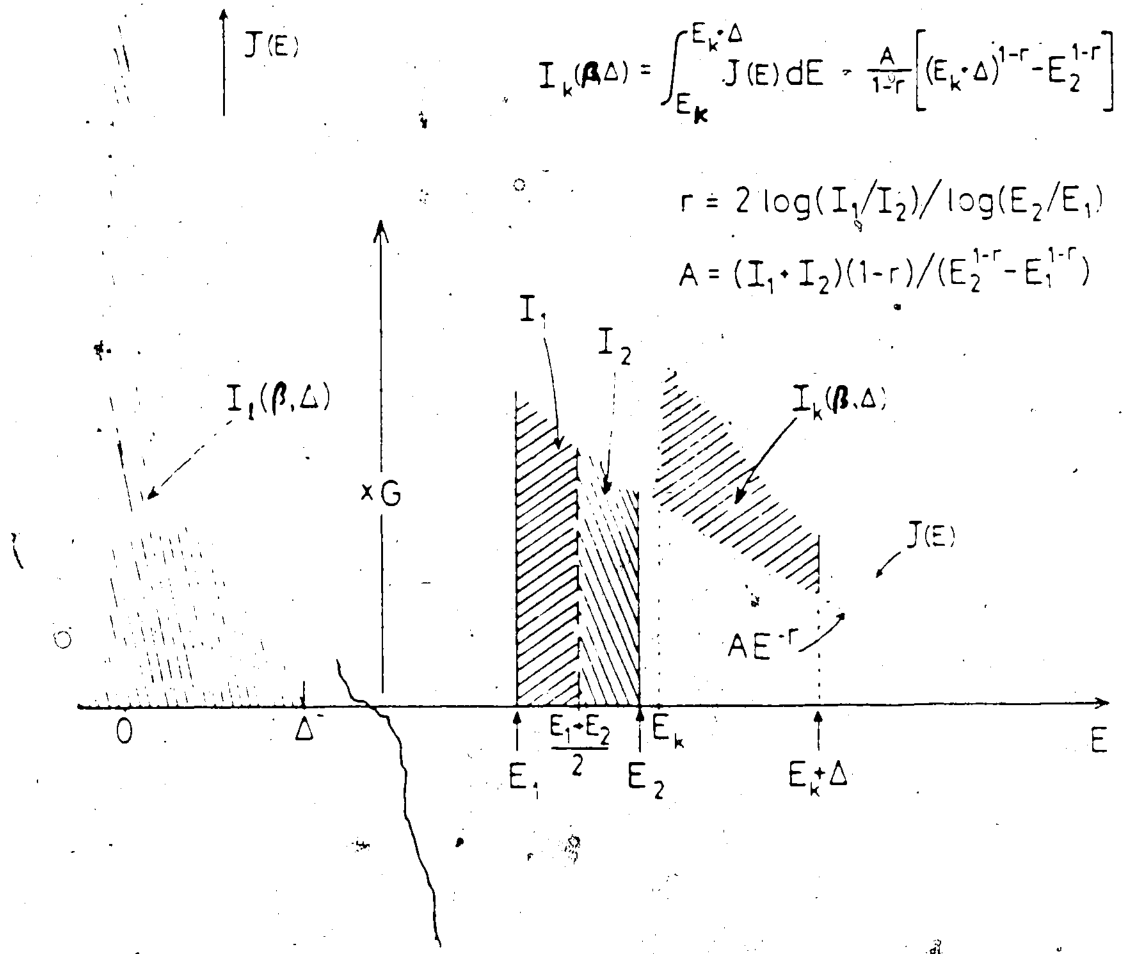

Fig. 3.1. Schematic EELS, illustrating measurement of $I_k(\Delta,\beta)$ and the method of background fitting.

power law $AE^{-\gamma}$ is extrapolated under the characteristic edge up to a few hundreds of eV. The intensity integral $I_k(\Delta,\beta)$ is then evaluated using the following relation:

$$I_k(\Delta,\beta) = \int_{E_2}^{E_k+\Delta} J(E)\, dE - \frac{A}{1-\gamma}\left[(E_k+\Delta)^{1-\gamma} - E_2^{1-\gamma}\right] \qquad (3.4)$$

where J(E) is the total intensity including both the background and the signal.

Equations (3.1)-(3.4) show that the improvement of the signal/background ratio is important for EELS as a practical technique for quantitative analysis since the signal/background ratio for inner-shell excitation edges is low.

Presented in this Chapter are the effect on the signal/background ratio of the collection aperture and the thickness of the specimen. The earlier reports that the signal/background ratio of the aluminum K-edge was sometimes improved by an off-axis collection aperture and thicker specimen (Oikawa et al. 1984, Hosoi et al. 1984) have been confirmed experimentally but interpreted as an artifact arising from the presence of a high instrumental background. Some essential requirements regarding the electron-detection system to improve the signal/background ratio are discussed.

3.2 USING A CENTRAL COLLECTION APERTURE (BRIGHT-FIELD CONDITIONS) AND THIN SPECIMEN

In transmission electron energy-loss spectroscopy, inner-shell ionization edges are usually recorded using a central collection aperture (as in bright-field imaging) and a very thin specimen.

The reason for using the bright-field condition can be understood from the Bethe theory and the Bethe surface (Bethe 1930, Inokuti 1971). The Bethe theory provides a general framework for discussing the inelastic scattering of fast electrons and leads to powerful criteria for judging the reliability of cross-section data. The central notion of the theory is the generalized oscillator strength (GOS) as a function of both the energy transfer and the momentum transfer. The Bethe surface is the generalized oscillator-strength (GOS) density df(K,E)/dE as a function of both E and K, where E is the transferred energy and $\hbar K$ is the transferred momentum from incident electrons ($\hbar = h/2\pi$ and h is the Planck's constant). As an example, the hydrogenic GOS for carbon K-shell excitation is shown as a function of E and $\ln(Ka_0)^2$ in Fig. 3.2, where a_0 is the Bohr radius (Egerton 1979). The main feature of the figure is that individual curves show qualitatively the angular dependence of K-shell scattering for different amounts of

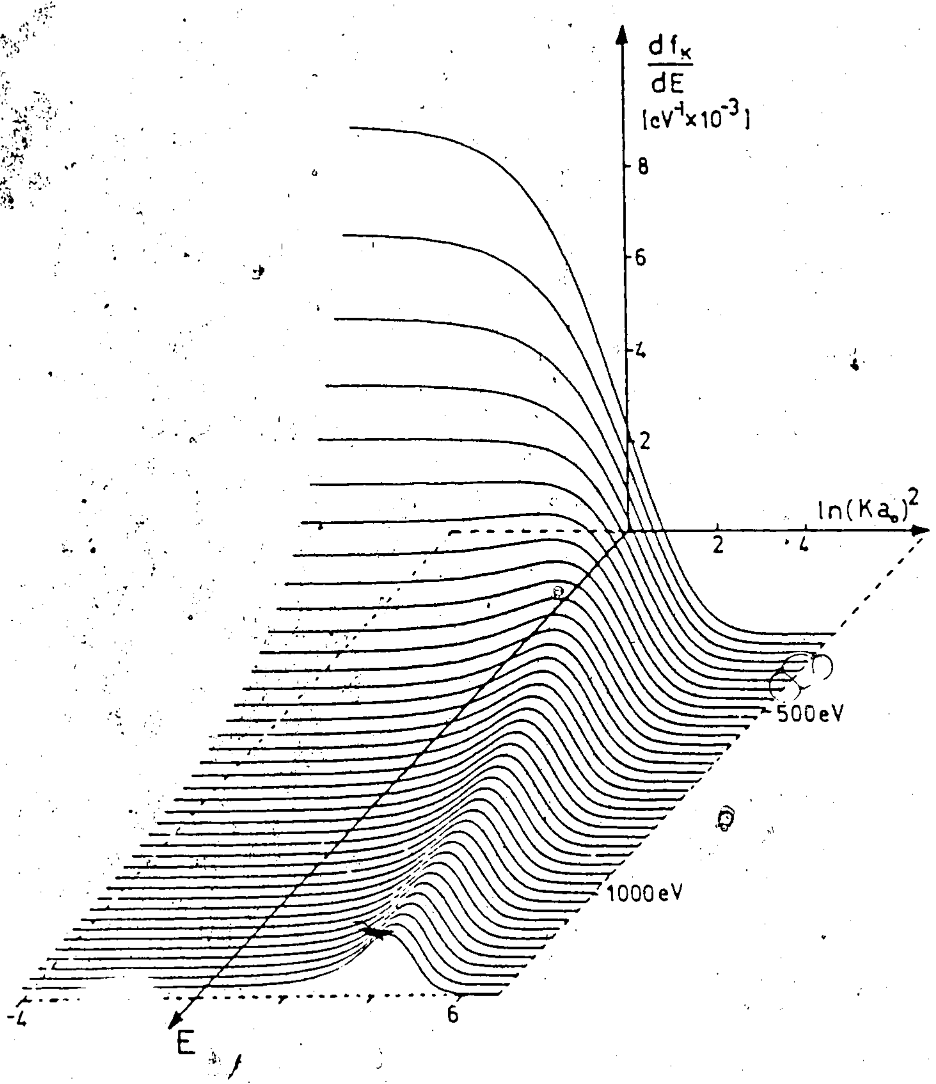

Fig. 3.2. The Be[illegible] surface for K-shell ionization in carbon calculated from [illegible] hydrogenic model.

energy loss. For an energy loss not much larger than the threshold value E_k, the scattering is forward-peaked (i.e., is of maximum intensity at scattering angle $\theta = 0$); whereas for large energy loss (several times E_k) the scattered electrons are concentrated around an angle given by $(Ka_o)^2 = E/R$ (where R = 13.6 eV is the Rydberg energy), forming a Bethe ridge which represents hard collisions, that is, those with small impact parameter. According to the properties of the Bethe surface, the signal/background is expected to fall if the collection aperture is sized or displaced from the optic axis. In other words, using the bright-field conditions the pre-edge background should have a broader angular distribution than that of the core-loss intensity, as a result of non-dipole contributions from the Bethe ridge.

The reason for preferring a thin specimen is that, whereas the initial increase of the intensity at the ionization edge arises from single scattering from inner shells, the pre-edge background (in thicker samples) contains an appreciable contribution from plural scattering, mainly one or more "plasmon" losses which precede or follow the core-loss event. Increasing the sample thickness should therefore result in a lower signal/background ratio (Egerton 1978a).

3.3 USING AN OFF-CENTER COLLECTION APERTURE (DARK-FIELD CONDITIONS) AND THICKER SAMPLES

Oikawa, Hosoi and co-workers (Oikawa et al. 1984) reported their experimental results for scattering angle dependence of the signal/background ratio of Si K-shell and Al K-shell electron excitation losses measured for single crystals and evaporated films. The scattering angle, θ, is limited by the position of the objective aperture. They found that the ratio of the signal integral for electrons collected at the scattering angle θ to that collected at zero scattering angle, $S(\theta)/S(0)$, changed periodically: the ratio of the background integral for electrons collected at the scattering angle θ to that collected at zero scattering angle, $B(\theta)/B(0)$, also changed periodically. However, the latter was in antiphase with the former. As a result, the signal/background ratio changed periodically with the scattering angle and had a maximum between Bragg reflections including the central beam. In addition, they found that the above observations were independent of the element (Si or Al), independent of the material structure (single crystal or evaporated film), and independent of the thickness of the specimen. Based on their experimental results, Oikawa et al. proposed to select the scattering angle between Bragg reflections or just outside the center beam, i.e., using an off-center collection aperture (dark-field conditions), to improve the signal/background ratio. They concluded that this is a practical operation technique for quantitative analysis of elements in the high-energy loss region; and hence, there is a need for knowing the "doubly partial cross-section".

Hosoi, Oikawa and co-workers (Hosoi et al. 1984) also reported the experimental results of the effect of the specimen thickness on the core-edge loss intensity using the relative specimen thickness, t_R, as the standard rule for the specimen thickness in EELS (Zaluzec 1980). They found that for aluminum single crystals, the core-edge loss intensity increased monotonically with increasing relative specimen thickness, t_R, for $t_R \leq 1$, but decreased monotonically with the increasing t_R for $t_R \geq 1$. The relative specimen thickness is defined as the ratio between the specimen thickness t and the total inelastic mean free path λ. At $t_R \approx 1$, the core-edge loss intensity had the maximum value. Therefore, Hosoi, Oikawa and co-workers suggested to use the relative thickness of $t_R = 1$ as the "optimum specimen thickness" to get the highest signal intensity of the core-edge loss and hence to improve the signal/background ratio.

3.4 EXPERIMENTAL

To understand the results of Oikawa's group (Oikawa et al. 1984, Hosoi et al. 1984), similar measurements on vacuum-evaporated polycrystalline aluminum were performed (Cheng and Egerton 1985). The method for preparing aluminum film is described in Chapter 4.

The thin film aluminum specimen was irradiated with 100 keV electrons in a JEM-100B conventional transmission microscope. A 20 μm diameter objective aperture (collection semi-angle $\simeq$ 5 mrad) was used to select the range of scattering angle contributing to the recorded spectrum; dark-field conditions were obtained by tilting the incident illumination rather than by shifting the aperture to avoid a large spherical aberration.

Energy-loss spectra were recorded in serial mode by scanning the magnetic field of the electron spectrometer. The electron detector consisted of a thin phosphor screen and a photomultiplier tube, whose output was digitized using a 5 MHz voltage-to-frequency converter and recorded using a Tracor Northern TN1710 multichannel analyser. The background preceding the aluminum K-ionization edge was fitted to a power-law energy dependence and the extrapolated background was integrated between energy losses of 1560 and 1620 eV to yield the background integral $B(\theta)$. The K-edge signal $S(\theta)$ was obtained by subtracting the background from the spectral data over this same energy region.

The specimen thickness t was measured in terms of the total inelastic mean free path, λ, (≃ 100 nm for 100 keV incident electrons) using the relation:

$$t/\lambda = \log_e(I_t/I_o)$$

where I_t and I_o are the integrals under the whole spectrum and under the zero-loss peak, respectively.

3.5 RESULTS

The initial results at two different values of t/λ are shown in Figs. 3.3 and 3.4. As expected from the theory, the K-loss signal and the pre-edge background both decrease with increasing scattering angle, the signal/background ratio eventually falling at higher angles. The signal/background ratio is not significantly higher in the dark-field conditions ($\theta > 0$) compared to that in the bright-field conditions ($\theta = 0$).

Since the difference between the experimental conditions performed and those of Oikawa et al. (200 keV operation, better angular resolution and larger integration window) were thought to be unimportant to the results, modifications in the detector-slit arrangement were made in

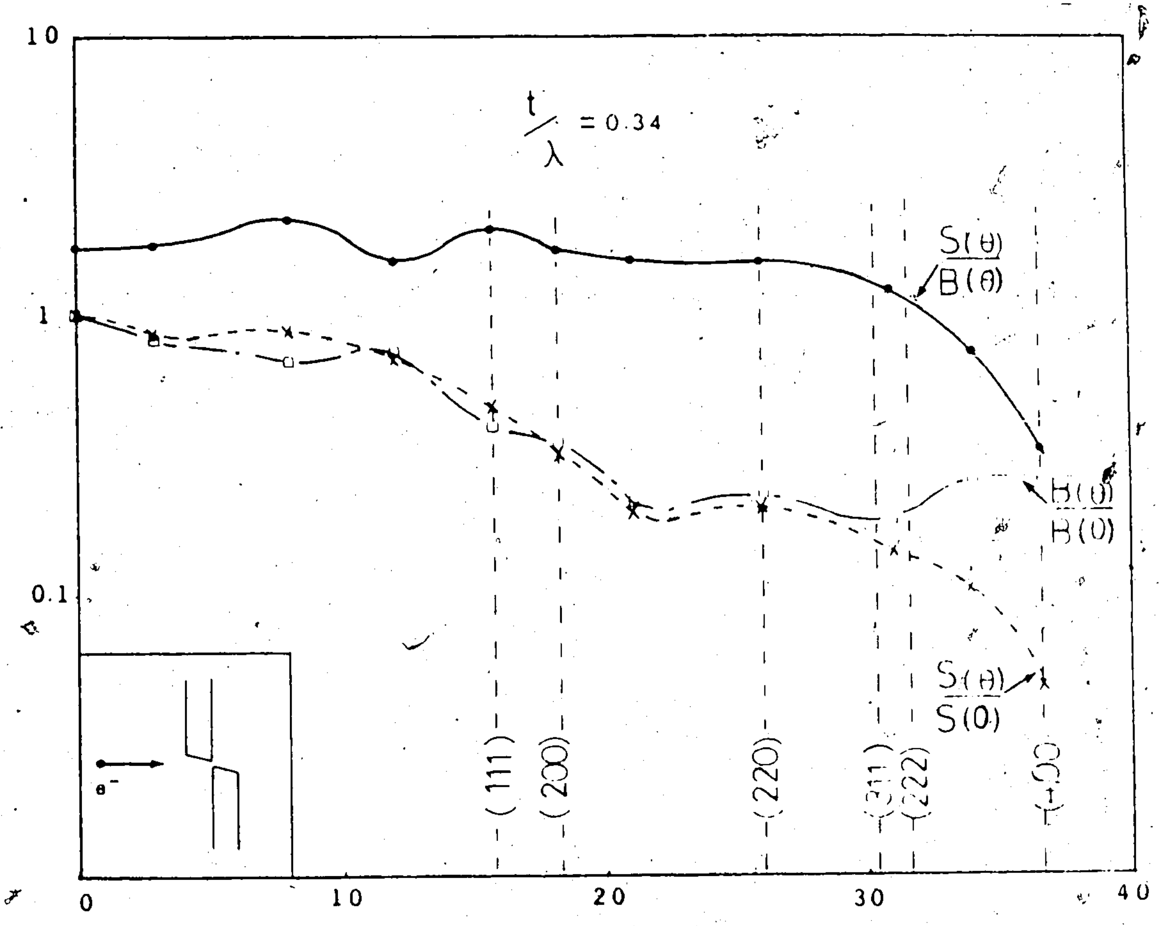

Fig. 3.3. K-loss signal S(θ), background B(θ) and signal/background ratio S(θ)/B(θ) measured as a function of scattering angle θ for polycrystalline film of aluminum with t/λ = 0.34, using the non-degraded detector-slit geometry shown in the inset. The scattering angles which correspond to rings in the diffraction pattern are also shown.

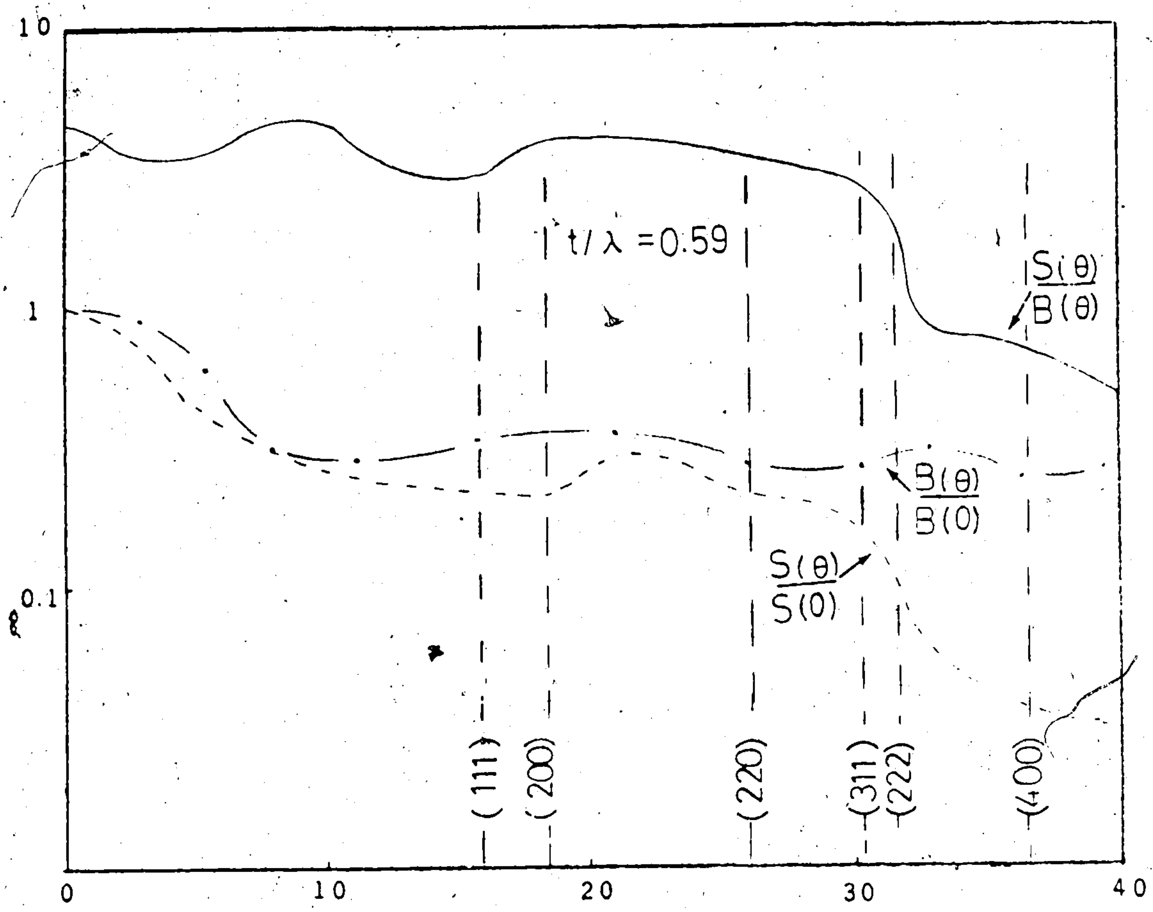

Fig. 3.4. The same as in Fig. 3.3 but using a thick polycrystalline film of aluminum with t/λ = 0.59.

an attempt to find the cause for the different experimental results reported here and reported by Oikawa et al. (Oikawa et al. 1984). The original 6 mm thick slit blades were replaced with 0.8 mm brass; and the length of the slit (in the non-dispersive direction) was increased from 1 to 10 mm (Fig. 3.5 inset). Figures 3.5 and 3.6 show that under the modified conditions, the signal/background ratio at $\theta = 0$ were about four times lower than that shown in Figs. 3.3 and 3.4. With increasing scattering angle θ, the K-loss signal and the pre-edge background both decreased; but the pre-edge background decreased faster than the signal. The signal/background ratio was higher in the dark-field conditions compared to the bright-field conditions.

Figures 3.7 and 3.8 show the results obtained by also offsetting the upper and lower detector slits by 6 mm in the exit-beam direction (Fig. 3.8 inset). These results closely resemble those reported by Oikawa, Hosoi and co-workers. The background under the bright-field illumination was one order of magnitude higher than before, resulting in a low signal/background ratio. Furthermore, comparing Fig. 3.7 with Fig. 3.8 it is seen that under the bright-field conditions, the signal/background ratio increased with increasing specimen thickness, which was the same as observed by the previous workers (Hosoi et al. 1984).

A further investigation showed that the instrumental background recorded for the modified (degraded)

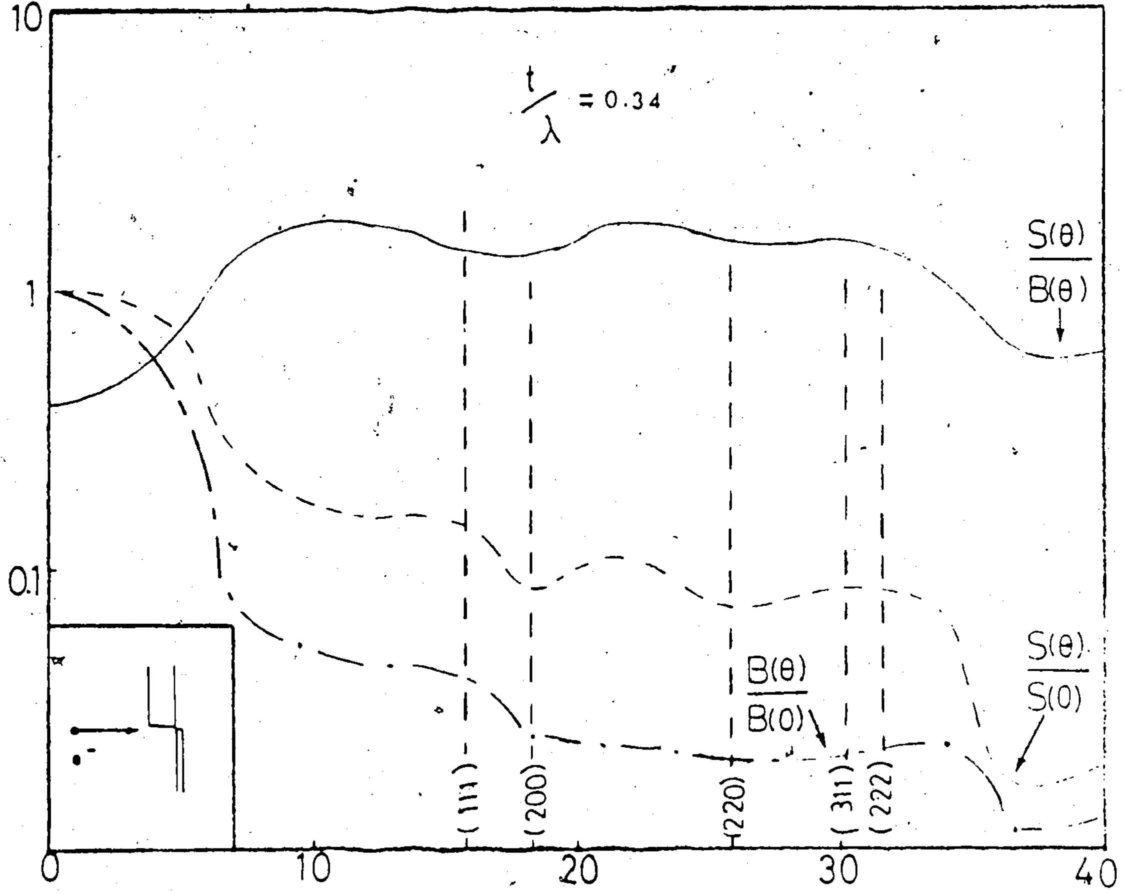

Fig. 3.5. The same as in Fig. 3.3 but using the degraded detector-slit arrangment shown in the inset.

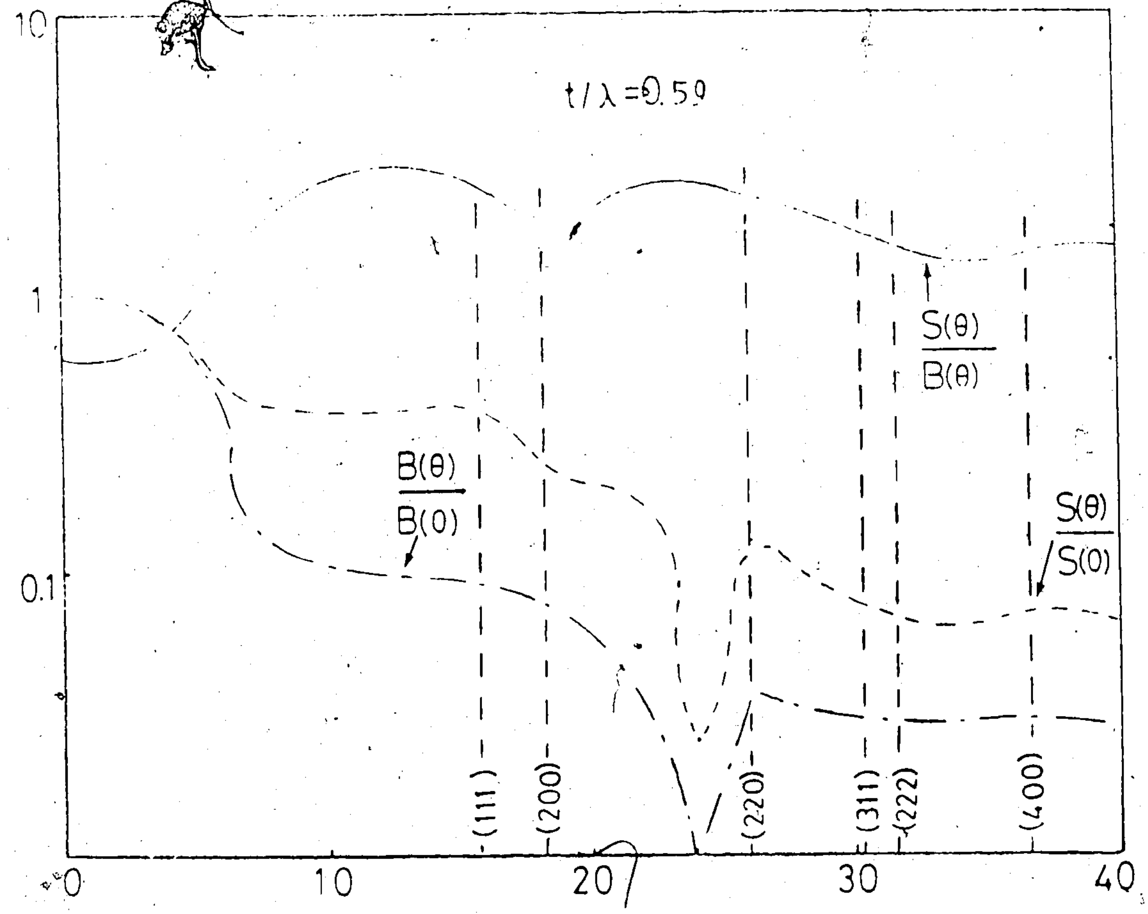

Fig. 3.6. The same as in Fig. 3.5 but using a thick polycrystalline film of aluminum with t/λ = 0.59.

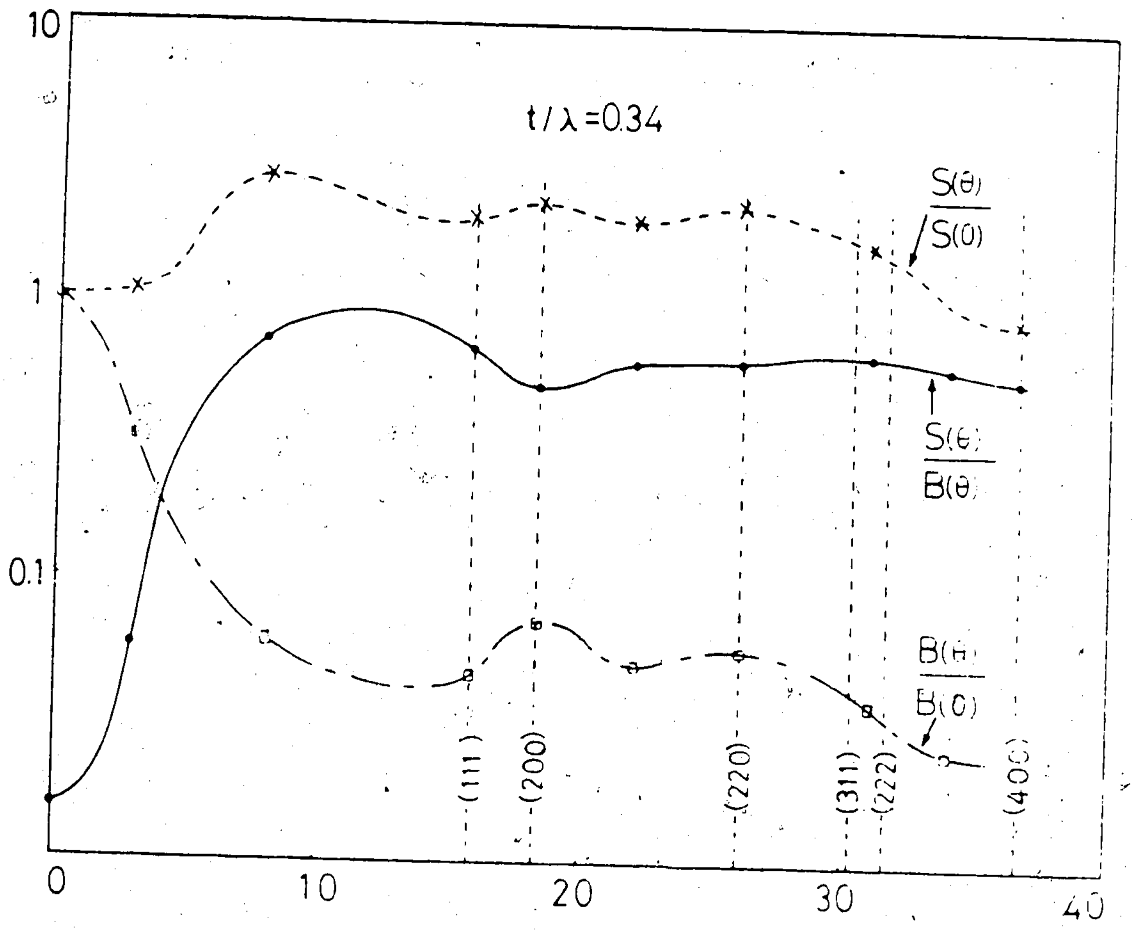

Fig. 3.7. The same as in Fig. 3.3 but using the more degraded detector-slit arrangement shown in the inset of Fig. 3.8.

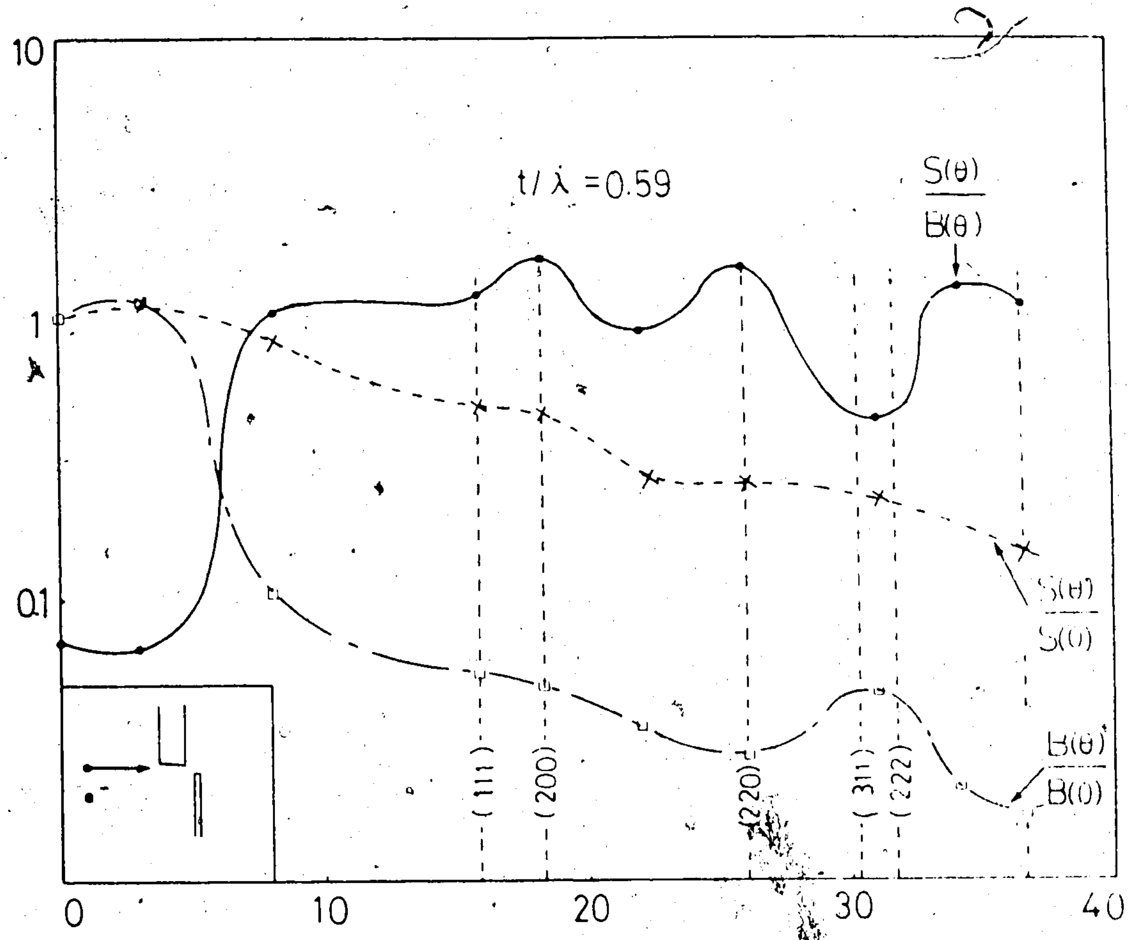

Fig. 3.8. The same as in Fig. 3.7 but using a thick polycrystalline film of aluminum with t/λ = 0.59.

detector-slit arrangement (corresponding to Figs. 3.5 and 3.6, and Figs. 3.7 and 3.8, respectively) was much higher than that recorded for the initial detector-slit arrangement (corresponding to Figs. 3.3 and 3.4), as illustrated in Figs. 3.9-3.11. In recording the instrumental background, the electron detector used was a phosphor-screen/photomultiplier whose output was converted into pulses, using a voltage-to-frequency (V-F) convertor, for counting in the multichannel analyzer. The energy range was about 2000 eV, a detector-gain change (x300) occured at 400 eV. The vertical axes in Figs. 3.9-3.11 show the number of V-F counts per channel, on a logarithmic scale.

3.6 DISCUSSION

The data shown in Figs. 3.5-3.8 can be interpreted in terms of the generation of an instrumental background to the energy loss spectrum by the intense zero-loss component of the undiffracted beam.

Under bright-field conditions, this component generates hard X-rays at the lower blade of the energy-selecting slit while higher energy losses are being recorded. If the slit material is sufficiently thin, some of these X-rays may penetrate through to the electron detector and give rise to a spurious background signal (Kihn et al. 1980). In

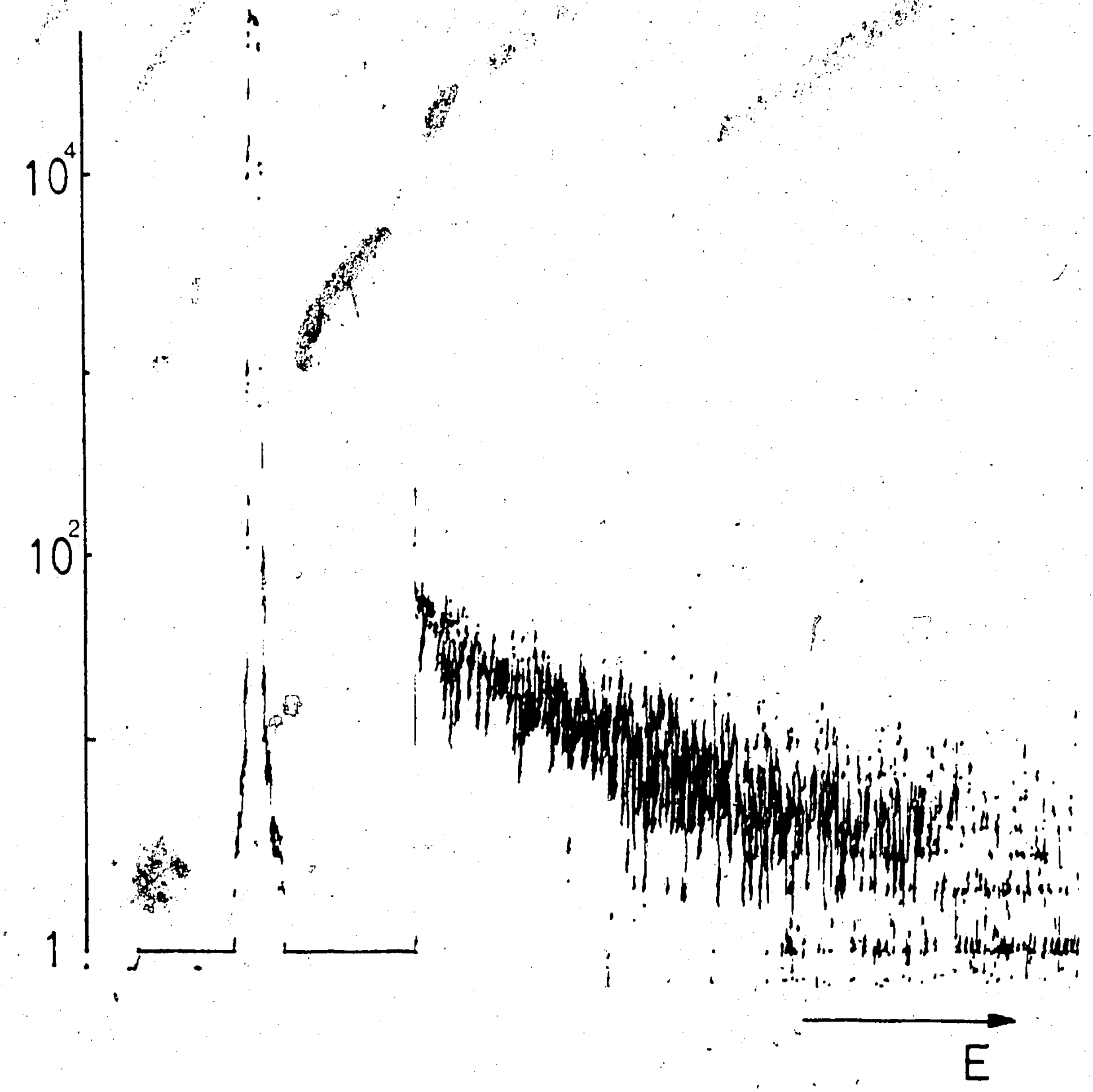

Fig. 3.9. The instrumental background recorded for the non-degraded detector-slit arrangement (obtained using the experimental conditions shown in Figs. 3.3 and 3.4).

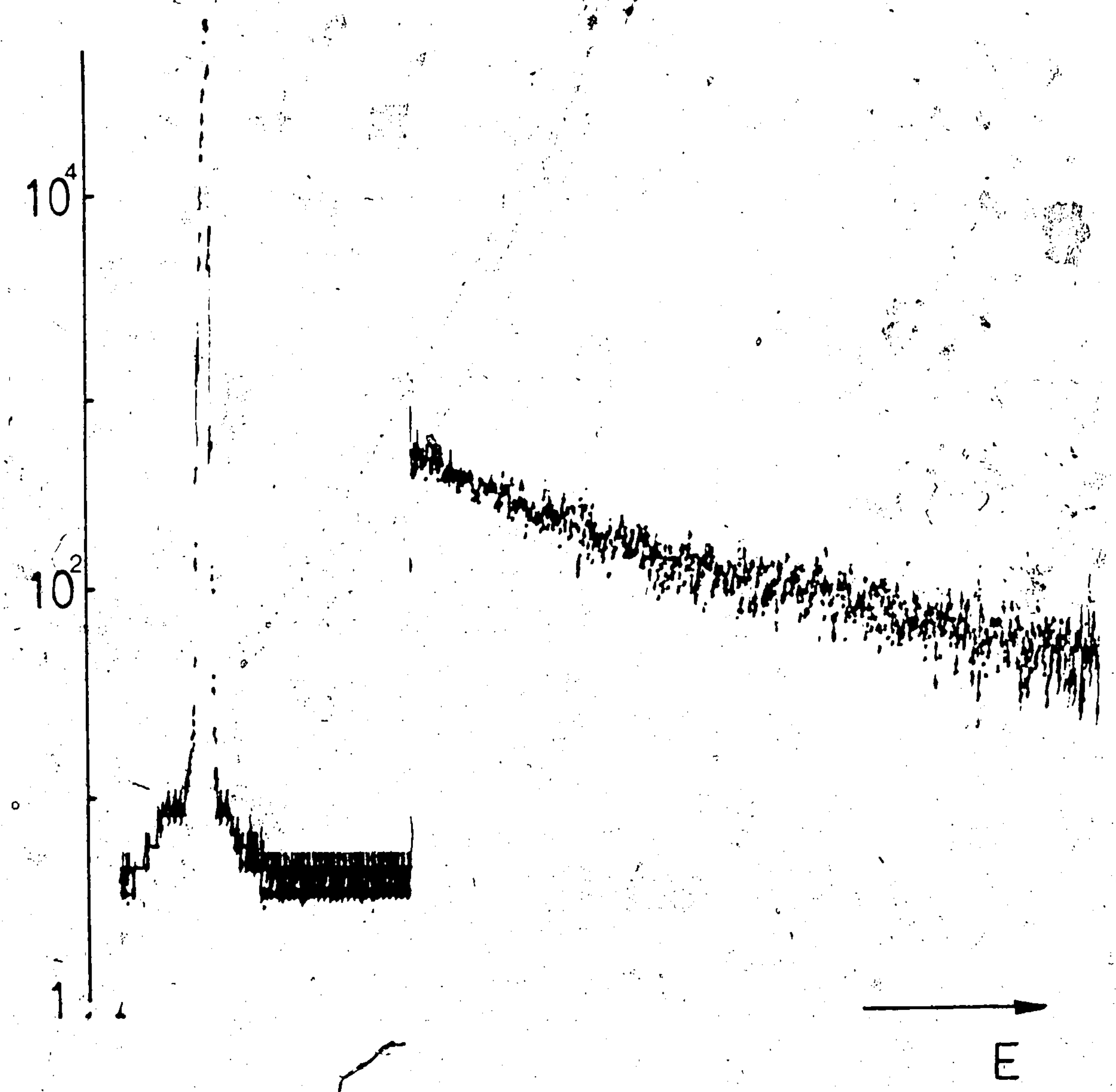

Fig. 3.10. The instrumental background recorded for the degraded detector-slit arrangement (obtained using the experimental conditions shown in Figs. 3.5 and 3.6).

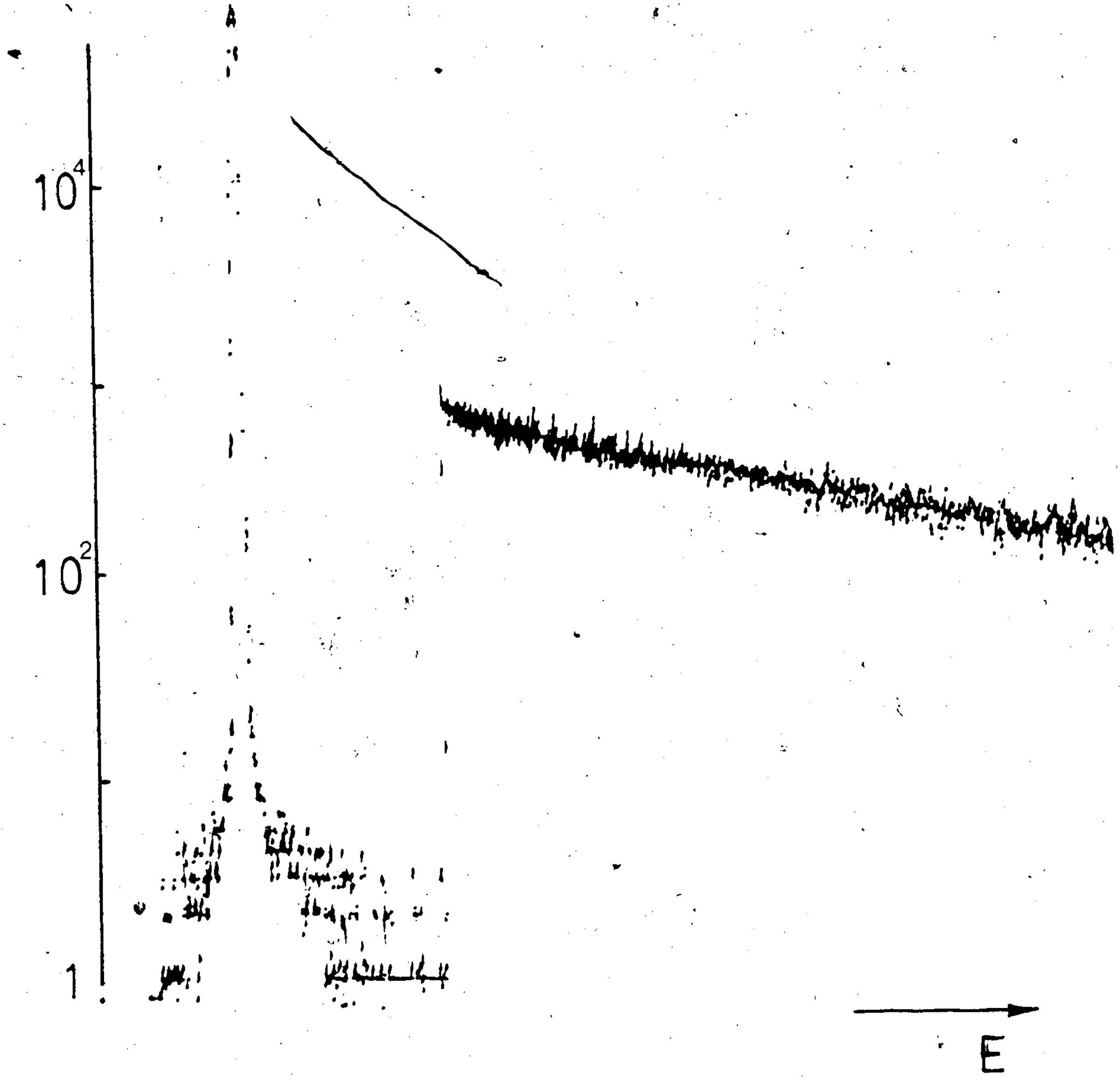

Fig. 3.11. The instrumental background recorded for the more degraded detector-slit arrangement (obtained using the experimental conditions shown in Figs. 3.7 and 3.8).

addition, backscattered electrons and X-rays generated at the slit blade can be reflected back through the slit opening towards the detector (Egerton 1978b, Craven and Buggy 1984). The resulting background is increased by lengthening the slit and by offsetting the two edges so that the effective slit width is large for electrons travelling at an appreciable angle relative to the optic axis.

Under bright-field conditions the instrumental background is also approximately independent of specimen thickness. The core-loss signal is, however, proportional to the specimen thickness. Consequently, at a high instrumental background the signal/background ratio is higher for a thicker specimen than for a thin specimen. This explains the results reported by Hosoi et al.

Under dark-field conditions, the intense undiffracted beam is intercepted by the objective aperture; scattered electrons and X-rays generated there have a much smaller probability of reaching the detector. Therefore, the instrumental background is lower and the signal/background ratio is higher than in the bright-field condition.

Although the zero-order undiffracted beam is usually the most intense and therefore acts as the main source of stray electrons and X-rays, prominent Bragg beams may make a significant contribution in thicker samples, which could explain some of the variation in background level in Figs. 3.3-3.8 and in the data of Oikawa et al.. The apparent decrease in signal in bright field [Figs. 3.5-3.8; also observed in (Oikawa et al. 1984)] is probably an artifact reflecting the difficulty of performing accurate background fitting and subtraction in the case of a weak ionization edge superimposed on a high background. However, some of the angular dependence of S(θ) and B(θ) in Figs. 3.3 and 3.4 could result from real diffraction and channelling effects.

The experimental results illustrate the need for careful design of the electron-detection system, especially for bright-field spectroscopy. Some of the essential reqirements are as follows.

(1) The material of the energy-selecting slit must be sufficiently thick to prevent penetration by X-ray photons with energies up to the primary-electron energy.It appears that 6 mm of brass or steel is sufficient for 100 keV operation; for higher voltages, it might be necessary to use lead sheet behind the main slits. The angle of the slit edges should be at least 80° so that X-rays generated by the zero-loss beam are absorbed by the full thickness of the lower slit when recording energy losed above a few hundred eV.

(2) The defining edges of the slit must be in the same plane so that there is no easy path available to stray electrons when the slit is almost closed to the spectrometer exit beam. The length of the slit in the non-dispersive direction should be restricted so that it is just sufficient

to accommodate small misalignments of the exit beam, due to stray magnetic fields for example.

(3) The slit blades and nearby reflecting surfaces should be "painted" with a layer of porous carbon (Egerton 1978b) which has a low backscattering coefficient ($\eta < 0.1$).

(4) Minimizing the surface area of the electron detector and increasing its separation from the slits will reduce the instrumental background since the stray electrons and X-rays are emitted isotropically whereas the spectrometer exit beam has a relatively small divergence (Kihn et al. 1980). Making the scintillator thin (around 100 μm) will minimize the amount of X-ray fluorescence. The use of electron-counting techniques at high energy loss should also help since some stray electrons and X-rays create detector-output pulses which fall below the discriminator threshold (Kihn et al. 1980).

In conclusion, the earlier findings that the core-edge signal/background ratio is increased by using dark-field illumination and thicker samples are confirmed, but only in the case where the instrumental background is high. As pointed out by Oikawa et al. (1984), elemental analysis using the dark-field EELS would require the calculation of "off-axis" partial cross sections. It appears more attractive to work under bright-field conditions and reduce the instrumental background to a low level by optimizing the design of the electron detector.

CHAPTER 4

DETERMINATION OF THE INELASTIC MEAN FREE PATH

4.1 INTRODUCTION

The inelastic mean free path is a useful concept in EELS. It is a quantity simply related to the stopping power of a medium containing free electrons, whose theoretical calculation has been of interest, and a quantity which may be determined from characteristic energy loss experiment. Also, the relative thickness of specimen is often expressed as the ratio of the absolute local thickness t to the inelastic mean free path λ, t/λ. A thin sample means that the sample thickness t is so small compared to the inelastic mean free path λ that the multiple-scattering processes can be ignored. In addition, it is desirable in many cases to know the absolute thickness of specimen as discussed later in Chapter 5. With known mean free path, the absolute local thickness of specimen can be experimentally determined from the log-ratio method (see later sections).

Many experimental measurements of the inelastic mean free path have been reported in the literature (Swanson and Powell 1966, Perez et al. 1977, Spence and Spargo 1970) These measurements were based on the Poisson probability distribution. It is known that electrons which have passed through a foil of thickness t suffer not only one energy loss, E, but in also any multiple n of E (Jouffrey and Sevely 1976). The multiple energy losses nE are more intense when the foil is thicker. The probability of n scattering events within a specimen with thickness t follows the Poisson distribution as:

$$P_n = \frac{1}{n!} \left(\frac{t}{\lambda}\right)^n \exp\left(\frac{-t}{\lambda}\right) \tag{4.1}$$

where λ is the mean free path for all inelastic scattering processes, and will be simply called the mean free path hereafter. According to Eq. (4.1), the probability P_n for n-fold energy losses increases with thickness, passing a maximum at $t/\lambda = n$. Based on this property, the mean free path was measured as the thickness of the specimen which gave the maximum intensity of the single plasmon loss (Spence and Spargo 1970).

The probability P_n may also be expressed as the ratio of the integrated intensity for the n-th scattering to the incident beam current or to the integrated intensity of the spectrum I_t. In other words,

$$P_n = \frac{I_n}{I_t} = \frac{1}{n!} \left(\frac{t}{\lambda}\right)^n \exp\left(\frac{-t}{\lambda}\right) \tag{4.2}$$

In the case of n = 0, Eq. (4.2) becomes:

$$t = \lambda \log_e\left(\frac{I_t}{I_o}\right) \tag{4.3}$$

where I_o is the integrated intensity over the zero-loss peak. Equation (4.3) has been used to determine the mean free path λ by measuring I_t and I_o from the energy-loss spectrum recorded from a standard specimen whose thickness has been calibrated independently. Similarly, the specimen thickness can be determined using Eq. (4.3) if the mean free path is known. Application of Eq. (4.3) has been referred to as the log-ratio method (Egerton and Cheng 1985). There are various ways for calibrating the thickness of a standard specimen. For example, for specimens prepared as evaporated or sputtered thin films, the thickness can be measured by the optical interferometry or their mass-thickness can be deduced by weighing the substrate before and after the deposition process (Chopra 1969, Burge and Misell 1968). For a specimen prepared as a wedge shaped crystal, the thickness can be calibrated by the thickness fringe method (Spence and Spargo 1970).

The mean free path not only depends on the chemical and physical properties of the specimen, but also depends on the incident electron energy and the maximum scattering angle accepted by the apert[illegible] the detector. The lack of agreement between the experimental measurements reported in the literature (Raether 1980, Blackstock et al. 1955, Horstmann and Meyer 1961) may be due to the different aperture size of the detector used in each experiment, due to different specimen conditions such as the presence of oxide layers or contamination, grain size and defect distribution, and due to errors in calibrating the specimen thickness (Tonomura and Watanabe 1967). The mean free path can also be calculated theoretically. Moderate agreement of the experimental results with the results calculated from the plasmon formula for aluminum crystal has been reported (Tonomura and Watanabe 1967, Jouffrey and Sevely 1976).

The present research was initiated in the attempt of applying the log-ratio method for the determination of the local thickness of specimen, which requires known values of the mean free paths. Preliminary results for the mean free path of thin films of Al, Cr, Ni, Cu, Ag and Au (measured by experiments based on the log-ratio method) are reported and discussed. These results are compared with the theoretical results predicted from the atomic model and from the plasmon formula. Calculations based on an atomic model and on a plasmon formula (assuming either a free electron gas or a jellium model) are also presented briefly.

4.2 CALCULATION FROM AN ATOMIC MODEL

An atomic model provides a means for calculating the inelastic cross section, which is related to the mean free path λ by:

$$\lambda = \frac{1}{n_a \sigma} \tag{4.4}$$

where n_a is the number of atoms per unit volume and σ is the inelastic cross section. If there is only one type of atom and the atomic mass is A, then

$$n_a = \frac{N_a \rho}{A}$$

where ρ is the density of the specimen; $N_a = 6.02 \times 10^{23}$ is Avogadro's number. Therefore, if n_a and σ are known, the mean free path λ can be calculated from Eq. (4.4).

The total cross section for inelastic scattering σ' is defined in terms of the sum of all possible inelastic collisions which may result from different processes. These processes are generally transitions of electrons from a ground to an excited state, including both the discrete and the continuum mode.

During an inelastic scattering event, an excitation energy $E = E_m - E_n$ may be transfered to an electron of an atom that is excited from the ground state (n) with energy E_n to the excited state (m) with energy E_m. The initial state of the system is characterized by $|\psi_i\rangle = |p_i, \epsilon_i\rangle$, where p_i and ϵ_i represent the momentum of the incident electron and the energy of the atom in the initial state i, respectively. The final state of the system is characterized by $|\psi_f\rangle = |p_f, \epsilon_f\rangle$, where p_f and ϵ_f represent the momentum of the electron and the energy of the atom in the final state f, respectively. According to the Golden rule, the probability of a transition from the state i to the state f per unit time, $\dot{P}(p_i, p_f)$, is given by the formula (Henoc 1979):

$$P(p_i, p_f) = \frac{2\pi}{\hbar} \langle p_f, \epsilon_f | V(r) | p_i, \epsilon_i \rangle^2 \rho(E_f) \tag{4.5}$$

in which V(r) and $\rho(E_f)$ designate the perturbation potential of the atom and the density of final states respectively.

Energy conservation of the system requires:

$$E_i = E_f$$

or

$$\frac{p_i^2}{2m_o} + \epsilon_i = \frac{p_f^2}{2m_o} + \epsilon_f \tag{4.6}$$

where m_o is the mass of the electron. The density of final states is related to the momentum by the equation (Henoc 1980):

$$\rho(E_f) = m_o p_f \tag{4.7}$$

The wave-functions of the initial and the final state are the products of the wave-functions for the electron and for the atom in the initial and the final state respectively:

$$\psi_i = \left(\frac{1}{2\pi\hbar}\right)^{3/2} \exp\left(\frac{i\mathbf{p}_i\cdot\mathbf{r}}{\hbar}\right) \Psi_i(\mathbf{r}_a) \tag{4.8a}$$

$$\psi_f = \left(\frac{1}{2\pi\hbar}\right)^{3/2} \exp\left(\frac{i\mathbf{p}_f\cdot\mathbf{r}}{\hbar}\right) \Psi_f(\mathbf{r}_a) \tag{4.8b}$$

where $\mathbf{r}$ and $\mathbf{r}_a$ are the coordinates of the incident electron and of the electron of the atom respectively.

Substituting Eqs. (4.6)-(4.8) into Eq. (4.5) and considering that the solid angle subtended by the detector is $d\Omega$, we have

$$P(p_i,p_f) =$$

$$\left|\iint \frac{1}{4\pi^2\hbar^4} \exp\left[\frac{-i(\mathbf{p}_f-\mathbf{p}_i)\cdot\mathbf{r}}{\hbar}\right] V(\mathbf{r})\,\Psi_f^*(\mathbf{r}_a)\Psi_i(\mathbf{r}_a)\,d^3r_a\,d^3r\right|^2 m_o p_f\, d\Omega \tag{4.9}$$

Since the incident electron flux is

$$J_i = [1/(2\pi\hbar)^3]p_i/m_o$$

we also have:

$$P(p_i, p_f) = \frac{1}{(2\pi\hbar)^3} \frac{p_i}{m_o} \sigma_{fi}(\theta)\ d\Omega \tag{4.10}$$

where $\sigma_{fi}(\theta)$ is the double-differential cross section corresponding to the transition from the initial state to the final state at a scattering angle θ. Thus, comparing Eq. (4.9) with Eq. (4.10) we have:

$$\sigma_{fi}(\theta) =$$

$$\frac{m_o}{4\pi^2\hbar^4} \frac{p_f}{p_i} \Bigg|\,\Bigg| \int \exp(-i(\mathbf{q}\cdot\mathbf{r})\ V(\mathbf{r})\ \Psi_f^*(\mathbf{r}_a)\Psi_i(\mathbf{r}_a) d^3r_a d^3r \Bigg|^2 \tag{4.11}$$

where $\mathbf{q} = (\mathbf{p}_f - \mathbf{p}_i)/\hbar$ is the scattering vector. Its magnitude is $q = \sqrt{k_o^2(\theta^2+\theta_E^2)}$, in which $k_o = \gamma m_o v/\hbar$ is the magnitude of the incident-electron wave vector and $\theta_E = E/\gamma m_o v^2$ is the characteristic angle corresponding to the energy loss E.

Setting

$$V(\mathbf{r}) = \frac{Z\,e^2}{r} - \sum_a \frac{e^2}{|\mathbf{r}-\mathbf{r}_a|} \tag{4.12}$$

where Z is the atomic number and the summation is taken over all the electrons in the atom, and using the Poisson formula to replace the potential with the charge according to the following expression:

$$\int \frac{\exp(-i\mathbf{q}\cdot\mathbf{r})}{|\mathbf{r}-\mathbf{r}_a|}\, d^3r = \frac{4\pi}{q^2}\int \delta(|\mathbf{r}-\mathbf{r}_a|)\exp(-i\mathbf{q}\cdot\mathbf{r})\, d^3r$$

$$= \frac{4\pi}{q^2}\exp(-i\mathbf{q}\cdot\mathbf{r}_a) \qquad (4.13)$$

Eq. (4.11) becomes:

$$\sigma_{fi}(\theta) =$$

$$\left(\frac{2e^2 m_o}{\hbar^2 q^2}\right)^2 \frac{k_f}{k_o} \left| \int \sum_a \exp(-i(\mathbf{q}\cdot\mathbf{r})\ \Psi_f^*(\mathbf{r}_a)\Psi_i(\mathbf{r}_a)\ d^3r_a \right|^2 \qquad (4.14)$$

where k_o is the magnitude of the incident-electron wave vector as before; and k_f is the magnitude of the transmitted-electron wave vector.

The differential cross-section for inelastic scattering $d\sigma(\theta)/d\Omega$ at an angle θ is obtained by summing over all possible transitions and taking account of the fact that $|k_f/k_o| \simeq 1$, i.e.,

$$\frac{d\sigma(\theta)}{d\Omega} = \sum_{f\neq i} \sigma_{fi}(\theta) \simeq$$

$$\left(\frac{2e^2 m_o}{\hbar^2 q^2}\right)^2 \sum_{f\neq i} \left| \int \sum_a \exp(-i(\mathbf{q}\cdot\mathbf{r})\ \Psi_f^*(\mathbf{r}_a)\Psi_i(\mathbf{r}_a) d^3r_a \right|^2 \qquad (4.15)$$

Further calculation will depend on the forms of Ψ_i and Ψ_f.

If the Wentzel model is used for the potential of the atom (Lenz 1954) and the mean value $\bar{E} = (13.5/2)Z$ in eV is used for E involved in q (Koppe 1948), then an analytical formula can be derived from Eq. (4.15) (Reimer 1984):

$$\frac{d\sigma}{d\Omega} \simeq \frac{4\gamma^2 Z}{a_o^2 q^4}\left[1 - \frac{1}{(1 + q^2 r_o^2)^2}\right] \tag{4.16}$$

where $\gamma = \surd(1-v^2/c^2)$; $q = \surd k_o^2(\theta^2+\bar{\theta}_E^2)$ in which $k_o = \gamma m_o v/\hbar$ as before and $\bar{\theta}_E = \bar{E}/\gamma m_o v^2$ is the characteristic angle corresponding to the mean energy loss $\bar{E}$; a_o is the Bohr radius and $r_o = a_o Z^{-1/3}$. Equation (4.16) can be expressed as a more explicit form for the angular dependence (Colliex and Mory 1984):

$$\frac{d\sigma}{d\Omega} \simeq \frac{4\gamma^2 Z}{a_o^2 k_o^4}\,\frac{1}{(\theta^2 + \theta_E^2)^2}\left[1 - \left(1 + \frac{\bar{\theta}_E^2}{\theta_o^2} + \frac{\theta^2}{\theta_o^2}\right)^{-2}\right] \tag{4.17}$$

where $\theta_o = 1/k_o r_o$.

Assuming the angle θ is in the range $\bar{\theta}_E \ll \theta < \theta_o$ and ignoring the terms inside the bracket whose orders are higher than 2, Eq. (4.17) takes the form of the Lorentzian angular distribution:

$$\frac{d\sigma}{d\Omega} \simeq \frac{8\gamma^2 Z}{a_o^2 k_o^4}\,\frac{1}{(\theta^2 + \bar{\theta}_E^2)\theta_o^2} \tag{4.18}$$

Integrating the Lorentzian angular distribution up to the collecting angle β gives:

$$\sigma(\beta) \simeq \frac{8\pi\gamma^2 Z r_o^2}{a_o^2 k_o^2} \log_e(1 + \frac{\beta^2}{\bar{\theta}_E^2})$$

$$= \frac{8\pi\gamma^2 Z^{1/3}}{k_o^2} \log_e(1 + \frac{\beta^2}{\bar{\theta}_E^2}) \qquad (4.19)$$

Taking $\theta_c = (2\bar{\theta}_E)^{1/2}$ as the cutoff angle (Colliex and Mory 1984) and integrating the Lorentzian angular distribution up to the cutoff angle gives the total-inelastic cross section:

$$\sigma \simeq \frac{8\pi\gamma^2 Z^{1/3}}{k_o^2} \log_e(\frac{2}{\bar{\theta}_E}) \qquad (4.20)$$

Finally, using Eq. (4.4) the expression for the mean free path is obtained:

$$\lambda(\beta) \simeq \frac{k_o^2}{8\pi\gamma^2 Z^{1/3} n_a} \left[\log_e(1 + \frac{\beta^2}{\bar{\theta}_E^2})\right]^{-1} \qquad (4.21)$$

Thus, if the chemical composition and the density of the specimen are known, the mean free path may be estimated from Eq. (4.21).

4.3 CALCULATION FROM A PLASMON FORMULA

Inelastic electron scattering in solids can be described in terms of a complex dielectric constant $\epsilon = \epsilon_1 + i\epsilon_2$, which is a function of the angular frequency ω of the oscillation and the scattering vector **q**. For **q** = 0, the dielectric constant is related to the familiar optical constants: the refractive index n and the extinction coefficient κ. From electrodynamic theory, the double-differential inelastic scattering cross section, per atom or molecule, for energy loss $E = \hbar\omega$ and momentum transfer $\hbar q$ in an infinite medium is (Ritchie 1957):

$$\frac{d^2\sigma}{d\Omega dE} = \frac{\mathrm{Im}(-1/\epsilon)}{\pi^2 a_0 m_0 v^2 n_a (\theta^2+\theta^2_E)} \qquad (4.22)$$

where $d\Omega = 2\pi\theta d\theta$; $\theta_E = E/(\gamma m_0 v^2)$ as before. In Eq. (4.22), the energy loss function $\mathrm{Im}(-1/\epsilon)$ introduces the macroscopic dielectric constant ϵ and describes the response of the electron gas to the perturbation introduced by the incident electron. If $\mathrm{Im}(-1/\epsilon)$ can be computed, the total cross section may be obtained.

In the free-electron-gas model, the energy-loss peak is assumed to be infinitely narrow and is treated as a delta function. The energy loss function can then be written as (Raether 1980):

$$\mathrm{Im}(-1/\epsilon) = \frac{\pi}{2}\,\omega_p\,\delta(\omega - \omega_p) \qquad (4.23)$$

where ω_p is the eigenfrequency of longitudinal oscillations in the electron gas, and corresponds to the eigenenergy of the eletron gas, E_p; ω_p is defined by:

$$\omega_p = \left[\frac{n_e e^2}{\epsilon_o m}\right]^{1/2} \qquad (4.24)$$

where n_e is the number of electro per unit volume; ϵ_o is the permitivity in vaccum; and m is the effective mass of an electron which differs from the rest mass m_o.

Substituting Eq. (4.23) into Eq. (4.22) and integrating Eq. (4.22) over all energy range and up to the collecting angle β, the integral cross section per atom (or per molecule) is:

$$\sigma(\beta) = \frac{E_p}{n_a a_o m_o v^2}\,\log_e\!\left(\frac{\beta}{\theta_E}\right) \qquad (4.25)$$

Assuming a sharp cutoff intensity at θ_c, where $\theta_c = E_p/\hbar k_o v_f$ in which v_f is the Fermi velocity, and integrating Eq. (4.22) over all energy and up to the cutoff angle θ_c, the total-inelastic cross section per atom is obtained:

$$\sigma = \frac{E_p}{n_a a_o m_o v^2} \log_e\left(\frac{\theta_c}{\theta_E}\right) \tag{4.26}$$

Applying Eq. (4.4) the mean free path can be written as (Raether 1980):

$$\lambda(\beta) = \frac{a_o m_o v^2}{E_p}\left[\log_e\left(\frac{\beta}{\theta_E}\right)\right]^{-1} \tag{4.27}$$

However, an energy-loss peak recorded in EELS has always a certain width and may not be taken as the delta function. The jellium model takes the width of the energy-loss peak into consideration by introducing the damping constant Γ or the relaxation time τ. They are related to the halfwidth of the energy-loss peak $E_{1/2}$ by $\tau = \hbar/E_{1/2}$ and $\Gamma = E_{1/2}/\hbar$, respectively. Therefore, derivation of the mean free path from the jellium model has been attempted and an extra term for the inelastic scattering cross section has been found compared to the expression derived from the model of the free electron gas. The derivation of the mean free path from the jellium model is ~~given~~ below.

Assume the displacement ~~$\mathbf{x}$ of~~ electron due to an applied electric field $\mathbf{E}$ must satisfy the equation of motion:

$$m\ddot{\mathbf{x}} + m\Gamma\mathbf{x} = -e\mathbf{E} \tag{4.28}$$

where m is the effective mass of electron as before; Γ is the damping constant whose reciprocal is the relaxation time τ. Then, for an oscillatory field $\mathbf{E} = E_o \exp(-i\omega t)$, Eq. (4.28) has the following solution:

$$\mathbf{x} = \frac{e\mathbf{E}}{m}\,(\omega^2 + i\,\Gamma\omega)^{-1} \tag{4.29}$$

The displacement **x** gives rise to a polarization:

$$\mathbf{p} = -e\,n_e\,\mathbf{x} = \epsilon_o \chi\,\mathbf{E}$$

where χ is the electronic susceptibility. The relative permittivity or dielectric function then takes the following form:

$$\begin{aligned} \epsilon(\omega) &= 1 + \chi \\ &= 1 - \frac{\omega_p^2}{\omega^2+\Gamma^2} + \frac{i\,\Gamma\,\omega_p^2}{\omega(\omega^2+\Gamma^2)} \end{aligned} \tag{4.30}$$

where ω is the angular frequency and $\omega_p = E_p/\hbar$ is the eigenfrequency for plasma oscillation as before. From Eq. (4.30) the energy-loss function can be expressed as:

$$\mathrm{Im}\left[\frac{-1}{\epsilon(\omega)}\right] = \frac{E_p^2\,(E\hbar/\tau)}{(E^2 - E_p^2)^2 + E^2\hbar^2/\tau^2} \tag{4.31}$$

Substituting Eq. (4.31) into Eq. (4.22) and noticing $\theta_E = E/2\gamma T$, where $T = m_o v^2/2$, we have

$$\frac{d\sigma}{d\Omega dE} = \frac{1}{\pi^2 a_o m v^2 n_a} \frac{E_p^2 E(\hbar/\tau)}{(E^2-E_p^2)^2+(E\hbar/\tau)^2} \frac{1}{\theta^2+(E/2\gamma T)^2} \qquad (4.32)$$

Integrating over all energy range, Eq. (4.32) becomes:

$$\frac{d\sigma}{d\Omega} = \frac{E_p^2(\hbar/\tau)}{\pi^2 a_o m v^2 n_a} \int_0^\infty \frac{E\, dE}{[(E^2-E_p^2)^2+(E\hbar/\tau)^2]\,[\theta^2+(E/2\gamma T)^2]}$$

$$= \frac{E_p}{2\pi a_o m v^2 n_a ({\theta'_E}^2+\theta^2)} + \frac{E_p^2(\hbar/\tau)}{4\pi^2 a_o m v^2 n_a \gamma^2 T^2} \frac{\log_e(\theta'_E/\theta)}{({\theta'_E}^2+\theta^2)^2} \qquad (4.33)$$

where $\theta'_E = E_p/\gamma m_o v^2$.

Integrating Eq. (4.33) up to an angle β gives the integral cross section per atom:

$$\sigma(\beta) =$$

$$\frac{E_p \log_e(\beta/\theta'_E)}{n_a a_o m v^2} + \int_0^\beta \frac{E_p^2(\hbar/\tau)}{2\pi a_o m v^2 n_a \gamma^2 T^2} \frac{\log_e(\theta'_E/\theta)}{2({\theta'_E}^2+\theta^2)^2}\, \theta\, d\theta \qquad (4.34)$$

The first term in the right hand of Eq. (4.34) has the same form as that in Eq. (4.25) derived from the free electron formula. The second term in the right hand of Eq. (4.34) is, however, an extra term compared with Eq. (4.25). This term can be further computed as:

$$\sigma_{ex} = \int_0^{\beta} \frac{E_p^2(\hbar/\tau)}{2\pi a_o m v^2 n_a \gamma^2 T^2} \cdot \frac{\log_e(\theta'_E/\theta)}{2(\theta_E'^2+\theta^2)^2}\, \theta\, d\theta$$

$$= \frac{E_{1/2}}{\pi a_o m v^2 n_a}\left[\frac{\log_e(\beta/\theta'_E)}{1+(\beta/\theta'_E)^2} + \log_e\sqrt{[1+(\theta'_E/\beta)^2]}\right] \qquad (4.35)$$

where $E_{1/2} = \hbar/\tau$ is the halfwidth of the enegy-loss peak as before. For most materials, the ratio of $E_{1/2}$ to E_p is in the range of 3% to 30% (Raether 1980). Therefore, if the magnitude of the collecting angle β is similar to that of θ'_E, the extra term σ_{ex} will have a considerable contribution to the inelastic cross section. Since ~~the~~ value of θ'_E increases with decreasing energy of the incident electron, the contribution of σ_{ex} may be important when the incident electron energy is low. At normal experimental conditions, for example, $\beta \simeq 10$ mrad and $\theta'_E \simeq 0.1$ mrad, the contribution of the term σ_{ex} is negligible.

4.4 EXPERIMENTAL

The mean free path was measured based on Eq. (4.3). Thin films of Al, Cr, Cu, Ni, Ag , Au, C and SnO_2 were prepared by evaporation from tungsten or molybdenum wires (or boats) in a standard vacuum system described in Chapter 2. The vapours were condensed onto unheated glass substrates, 22 mm square and of 0.15 mm thickness. To obtain an independent measurement of thickness, a sensitive microbalance was used to weigh the substrate before and after deposition with a precision (determined by repeated weighing) of ±2 μg, equivalent to an accuracy of ±(6/ρ) nm in the thickness determination for a deposit of density ρ g/cm²: To convert the weight difference into a film thickness, the bulk density of each metal was used. In most cases, a very thin layer of a water-soluble organic compound, (Victawet, available from E.F. Fulham Inc., P.O. Box 444, Schenectady, N.Y. 12301, U.S.A.), was evaporated onto the glass before the first weighing to ensure that portions of the metal film could later be float very toped onto the surface of deionized water and caught on 400-mesh electron-microscope grids.

The specimens were examined in a JEM-100B electron microscope. Spectra from clean, flat areas of film were recorded serially with defocussed illumination and an image of magnification 5000 at the level of the CTEM screen. The detection slit of the Gatan 607 electron spectrometer was set to give an energy resolution of 3 eV; an instrumental 'tail' to the right of the zero-loss peak was avoided either by scanning downwards in energy loss or by recording spectra in the electron-counting mode. To avoid non-linearity of the detector response, all count rates were kept below 1 MHz.

4.5 RESULTS AND DISCUSSION

The linear relation of Eq. (4.3) was tested at various collecting semi-angle β (5-20 mrad). Figures. 4.1(a)-4.1(g) show that for films of Al, Cr, Ni, Cu, Ag, Au and C at a limited aperture size, Eq. (4.3) is applicable over a wide range of specimen thickness, typically 10-500 nm at the incident energy E_o = 100 keV, and the linear relation between t and $\log_e(I_t/I_o)$ has an accuracy about 10% in the range of $0.2<t/\lambda<5$.

The experimental results of the inelastic mean free path obtained at an incident electron energy E_o = 100 keV have been plotted as the function of the collecting aperture, semi-angle, β, in Figs. 4.2(a)-4.2(e) for films of Al, Cr, Ni, Ag and Au. Also plotted in Figs. 4.2(a)-4.2(e) are the calculated inelastic cross sections and the inelastic mean free paths (as a function of β) calculated from the atomic model [Eqs. (4.19) and (4.21)] and from the plasmon model [Eqs. (4.25)-(4.27)]. The parameters used in the calculations are shown in Table 4.1. In the calculation from the plasmon formula, E_p was taken as the measured loss of the main loss peak. In the calculation from the atomic

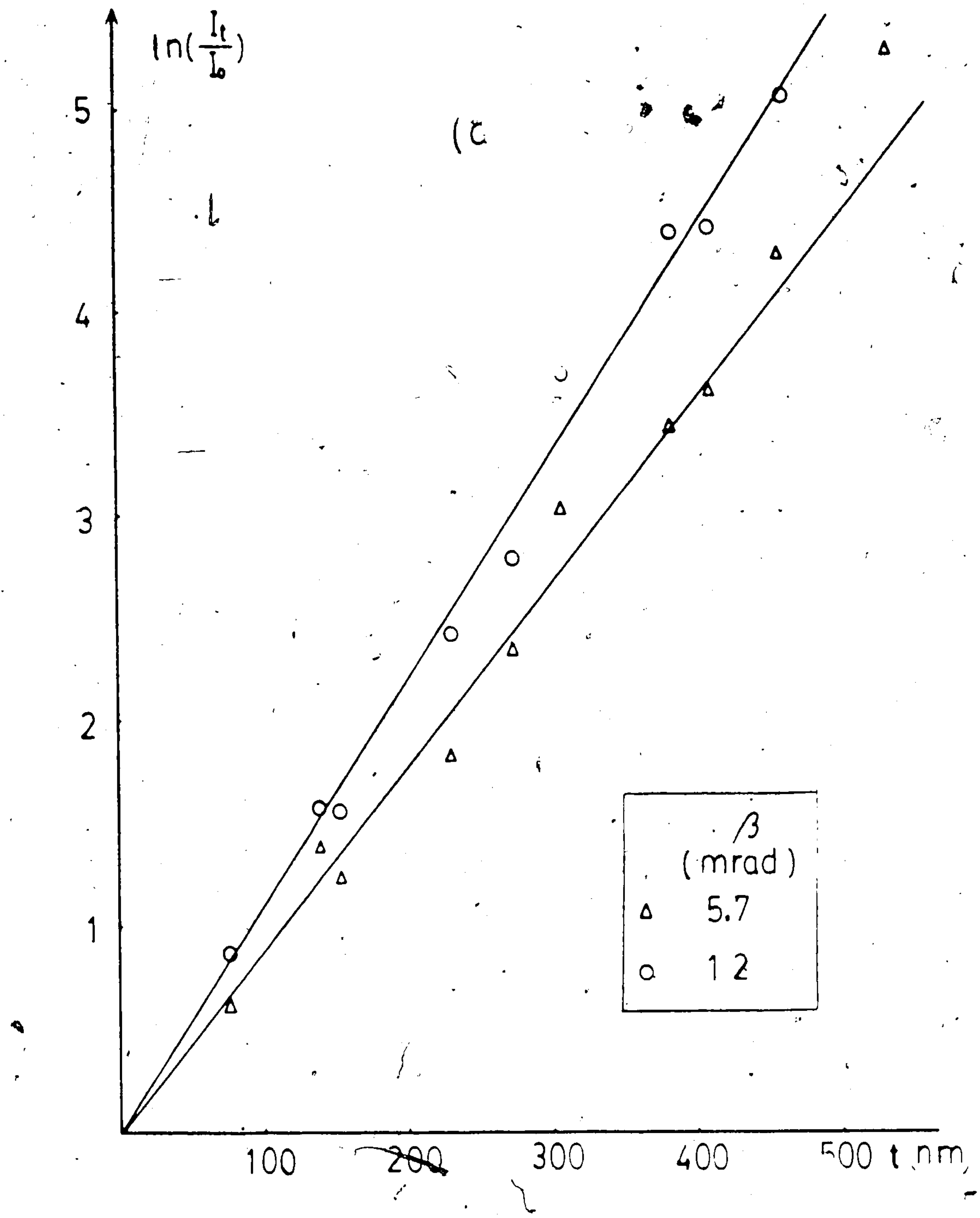

Fig. 4.1. Plots of specimen thickness t vs. $\log_e(I_t/I_o)$ for films of (a) Al, (b) Cr, (c) Ni, (d) Cu, (e) Ag, (f) Au, and (g) C. E = 100 keV. Δ ≃ 500 eV. For all materials except Al, β = 5.3 mrad.

(to be continued)

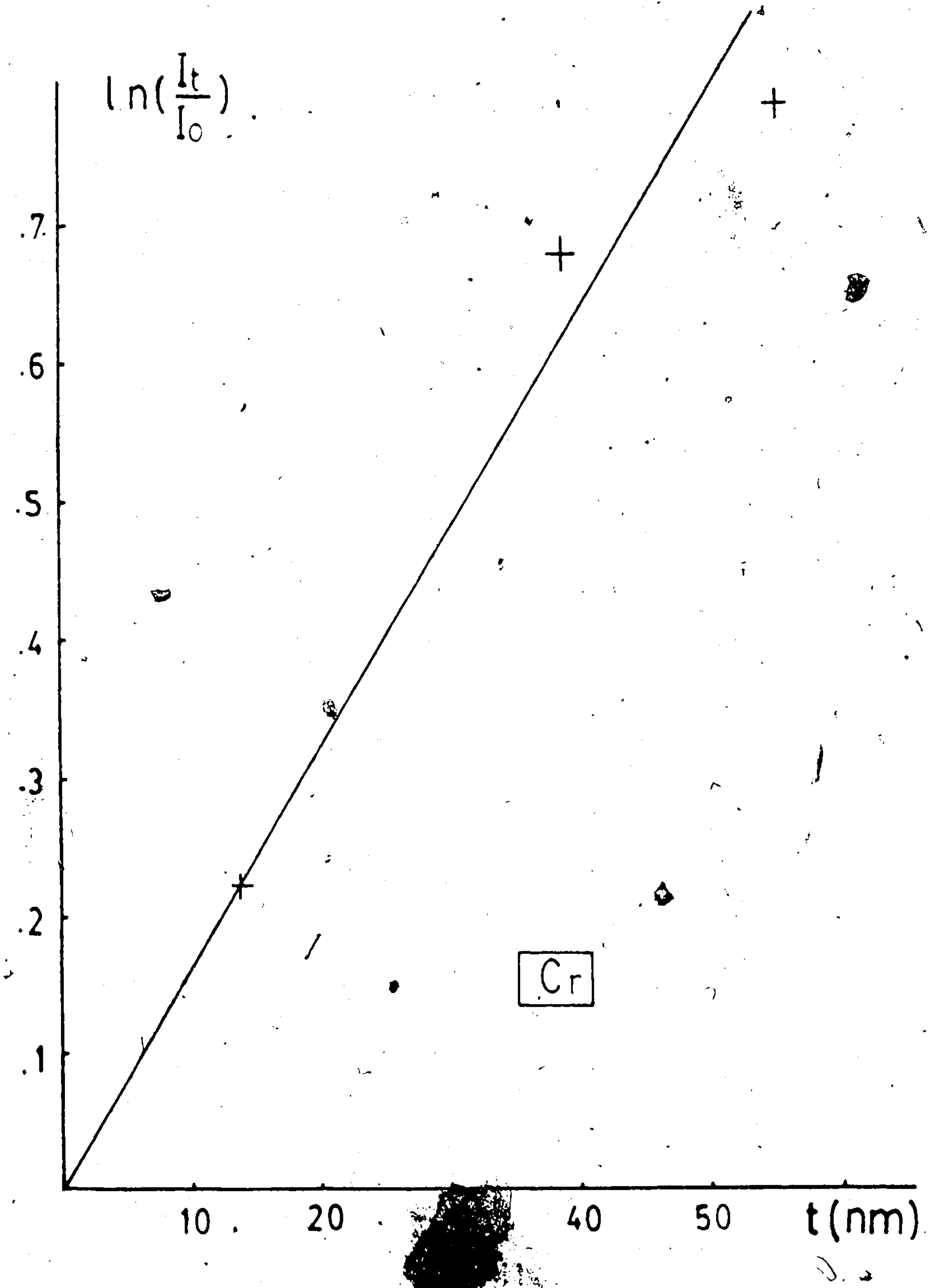

(Fig. 4.1 continued) Fig. 4.1(b)

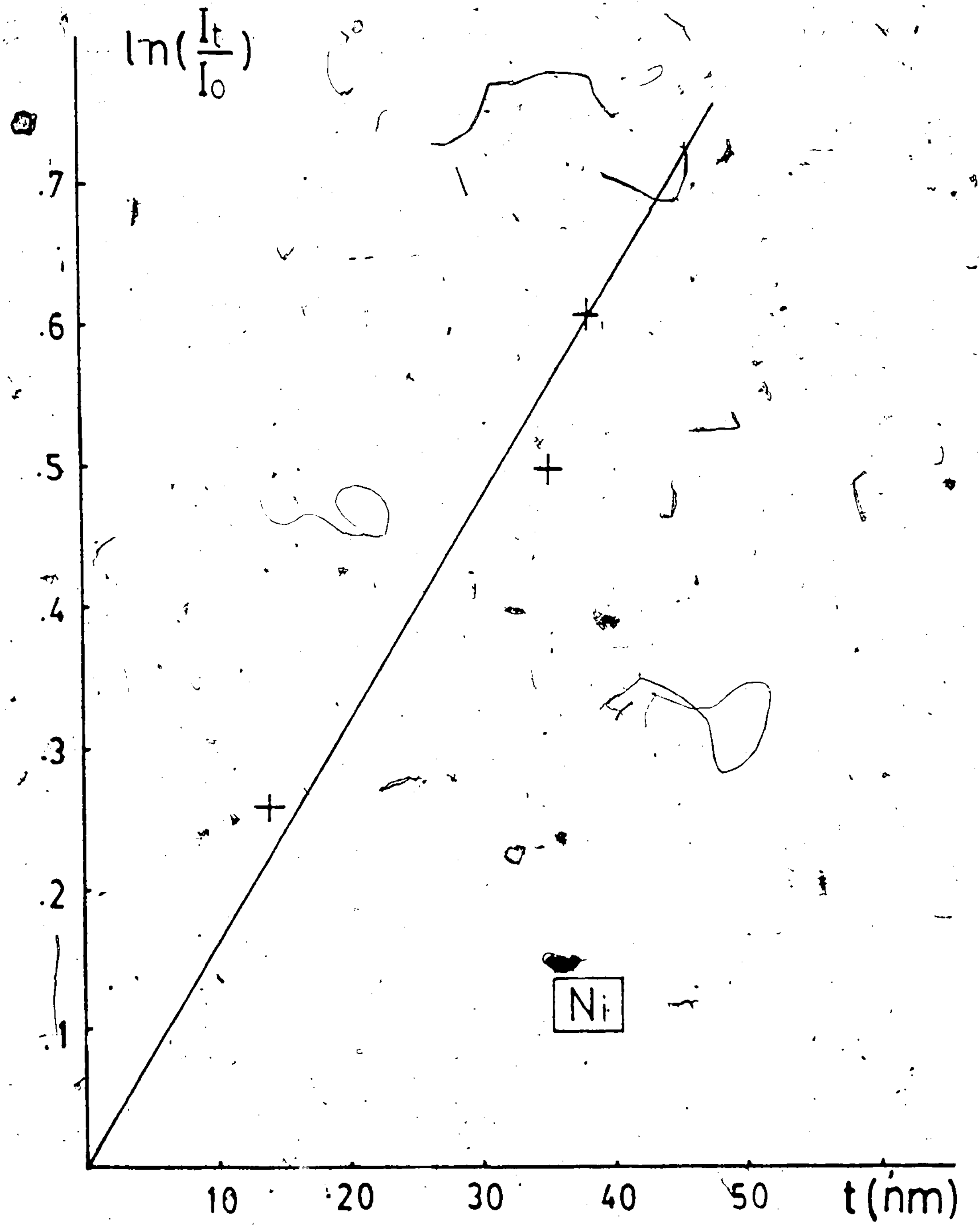

(Fig. 4.1 continued) Fig. 4.1(c)

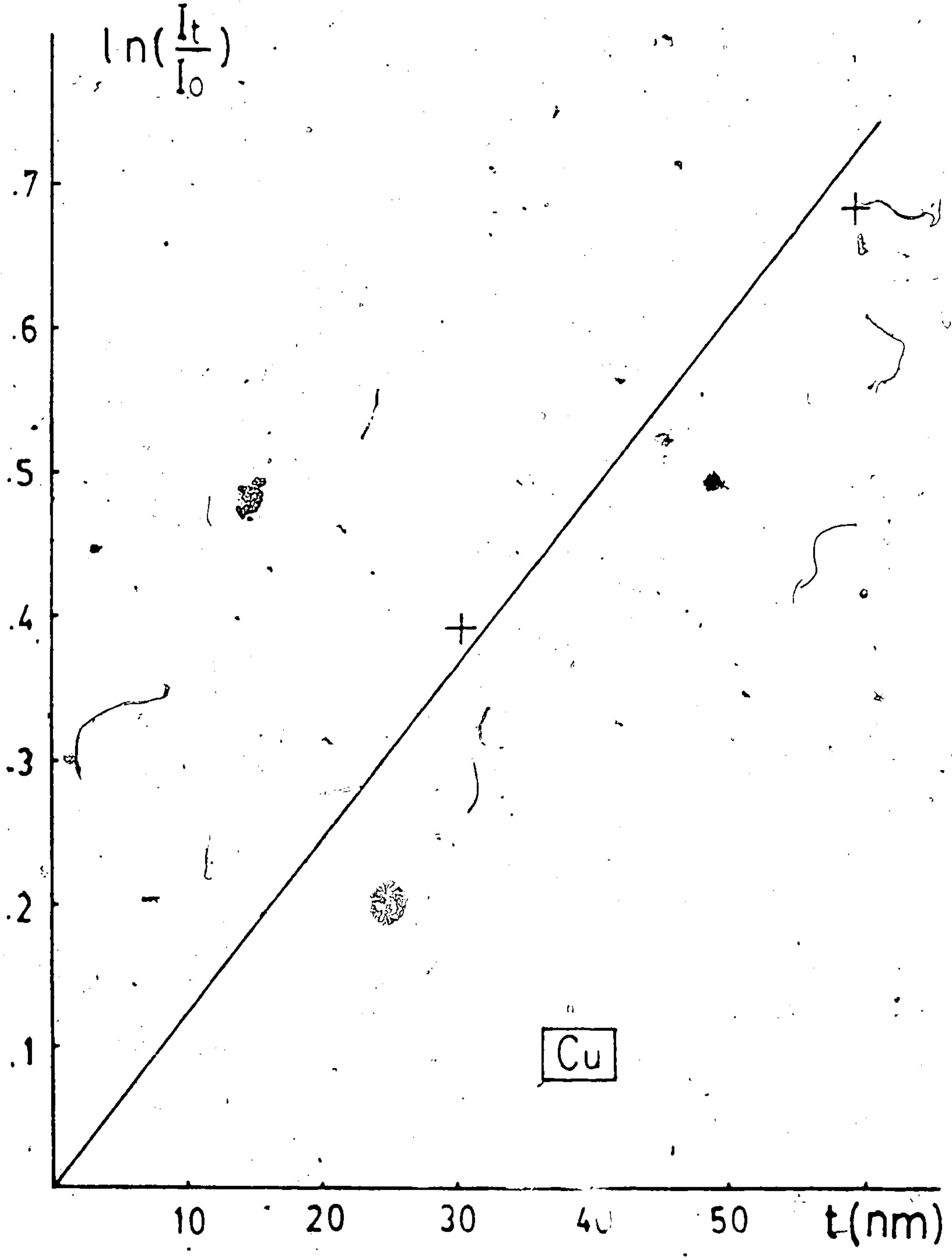

(Fig. 4.1 continued) Fig. 4.1(d)

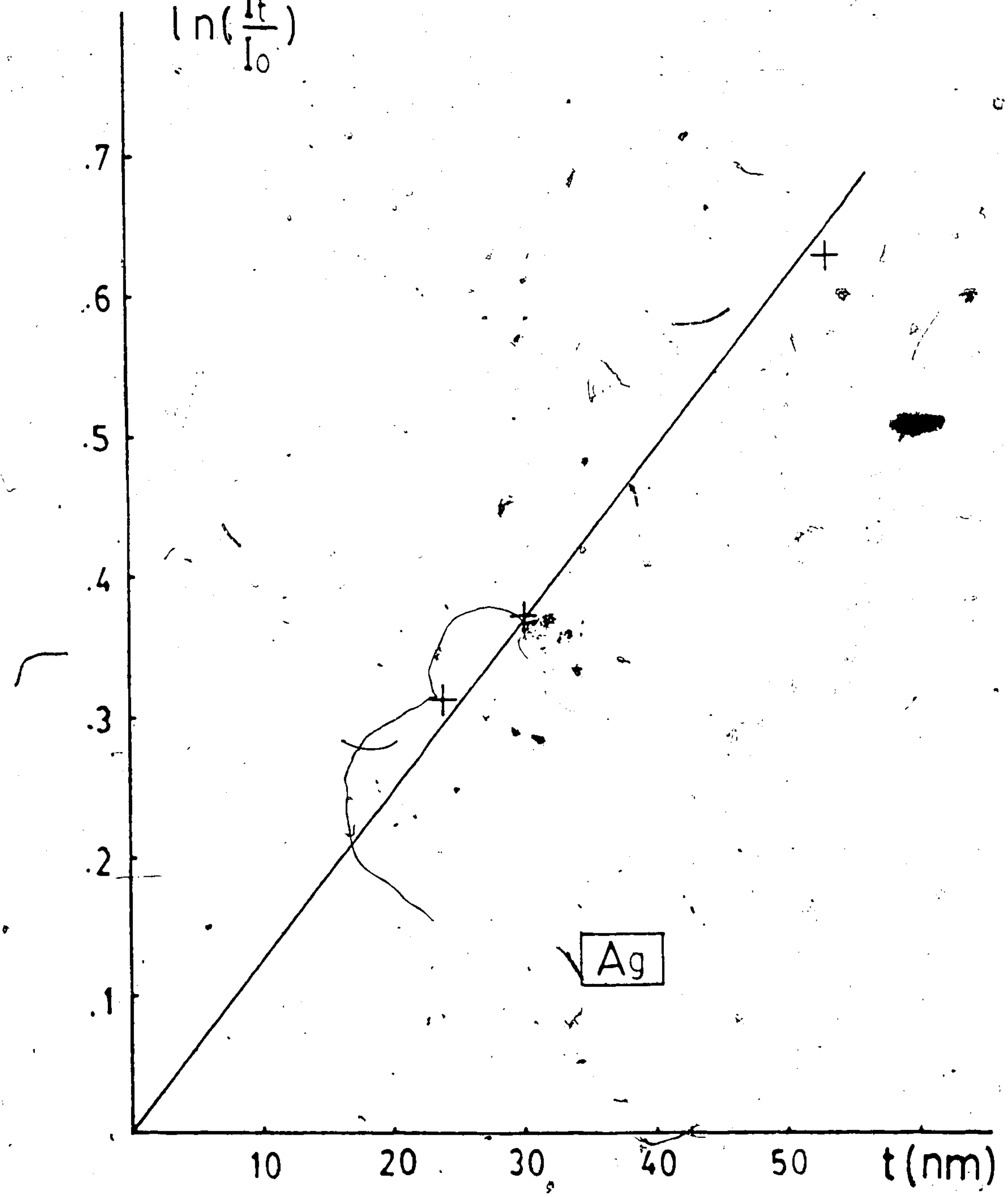

(Fig. 4.1 continued)

Fig. 4.1(e)

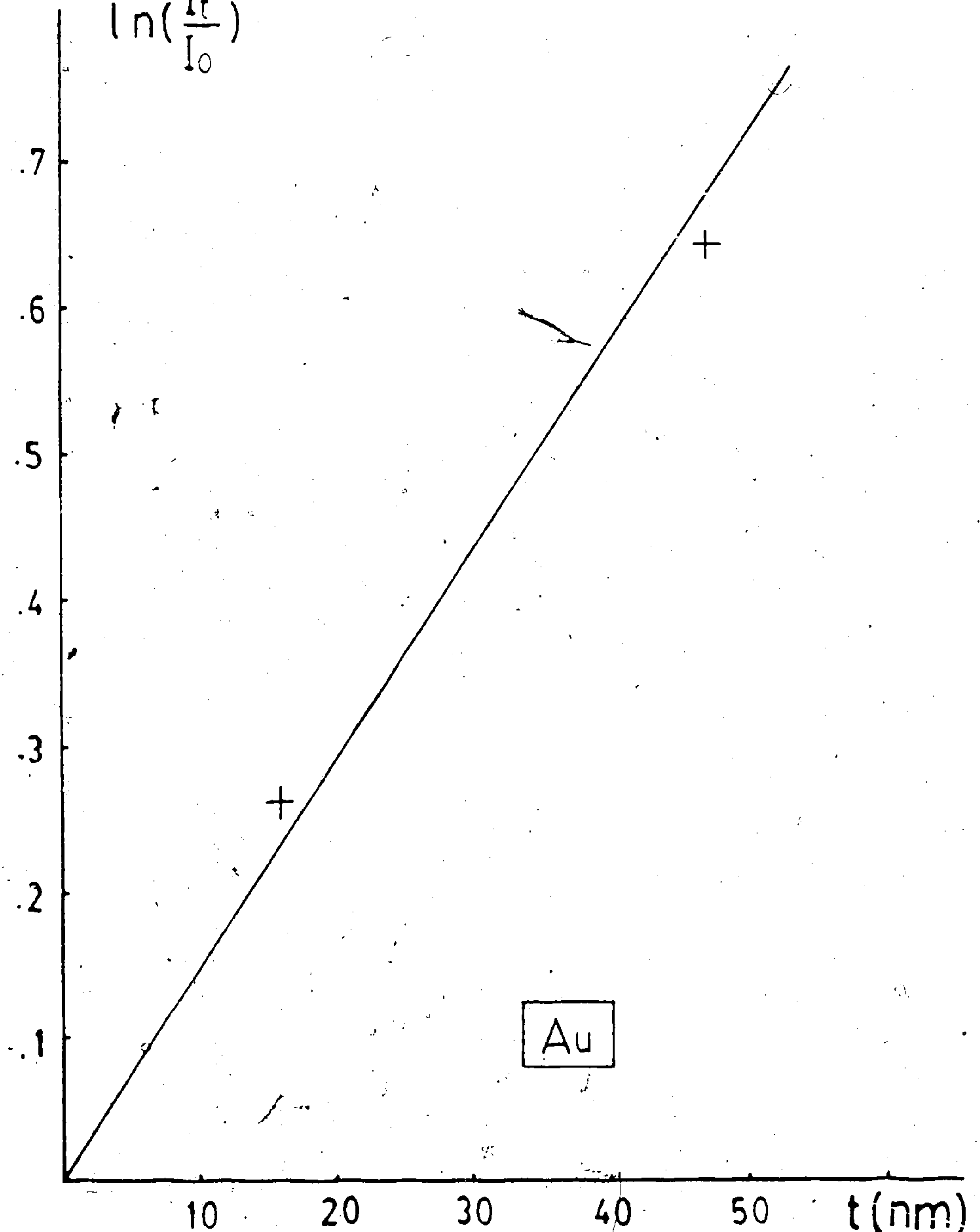

(Fig. 4.1 continued)

Fig. 4.1(f)

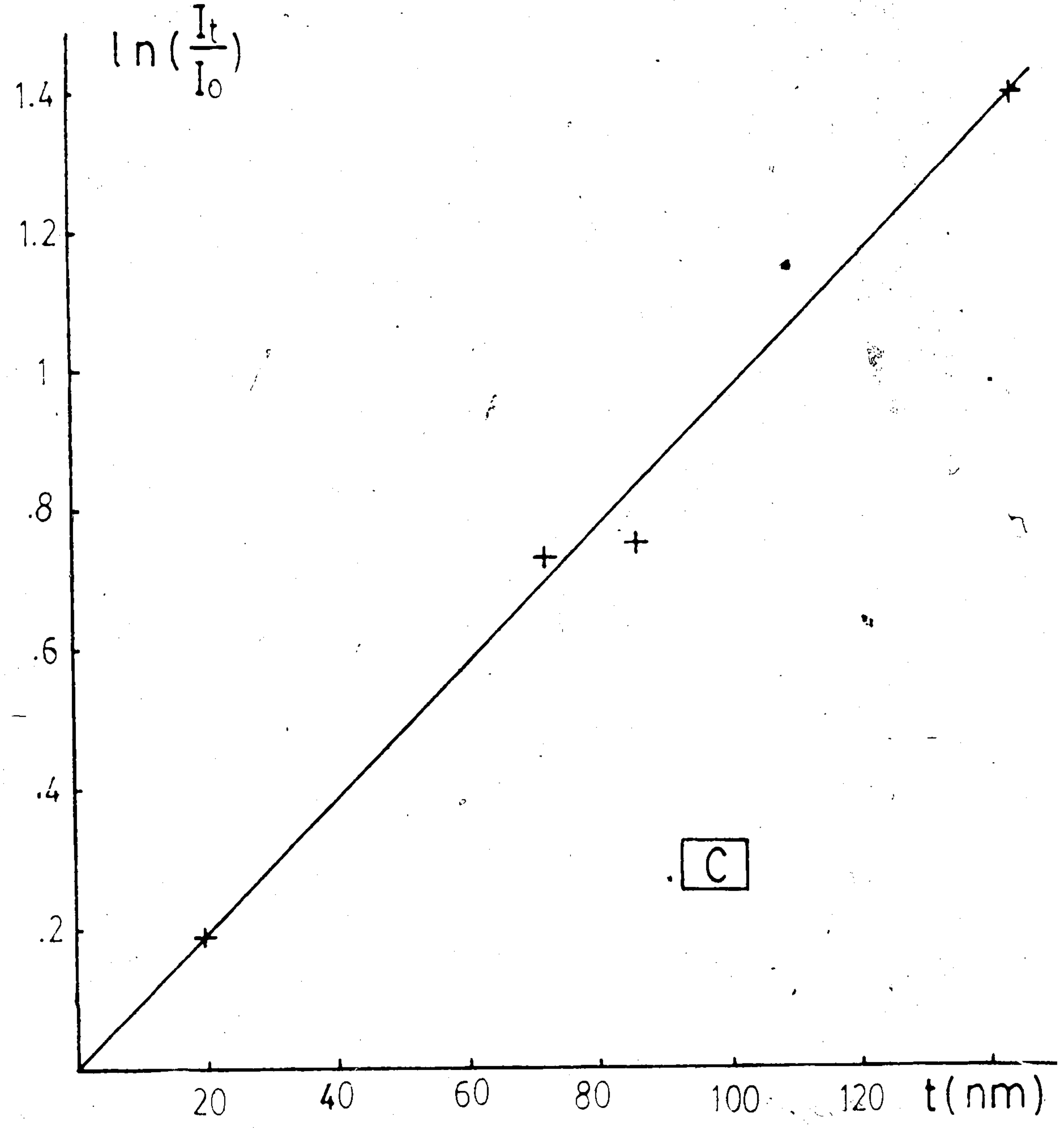

(Fig. 4 1 continued)

Fig. 4.1(g)

Table 4.1 Parameters used in calculating the mean free path from an atomic model and plasmon formula

Material	Z	ρ (g/cm^3)	n_a (10^{23}/cm^3)	E_p* (eV)	θ_E† (mrad)	θ_c‡ (rmad)
C	6	2.0	0.10	24.0	0.13	7.1
Al	13	2.7	0.60	15.0	0.082	7.7
Cr	24	7.2	0.86	26.8	0.15	–
Ni	28	8.9	0.91	20.7	0.11	–
Cu	29	8.96	0.84	19.3	0.11	11.0
Ag	47	10.5	0.59	25.0	0.14	15.9
Au	79	19.3	0.59	29.0	0.16	19.0

* Measured loss of the main loss peak.

† Calculated as $\theta_E = E_p/\gamma m_o v^2$ in which $m_o v^2 = 154$ keV ($E_o = 100$ keV).

‡ Cutoff angle in the plasmon formula $\theta_c = E_p/\hbar k_o v_f$. No v_f data is available for Cr and Ni.

model, the average energy loss $\bar{E}$ involved in the term $\bar{\theta}_E$ was also taken as the measured loss of the main loss peak. Figures 4.2(a)-4.2(e) show that the measured mean free path increases ~~with~~ decreasing collecting angle β. This trend is in agreement with that predicted from the atomic model, in which the cutoff angle is large; but only agrees with that predicted from the plasmon formula at $\theta<\theta_c$. Figures 4.2(a)-4.2(e) also show that the atomic model underestimates $\lambda(\beta)$ by a factor up to 3, especially for free-electron metals such as Al. The error may be due to the solid-state effect (Egerton 1986). The mean free path calculated from the plasmon formula is generally too high compared with the experimental data, except for Al and Ag at relatively low semi-angles. This may be due to the inner-shell contributions and the band-structure effects which are not considered in the plasmon model.

The measured mean free paths λ for all inelastic scattering processes occurring withing the recorded energy range for different materials are plotted in Fig. 4.3, together with the datum obtained by Malis (Malis et al. 1987). Figure 4.3 shows that λ generally decreases with increasing (mean) atomic number $\bar{Z}$. The $\bar{Z}$-dependence can be approximated by a power law $\lambda \propto \bar{Z}^{-0.3}$. It happens that this $\bar{Z}$-dependence is similar to that predicted from the atomic model [Eq. (4.21)]. From the measured λ-$\bar{Z}$ graph an empirical formula, including also the β- and E_0-dependences expected on the basis of electron-scattering theory [plasmon formula,

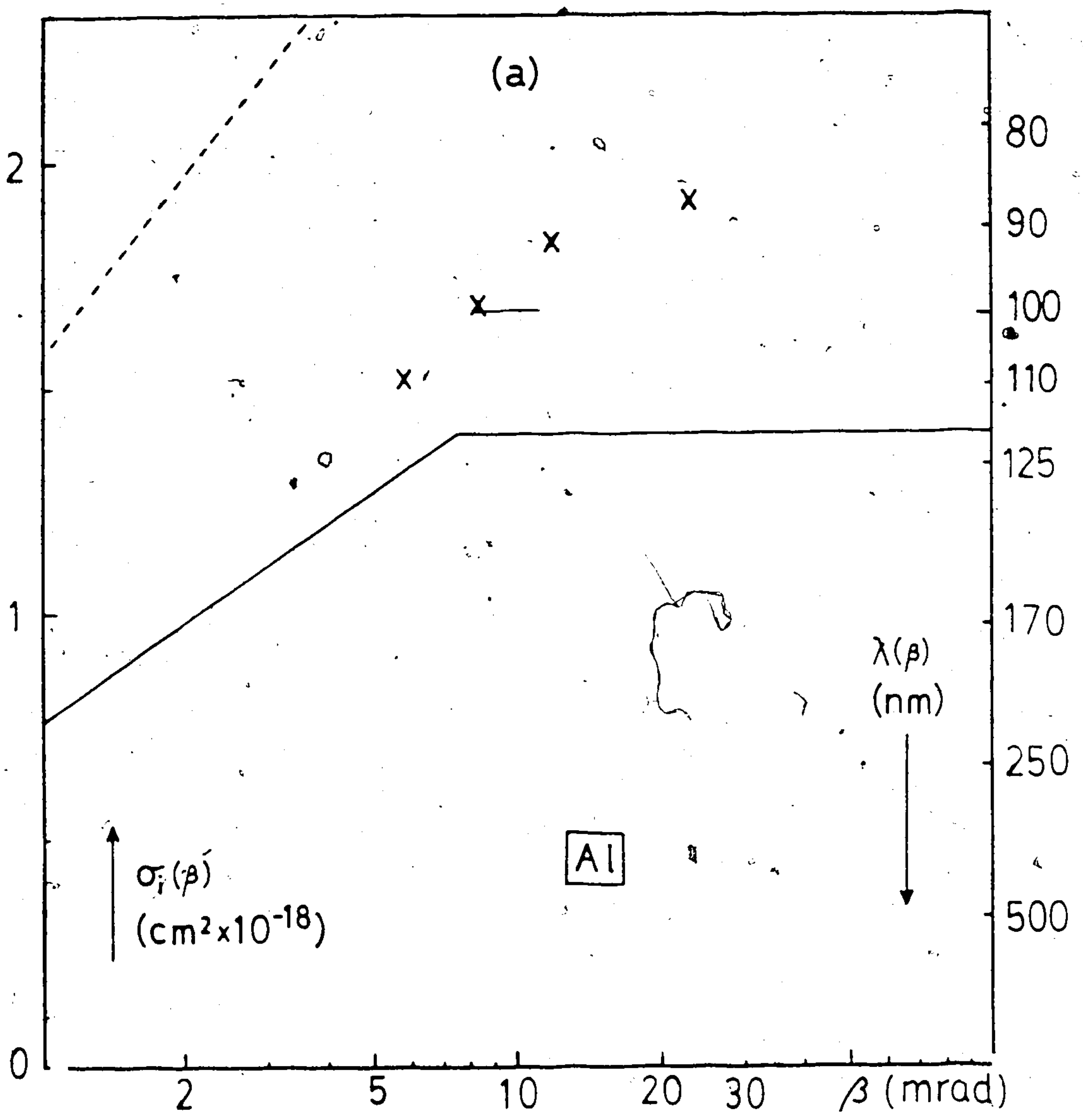

Fig. 4.2. The calculated and the measured mean free path as a function of the collecting semi-angle β for films of (a) Al, (b) Cr, (c) Ni, (d) Ag and (e) Au. The symbols are the measured results. The dashed and solid lines represent the ones calculated from the atomic model and the plasmon formula respectively. E_o = 100 keV.

(to be continued)

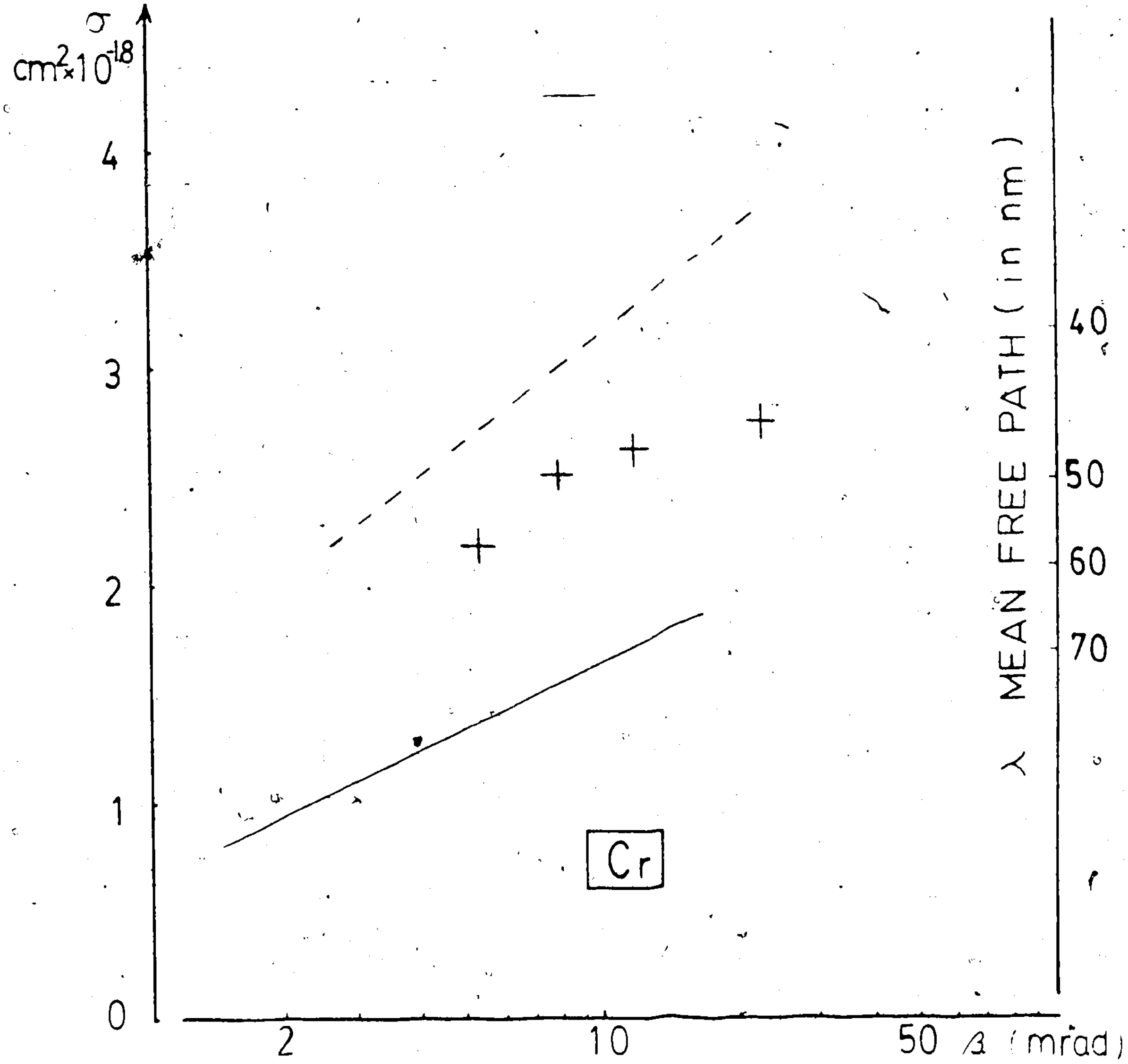

(Fig. 4.2 continued)

Fig. 4.2(b)

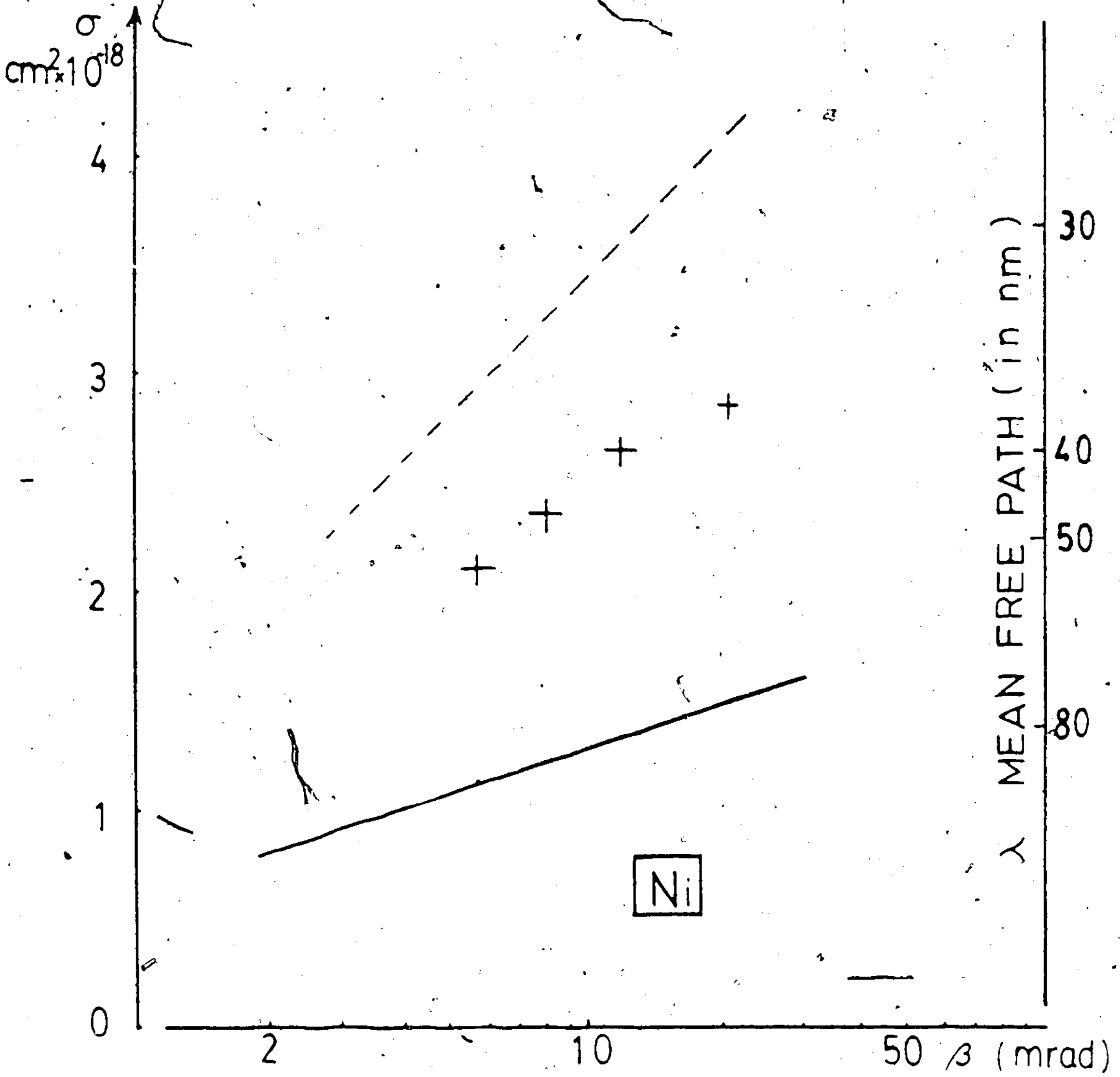

(Fig. 4.2 continued)

Fig. 4.2(c)

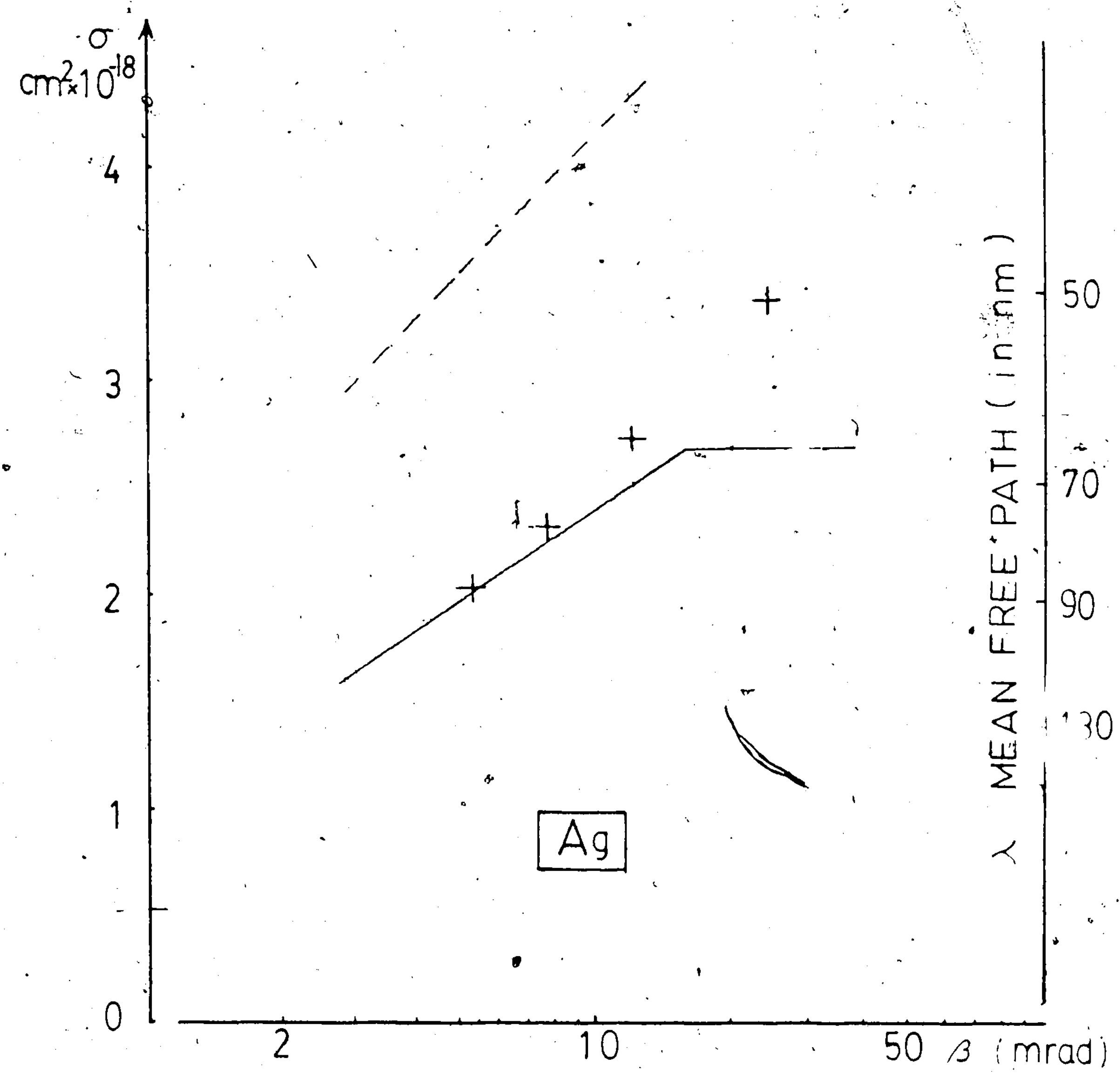

(Fig. 4.2 continued)

Fig. 4.2(d)

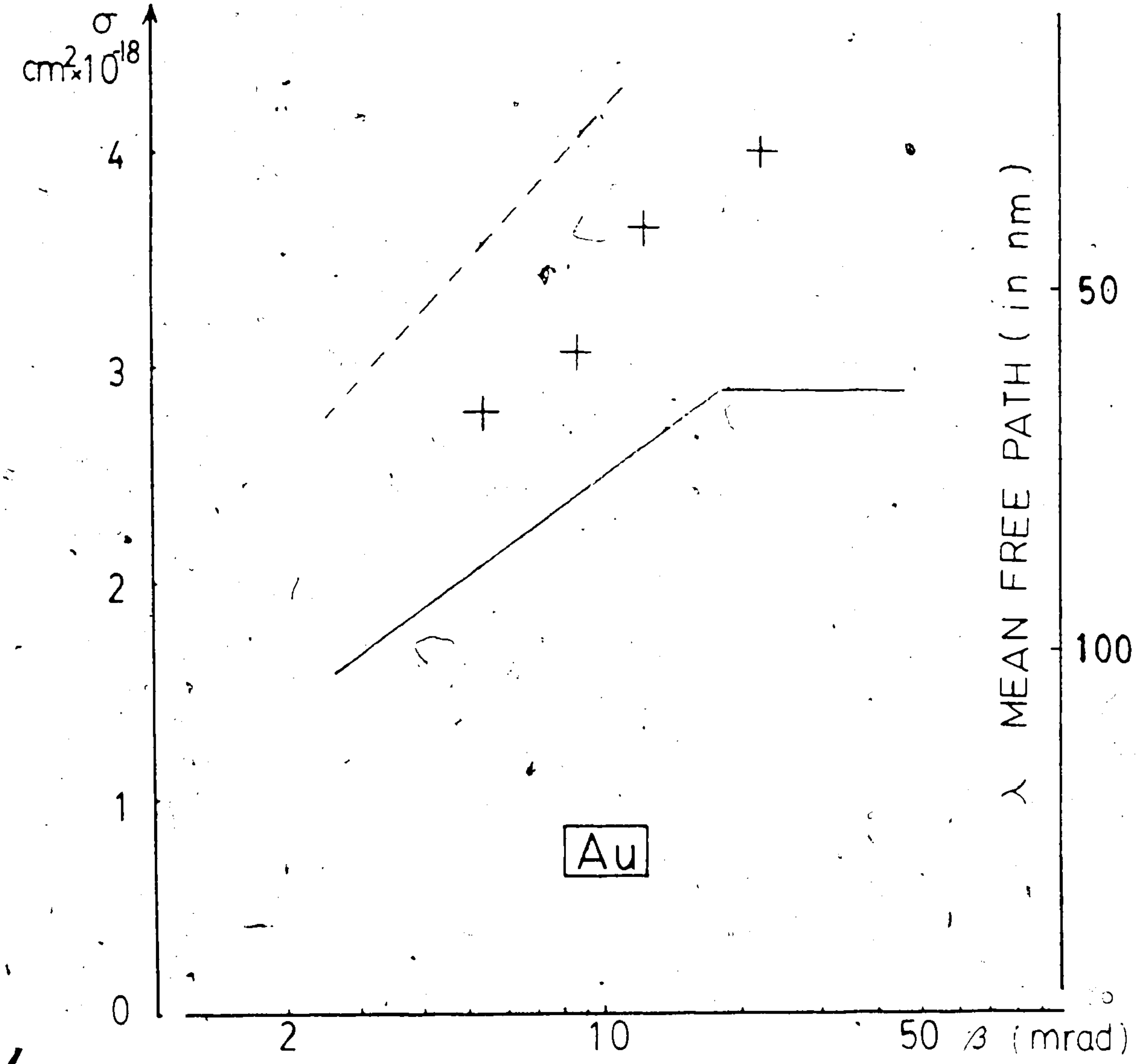

(Fig. 4.2 continued)

Fig. 4.2(e)

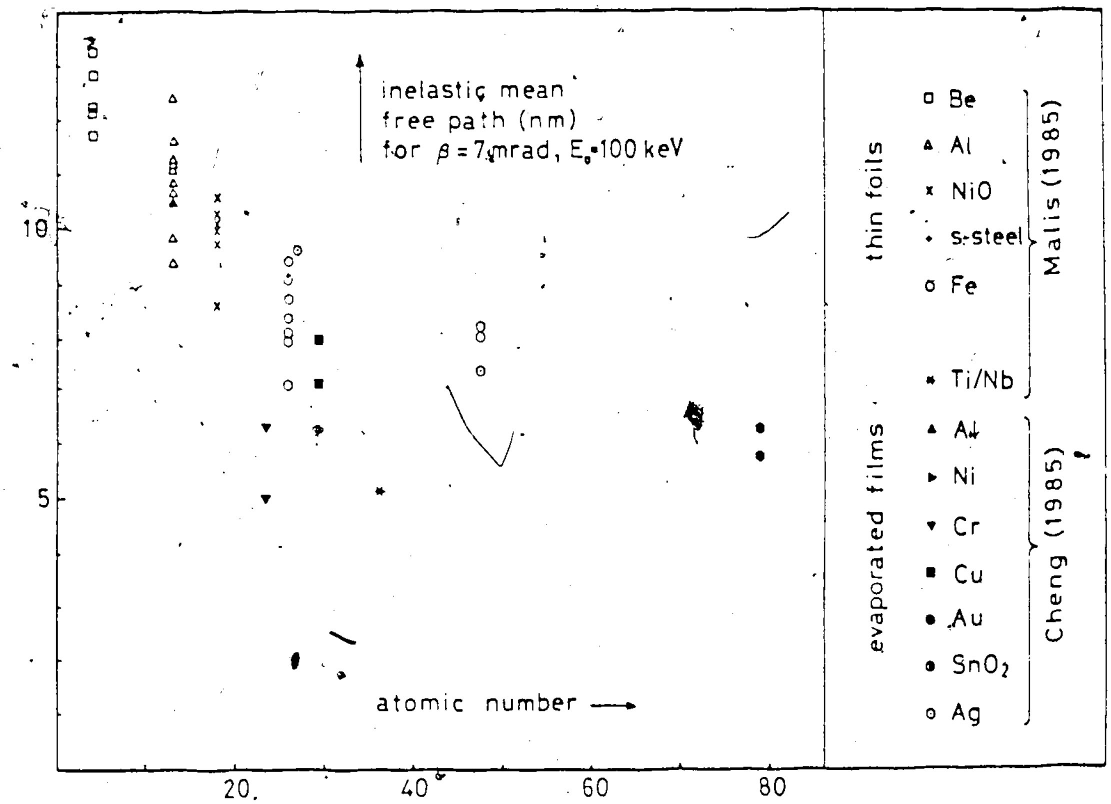

Fig. 4.3. The plot of the mean free path vs. the mean atomic number.

see Eq. (4.27)], can be derived as (Egerton et al. [illegible]7, Malis et al. 1987):

$$\lambda = \frac{106\,F\,E_o}{E_m \log_e(2\beta E_o/E_m)} \qquad (4.36)$$

where λ is expressed in nm, E_o in keV; $E_m = 7.6\,\bar{Z}^{0.36}$ and $F = (1+E_o/1022)(1+E_o/511)^{-2}$ is a relativistic factor (Egerton 1986). For a compound, the mean atomic number is taken as:

$$\bar{Z} = \sum_i \left[\frac{Z_i f_i}{\lambda_i}\right] \Big/ \sum_i \left[\frac{f_i}{\lambda_i}\right]$$

where Z_i, f_i and λ_i are atomic number, atomic fraction and mean free path for each constituent element.

Equation (4.36) has been tested for 20 keV $<E_o<$ 120 keV and 2 mrad $<\beta<$ 20 mrad, and found to be a reasonable approximation within an accuracy of ±20%; see Fig. 4.4. However, where the convergence semi-angle of the incident electrons exceeds β (as may happen for incident probes less than 100 nm in diameter), the former angle should be used in place of the latter (β) in Eq. (4.36) (Malis et al. 1987).

A knowledge of the mean free path, even if only to an accuracy of ±20%, can be useful for estimating the effects of inelastic scattering of electrons in a solid. It also enables the local thickness t of an electron-microscope specimen to be rapidly determined using the log-ratio method

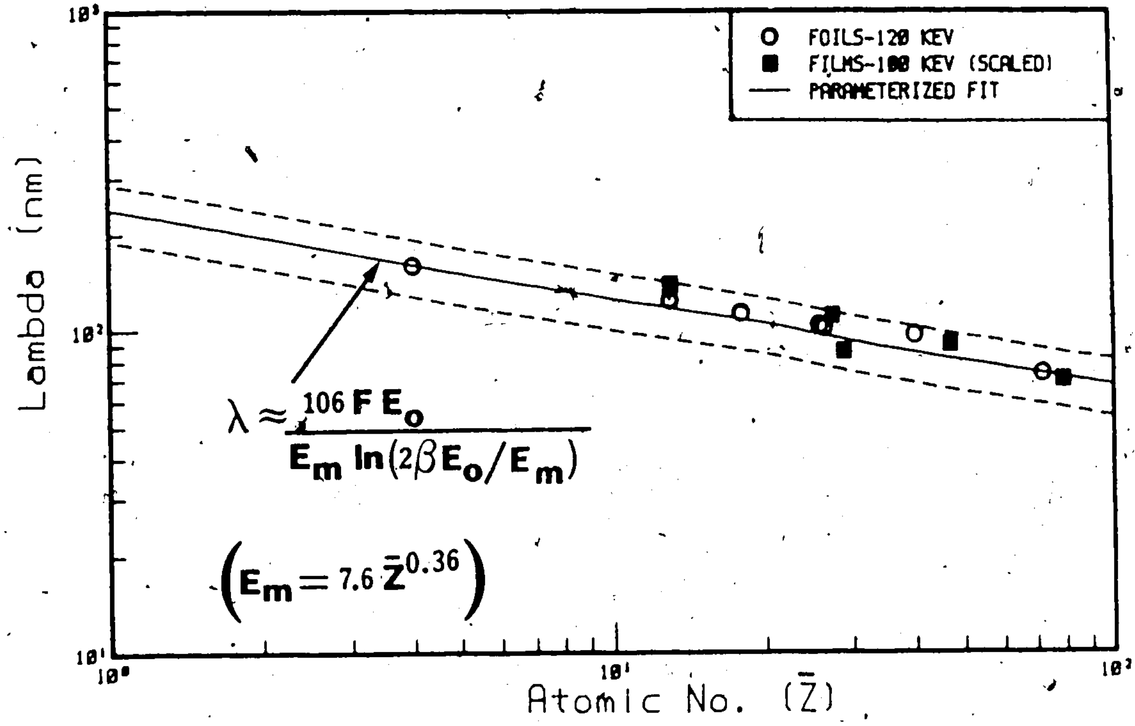

Fig. 4.4. Logarithmic plot of the mean free path vs. the mean atomic number. The solid curve represents Eq. (4.36); dashed curves reprpesent +20% and -20% deviation from this general trend.

[Eq.(4.3)], provided the microscope is equipped with an energy-loss spectrometer and the approximate mean atomic number of the specimen is known.

CHAPTER 5

MEASUREMENT OF LOCAL THICKNESS USING KRAMERS-KRONIG SUM RULE IN ELECTRON ENERGY-LOSS SPECTROSCOPY

5.1 INTRODUCTION

There are a number of situations in which it is necessary to know the local thickness of a TEM specimen; for example, when converting the areal densities provided by EDX or EELS microanalysis into elemental concentrations, when applying fluorescence corrections to the EDX signal, and when estimating defect concentrations from a TEM image. The thickness is also required when using the TEM to measure structure factors, cross sections or mean free paths for elastic or inelastic scattering (Egerton and Cheng 1987).

Several methods of thickness determination are available, each with its own strengths and weaknesses. A procedure based on convergent-beam diffraction is generally thought to be the most accurate, but is applicable only to crystalline regions of a specimen and is time-consuming, since it involves photographic recording followed by graphical analysis (Kelly et al. 1975, Castro-Fernandez et al. 1985).

Another technique involves tilting the specimen and measuring the lateral shift of gold particles or contamination spots introduced onto the top and bottom surfaces (Berriman et al. 1984). Unlike the convergent-beam method, the total thickness is measured, including any amorphous (e.g. oxide) layers present at each surface. However, the accuracy of contamination-spot measurements is perhaps no better than 50 nm (Rae et al. 1981) and the surface decoration and contamination spots may interfere with subsequent TEM imaging of the same specimen. Another destructive technique relies on TEM observation of a transverse section, cut at a known angle relative to the layer whose thickness is to be determined (Berriman et al. 1984).

If the microscope is fitted with an EDX detector, local thickness can be deduced from the background intensity (bremsstrahlung continuum) in the X-ray emission spectrum (Hall and Gupta 1983). Applied to organic specimens, this method is capable of giving mass-thickness to an accuracy of around ±20% (Leapman et al. 1984) if instrumental contributions to the background are sufficiently low. Because the measurement involves a substantial electron dose to the specimen, mass loss can be a problem (Hall and Gupta 1983, Leapman et al. 1984).

The electron energy-loss spectrum in the low-loss region may be used to extract physical information, including the specimen thickness.

The simplest method to estimate the specimen thickness is the log-ratio method. By recording the spectrum up to an energy loss (typically one or two hundred eV) at which the intensity has fallen to a low value, and by measuring the integral I_o under the zero-loss peak and the total integral I_t under the spectrum, the specimen thickness t is measured using Eq. 4.3, i.e.,

$$t = \lambda \log_e(I_t/I_o) \tag{5.1}$$

where λ is the mean free path for all inelastic scattering processes occurring within the recorded energy range (Egerton and Cheng 1985). This equation can be derived by considering the Poisson statistics of plural scattering as given in Chapter 4. The main limitation of the log-ratio method is that it provides an absolute measurement of thickness only if the mean free path is known.

For elastic scattering up to an angle β, the method based on the Bethe sum rule gives the mass-thickness of the specimen as (Crozier and Egerton 1986):

$$\rho t = \frac{B\, m_n T}{4\pi a_o^2 R^2 I_o} \int_0^\infty \frac{E\, S(E)}{\log_e(1 + \beta^2/\theta_E^2)}\, dE \tag{5.2}$$

where ρ is the density of the specimen; t is the thickness of the specimen; B = A/Z for an element (A being the atomic weight and Z the atomic number of the specimen) and $B = M/(\Sigma n_i Z_i)$ for a compound of molecular weight M, n_i being the number of atoms of atomic number Z_i within each molecule; $m_n \doteq 1.67 \times 10^{-27}$ kg being the nucleon mass; $T = m_o v^2/2$ is a relativistically modified incident-beam energy; $a_o \doteq 0.053$ nm is the Bohr radius and R = 13.6 eV the Rydberg energy; $\theta_E = E/(2\gamma T)$ is the characteristic angle for inelastic scattering at an energy loss E, $\gamma = 1/\sqrt{(1-v^2/c^2)}$ being the usual relativistic factor for an electron whose incident velocity is v. In practice, the energy-loss spectrum must be recorded up to an energy loss of at least 1 keV, or with good signal/noise ratio to avoid underestimating ρt because Eq. (5.2) contains the energy loss E as a weighting factor, and hence the integral converges fairly slowly. In addition, derivation of S(E) by means of the Fourier-log deconvolution is exact only for a large collection angle, whereas a fairly small value of β is desirable to ensure that the dipole approximation is obeyed over the entire energy range. The chosen value of β must therefore be a compromise, introducing an amount of error whose magnitude has yet to be determined (Crozier and Egerton 1986).

This chapter presents a third method for determining the absolute thickness of specimen with Kramers-Kronig sum rule in electron energy-loss spectroscopy (Cheng and Egerton 1986). The method requires no knowledge of the physical or chemical properties of the specimen other than the refractive index and involves only a low radiation dose. The accuracy of the method is estimated to be ±10% over the thickness range 10-150 nm. The theory and the implementation of the method, and the experimental results are given below.

5.2 THEORY

The measurement of specimen thickness using the Kramers-Kronig sum rule in EELS is based on the theory of inelastic scattering and the Kramers-Kronig relation. Therefore, the theory of inelastic scattering and the Kramers-Kronig relation will be given briefly in the first two sections. Then the expression for the determination of specimen thickness using the Kramers-Kronig sum rule in EELS will be derived.

5.2.1 INELASTIC SCATTERING OF FAST ELECTRONS IN MATTER

A fast electron, in passing through matter, is inelastically scattered through interaction with outer- and inner-atomic electrons, and thereby losses energy. In a solid, however, several atoms interact simultaneously with the input fast electron. The effect of this on the energy loss of the input electron can be macroscopically regarded as resulting from the dielectric polarization of the medium by the input electron. The latter is generally expressed in terms of a (complex) relative permittivity or dielectric response function: $\epsilon(\omega) = \epsilon_1(\omega) + i\epsilon_2(\omega)$, where $\omega \equiv E/\hbar$ is the angular frequency.

An expression for the electron-scattering power of an infinite medium can be derived using electrodynamics (Ritchie 1957) as follows.

The transmitted electron, having coordinate **r** and moving with a velocity v, is represented as a point charge $-e\delta(\mathbf{r}-\mathrm{v}t)$, t being the time. In the non-relativistic case, the electric field produced by the electron moving through matter can be defined by the scalar potential ϕ which is space and time dependent. This potential satisfies

$$\hat{\epsilon}\Delta\phi = -4\pi e\delta(\mathbf{r}-\mathrm{v}t) \qquad (5.3)$$

in which the dielectric response function ϵ is written as an operator (Landau and Liftshitz 1960).

Expanding ϕ as a Fourier-space integral, i.e.,

$$\phi = \int_{-\infty}^{+\infty} \phi_k \exp(i\mathbf{k}\cdot\mathbf{r})\, d^3k \qquad (5.4)$$

and taking the Laplacian of Eq. (5.4), we have

$$\Delta\phi = -\int_{-\infty}^{+\infty} \phi_k k^2 \exp(i\mathbf{k}\cdot\mathbf{r})\ d^3k \tag{5.5}$$

The Fourier component of $\Delta\phi$ is

$$\Delta\phi_k = -k^2\phi_k$$

Taking the Fourier component of Eq. (5.3) gives

$$\hat{\epsilon}(\Delta\phi)_k = \frac{1}{(2\pi)^3}\int 4\pi e\,\delta(\mathbf{r}-\mathbf{v}t)\exp(-i\mathbf{k}\cdot\mathbf{r})\ d^3r$$

$$= -\frac{e}{2\pi^2}\exp(-it\mathbf{v}\cdot\mathbf{k})$$

Therefore, we have

$$\hat{\epsilon}\phi_k = \frac{e}{2\pi^2 k^2}\exp(-it\mathbf{v}\cdot\mathbf{k})$$

and ϕ_k depends on time t through ~~a~~ factor $\exp(-it\mathbf{v}\cdot\mathbf{k})$. The operator ϵ acting on a function $\exp(-it\mathbf{v}\cdot\mathbf{k})$ multiplies it by $\epsilon(\mathbf{v}\cdot\mathbf{k})$. Hence, we have

$$\phi_k = \frac{e}{2\pi^2 k^2 \epsilon(\mathbf{v}\cdot\mathbf{k})}\exp(-it\mathbf{v}\cdot\mathbf{k})$$

The Fourier components of the field strength $\mathbf{E}_k$, and of the potential ϕ_k are related by:

$$\mathbf{E}_k \exp(i\mathbf{r}\cdot\mathbf{k}) = -\mathrm{grad}[\phi_k \exp(i\mathbf{r}\cdot\mathbf{k})]$$

or

$$\mathbf{E}_k = -i\phi_k \mathbf{k}$$

Thus, we have

$$\mathbf{E}_k = -\frac{ie\mathbf{k}}{2\pi^2 k^2 \epsilon(\mathbf{v}\cdot\mathbf{k})} \exp(-it\mathbf{v}\ \mathbf{k}) \qquad (5.6)$$

The total field strength $\mathbf{E}$ is obtained by inverting the Fourier transform:

$$\mathbf{E} = \int_{-\infty}^{+\infty} \mathbf{E}_k \exp(i\mathbf{r}\cdot\mathbf{k})\, d^3k \qquad (5.7)$$

The force $\mathbf{F} = e\mathbf{E}$; and hence, from Eqs. (5.6) and (5.7) we have

$$\mathbf{F} = -\frac{ie^2}{2\pi^2} \int_{-\infty}^{\infty} \frac{\mathbf{k}}{k^2 \epsilon(\mathbf{v}\cdot\mathbf{k})}\, d^3k$$

Letting the velocity be the x-direction, using $k_x v = \omega$, putting $q = \sqrt{(k_y^2+k_z^2)}$, and replacing $dk_y dk_z$ by $2\pi q dq$, the magnitude of $\mathbf{F}$ can be written as:

$$F = i\,\frac{e^2}{\pi}\int_{-\infty}^{\infty}\int_{0}^{q_o}\frac{q\,\omega}{v^2q^2+\omega^2}\;\frac{1}{\epsilon(\omega)}\,dq\,d\omega \tag{5.8}$$

where q_o is the upper limit of the integration. It is convenient to write

$$\frac{1}{\epsilon(\omega)} = \mathrm{Re}\left[\frac{1}{\epsilon(\omega)}\right] + i\,\mathrm{Im}\left[\frac{1}{\epsilon(\omega)}\right] \tag{5.9}$$

with the real part $\mathrm{Re}[1/\epsilon(\omega)]$ and the imaginary part $\mathrm{Im}[1/\epsilon(\omega)]$ respectively even and odd functions. Thus Eq. (5.8) can be rewritten in the explicitly real form:

$$F = \frac{2e^2}{\pi}\int_{0}^{\infty}\int_{0}^{q_o}\frac{q\,\omega}{v^2q^2+\omega^2}\;\mathrm{Im}\left[\frac{-1}{\epsilon(\omega)}\right]dq\,d\omega \tag{5.10}$$

The energy loss per unit parth length of the transmitted electron, dE/dx, which is also called the stopping power of the substance with respect of the transmitted electron, is the work done by the force over that distance (unit parth length), i.e.,

$$F = \frac{dE}{dx} \tag{5.11}$$

For inelastic scattering, the stopping power is related to the double-differential cross section (per atom) by:

$$\frac{dE}{dx} = \iint n_a E \frac{d^2\sigma}{d\Omega dE} \, d\Omega \, dE \tag{5.12}$$

where n_a represents the number of atoms per unit volume of the medium. By writing $dq \simeq k_0\theta$ and $d\Omega \simeq 2\pi\theta d\theta$, where k_0 is the wave vector of the incident electron and θ the scattering angle, Eqs.(5.10)-(5.12) give:

$$\frac{d^2\sigma}{d\Omega dE} \simeq \frac{\mathrm{Im}(-1/\epsilon)}{\pi^2 a_o m_o v^2 n_a} \frac{1}{\theta^2+\theta_E^2} \tag{5.13}$$

where $\theta_E = E/(\gamma m_o v^2)$ and $\gamma = 1/\sqrt{(1-v^2/c^2)}$ as before.

If the thickness of a film through which a fast electron penetrates is t, the energy loss probability for single scattering, P_1, can be expressed as (Daniels et al. 1970):

$$P_1 = \frac{t}{\pi^2 a_o m_o v^2} \mathrm{Im}\left[\frac{-1}{\epsilon(\omega)}\right] \frac{1}{\theta^2+\theta_E^2}$$

By assuming the dipole approximation, the single-scattering distribution (SSD) within the energy-loss spectrum for inelastic scattering up to an angle β can then be written in the form:

$$S(E) \simeq \frac{tI_o}{\pi a_o m_o v^2} \, \mathrm{Im}\left[\frac{-1}{\epsilon(\omega)}\right] \log_e\left(1+\frac{\beta^2}{\theta_E^2}\right) \qquad (5.14)$$

Therefore, knowing the single-scattering distribution S(E) and the information about the imaginary part of $1/\epsilon(\omega)$, the absolute thickness of the specimen may be determined from Eq. (5.14).

The single-scattering distribution S(E) can be derived from the measured energy-loss intensity J(E) acquired in a multichannel analyser, as described in later sections. The information about the imaginary part of $1/\epsilon(\omega)$ can be found from the Kramers-Kronig relation, which is given in the following section.

5.2.2 KRAMERS-KRONIG RELATION

The Kramers-Kronig relation, derived independently by H.A. Kramers (1927) and R.de L. Kronig (1926), gives the real part of the response of a linear passive system when the imaginary part of the response at all frequencies is known and vice versa.

The Kramers-Kronig relation is usually derived using the Cauchy's theorem to relate the real part and the imaginary part of $\epsilon(\omega)$ on the real axis. To use Cauchy's theorem the following properties of $\epsilon(\omega)$ are required.

(1) The poles of $\epsilon(\omega)$ are all below the real axis.

(2) The integral of $\epsilon(\omega)/\omega$ vanishes when taken around an infinite semicircle in the upper half of the complex ω-plane.

(3) The function $\mathrm{Re}[\epsilon(\omega)]$ is even and $\mathrm{Im}[\epsilon(\omega)]$ is odd with respect to real ω.

The real system that satisfies the above three requirements is called the causal physical system. A complete derivation of the Kramers-Kronig relation using Cauchy's theorem can be found in many text books (Kittel 1976, Jackson 1962), and will not be given here.

A different approach to derive the Kramers-Kronig relation was given by Johnson (1975). He uses a simple time-domain method without recourse to complex analysis. From the time-domain results, a Fourier series method for numerical evaluation of causality relation is derived. Johnson's method eliminates the need to use numerical integration, the use of time-consuming logarithms in evaluating the function, and the need to deal with the Cauchy principal parts in integrating over the pole in the integrand. In addition, through the use of the fast Fourier transform algorithm, the calculation is much more rapid than the conventional integration. Because of the advantages of Johnson's approach mentioned above, and because the Fourier-domain techniques applied in Johnson's approach were used in determining specimen thickness with Kramers-Kronig sum rule, Johnson's approach is given below.

First, consider a real function $\epsilon(t)-\delta(t)$, and let $p(t)$ and $q(t)$ be its even and odd contributions, i.e.,

$$\epsilon(t) - \quad (t) = p(t) + q(t) \tag{5.15}$$

Then, it can be proved that for the causal function $\epsilon(t)-\delta(t)$, the follwing formula is valid (Johnson 1974a):

$$p(t) = \mathrm{sgn}(t)q(t) \tag{5.16}$$

The function of sgn(t) is defined by

$$\mathrm{sgn}(t) = \begin{cases} 1, & t > 0, \\ 0, & t = 0, \\ -1, & t < 0, \end{cases}$$

and can be written as a Fourier transform of $i/\pi\omega$ (Johnson 1974b):

$$\mathrm{sgn}(t) = \frac{i}{\pi} P\int_{-\infty}^{+\infty} \frac{1}{\omega} \exp(-i\omega t)\, d\omega$$

where P represents the Cauchy principal part of the integral. By the convolution theorem and noting that $\epsilon(t)-\delta(t)$, $p(t)$ and $q(t)$ are the inverse Fourier transforms of $\epsilon(\omega)-1$, $\epsilon_1(\omega)-1$ and $\epsilon_2(\omega)$ respectively, the familiar Kramers-Kronig relation is obtained:

$$\epsilon_1(\omega) - 1 = \frac{1}{\pi} P \int_{-\infty}^{+\infty} \frac{\epsilon_2(\omega')}{\omega' - \omega} d\omega' \qquad (5.17)$$

Since the function $1/\epsilon(\omega)$ is also a response of the solid to an 'input' function (the high-energy incident electron), $1/\epsilon(\omega)$ is also a causal function, like $\epsilon(\omega)$. Therefore, the Kramers-Kronig relation [Eq. (5.17)] can be written in the following form:

$$\mathrm{Re}\left[\frac{1}{\epsilon(\omega)}\right] - 1 = \frac{1}{\pi} P \int_{-\infty}^{+\infty} \frac{1}{\omega' - \omega} \mathrm{Im}\left[\frac{1}{\epsilon(\omega)}\right] d\omega' \qquad (5.18)$$

The importance of the Johnson's approach is that it not only gives a different method to derive the Kramers-Kronig relation, but also gives the relation between the Fourier transform of $\epsilon_1(\omega)-1$ and $\epsilon_2(\omega)$ through Eq. (5.16). If $\epsilon_1(\omega)-1$ and $\epsilon_2(\omega)$ are represented by Fourier exponential series in the range $(-\omega_1, \omega_1)$ i.e.,

$$\epsilon_1(\omega) - 1 = \sum_{k=-\infty}^{+\infty} p_k \exp(\frac{ik\pi\omega}{\omega_1}) \qquad (5.19a)$$

$$\epsilon_2(\omega) = \sum_{k=-\infty}^{+\infty} -i\, q_k \exp(\frac{ik\pi\omega}{\omega_1}) \qquad (5.19b)$$

then, by using Eq. (5.16) we have

$$\epsilon_1(\omega) - 1 = 2 \sum_{k=1}^{+\infty} p_k \cos\left(\frac{k\pi\omega}{\omega_1}\right) \tag{5.20a}$$

$$\epsilon_2(\omega) = 2 \sum_{k=1}^{+\infty} p_k \sin\left(\frac{k\pi\omega}{\omega_1}\right) \tag{5.20b}$$

Equations (5.20a) and (5.20b) show that by finding values of p_k which satisfy Eq. (5.20b) and then substituting these values into Eq. (5.20a), the function $\epsilon_1(\omega)-1$ may be found from the function $\epsilon_2(\omega)$. Again, since the function $1/\epsilon(\omega)$ is causal, the following equations, similar to Eqs.(5.20a) and (5.20b), are obtained:

$$\mathrm{Re}\left[\frac{1}{\epsilon(\omega)}\right] - 1 = 2 \sum_{k=1}^{+\infty} p_k \cos\left(\frac{k\pi\omega}{\omega_1}\right) \tag{5.21a}$$

$$\mathrm{Im}\left[\frac{1}{\epsilon(\omega)}\right] = 2 \sum_{k=1}^{+\infty} p_k \sin\left(\frac{k\pi\omega}{\omega_1}\right) \tag{5.21b}$$

Equations (5.21a) and (5.21b) are used in the thickness measurement with the Kramers-Kronig sum rule as will be seen in the later sections.

5.2.3 EXPRESSION FOR THE SPECIMEN THICKNESS USING THE KRAMERS-KRONIG SUM RULE

As a special case of the Kramers-Kronig relation at $\omega = 0$, Eq. (5.18) takes the form:

$$1 - \mathrm{Re}\left[\frac{1}{\epsilon(0)}\right] = \frac{1}{\pi} P \int_{-\infty}^{+\infty} \frac{1}{\omega} \mathrm{Im}\left[\frac{-1}{\epsilon(\omega)}\right] d\omega \qquad (5.22)$$

which has been called the Kramers-Kronig sum rule (Egerton and Cheng 1987).

In principle, at $\omega = 0$ (i.e , $E = 0$) $\mathrm{Re}[1/\epsilon(\omega)]$ in Eq. (5.22) denotes the value of

$$\mathrm{Re}\left[\frac{1}{\epsilon(0)}\right] = \frac{\epsilon_1(0)}{\epsilon_1^2(0) + \epsilon_2^2(0)}$$

For a loss-free dielectric ($\epsilon_2 << \epsilon_1$), this expression reduces to $[\epsilon_1(0)]^{-1}$, $\epsilon_1(0)$ being the static dielectric constant (relative permittivity) of the specimen. In practice, the optical value of $1/\epsilon_1$ (i.e. the value relating to a photon energy between 2 eV and 3 eV) is more appropriate (Keil 1968, Daniels et al. 1970), since the instrumental energy resolution is typically 2 eV, in which case an integration over energy loss takes no account of vibrational-mode losses which lie within the meV region. In other words, $\mathrm{Re}[1/\epsilon(0)]$ in Eq. (5.22) can be replaced by n^{-2} for an insulator or semiconductor, n being the refractive index. For a good conductor such as a metal, ϵ_1 and ϵ_2 are large for E<3 eV, so both $\mathrm{Re}[1/\epsilon(0)]$ and n^{-2} can be taken as zero.

Using Eqs.(5.14), (5.22) and replacing $\mathrm{Re}[1/\epsilon(0)]$ in the left-hand side of Eq. (5.22) by n^{-2}, we obtain the following expression for specimen thickness:

$$t = \frac{4a_0T}{I_0(1-n^{-2})} \int_0^{\infty} \frac{S(E)}{E\ \log_e(1+\beta^2/\theta_E^2)}\, dE \qquad (5.23)$$

Equation (5.23) has the advantage that the 1/E factor, combined with the rapid decrease in S(E) with increasing energy loss, ensures that the integral converges rapidly, so that the single-scattering distribution need be known only up to about 100 eV (see later, Fig. 5.9). However, this same weighting factor gives prominence to low energy losses (<10 eV); to obtain an accurate value of t, it is therefore desirable to achieve good energy resolution and take account of surface-mode energy losses, as discussed below.

5.3 IMPLEMENTATION OF THE KRAMERS-KRONIG SUM RULE

As a first step towards the use of Eq. (5.23), a single-scattering distribution S(E) must be derived from the measured energy-loss intensity distribution J(E) acquired in a multichannel analyser. For this purpose, Fourier-log deconvolution (Johnson and Spence 1974, Spence 1979) has been used. Then, the experimentally-derived single-scattering distribution S(E) has to be corrected for surface-mode scattering. This scattering arises from the fact that, in addition to undergoing inelastic scattering within the specimen, a transmitted electron can lose energy as it crosses the entrance and exit surfaces. Details of the methods of deconvolution, of the correction for surface-mode scattering, and of the fast Fourier transform applied in the Fourier-log deconvolution and in the correction for the surface-mode scattering are given below.

5.3.1 DECONVOLUTION METHOD

In the Fourier-log deconvolution a delta-function approximation is used. The delta-function approximation is equivalent to ignoring instrumental energy broadening and is reasonably accurate when inelastic peaks in the measured spectrum acquired in a multichannel analyser are considerably broader than the zero-loss peak (Swyt and Leapman 1984, Egerton 1986).

Assuming independent scattering events, the intensity I_n, integrated over the energy loss spectrum and corresponding to scattering of order n, follows the Poisson distribution:

$$I_n = I\,P_n = \frac{I}{n!}\left(\frac{t}{\lambda}\right)^n \exp\left(\frac{-t}{\lambda}\right) \qquad (5.24)$$

where I is the incident beam current; P_n is the probability of n scattering events within a specimen with thickness t; and λ is the mean free path for the inelastic scattering as before.

The case n = 0 corresponds to the absence of the inelastic scattering and is represented in the energy-loss spectrum by the intensity distribution over the zero-loss peak Z(E):

$$Z(E) = I_o\delta(E)$$

where I_o is the integrated intensity over the zero-peak as before. From Eq. (5.24) we have

$$I_o = I\exp\left(\frac{-t}{\lambda}\right)$$

The case n = 1 corresponds to the single scattering and is characterized by an intensity distribution S(E). From Eq. (5.24) the single-scattering intensity I_1 is:

$$I_1 = \int S(E)\, dE = I\, (\frac{t}{\lambda})\, \exp(\frac{-t}{\lambda}) = I_o(\frac{t}{\lambda})$$

The case n = 2 corresponds to the double scattering and has an energy dependence of the form S(E)*S(E), where * denotes a convolution over the energy loss. The double-scattering component would therefore be:

$$D(E) = \frac{S(E)*S(E)}{2!\ I_o}$$

Likewise, the n order-scattering contribution is equal to:

$$N(E) = \frac{\overbrace{S(E)*S(E)*\cdots *S(E)}^{n}}{n!\ I_o^{n-1}}$$

The observed energy-loss intensity distribution J(E), including the zero-loss intensity distribution, can therefore be written in the following form:

$$J(E) = Z(E) + S(E) + D(E) + \cdots + N(E) + \cdots$$

$$= I_o\left[\delta(E) + \frac{S(E)}{I_o} + \frac{S(E)*S(E)}{2!\ I_0^2} + \cdots\right] \qquad (5.25)$$

Taking the Fourier transform of both sides of Eq. (5.25) and using the convolution formula, the following equation is obtained:

$$J(\nu) = I_o \left[1 + \frac{S(\nu)}{I_o} + \cdots + \frac{S^n(\nu)}{n!\, I_o^n} + \cdots \right]$$

$$= I_o \exp\left[\frac{S(\nu)}{I_o}\right] \qquad (5.26)$$

By taking the logarithm of both sides of Eq.5.26, we have

$$S(\nu) = I_o \log_e \left[\frac{J(\nu)}{I_o} \right] \qquad (5.27)$$

In Eq. (5.27) $S(\nu)$ and $J(\nu)$ are the complex numbers of the forms S_1+iS_2 and J_1+iJ_2, respectively. Therefore, by comparing the real and the imaginary part in Eq. (5.27), we have:

$$S_1(\nu) = 0.5\, I_o \log_e[J_1^2(\nu) + J_2^2(\nu)] - I_o \log_e I_o \qquad (5.28a)$$

and

$$S_2(\nu) = \psi\, I_o \qquad (5.28b)$$

where

$$\psi = \mathrm{arctg}\left[\frac{J_2(\nu)}{J_1(\nu)}\right] \qquad (5{:}28c)$$

Equations (5.27) and (5.28) gives the simple relationships between the Fourier transforms of the single-scattering intensity distribution and of the measured spectrum. By performing one forward and one inverse transform, all the double- and multiple-scattering distributions can be removed from the measured spectrum.

~~It~~ is noticed that the value of the phase ψ in Eq. (5.28c) is restricted to the range $-\pi/2$ to $\pi/2$ by the arctg function; whereas for a thick sample when the scattering parameter t/λ exceeds $\pi/2$, the true value of the phase ψ may lie outside the above range. In the present work when such a situation occurs, the computer is instructed to correct each discontinuity by adding or substracting multiples of π. The deconvolution then works for samples of arbitrary thickness.

5.3.2 CORRECTION FOR THE SURFACE-MODE SCATTERING

Collective excitations of electrons exist not only in the volume of a plasma but also at its boundary. Longitudinal waves of surface charge density which run along the surface as polarization waves are possible (Ritchie 1957). Therefore, the single-scattering intensity distribution derived from the measured total intensity distribution J(E) should be written as a sum of two terms:

$$S(E) = S_v(E) + S_s(E)$$

where $S_v(E)$ is the contribution due to the inelastic scattering within the specimen and $S_s(E)$ is the contribution due to the transmitted electron crossing the entrance and the exit surface. For applying Eq. (5.23) correctly, $S_v(E)$ instead of S(E) should be used. Thus, after deconvolution S(E) has to be corrected for the surface-mode scattering.

For a clean and smooth surface which is perpendicular to the incident beam, surface-mode scattering is characterized by a differential probability (per unit solid angle and unit range of energy loss) given by (Raether 1980, Egerton 1986):

$$\frac{d^2P_s}{d\Omega dE} = \frac{\hbar}{\pi^2 \gamma a_o m_o^2 v^3} \frac{\theta}{(\theta^2+\theta_E^2)^2} \mathrm{Im}\left[\frac{(1-\epsilon)^2}{\epsilon(1+\epsilon)}\right] \qquad (5.29)$$

In order to apply Eq. (5.29), the following transformation steps are necessary.

First, change the surface-energy-loss function $\mathrm{Im}[(1-\epsilon)^2/\epsilon(1+\epsilon)]$ to:

$$\mathrm{Im}\left[\frac{(1-\epsilon)^2}{\epsilon(1+\epsilon)}\right] = \frac{4\epsilon_2}{(\epsilon_1+1)^2+\epsilon_2^2} + \mathrm{Im}\left(\frac{-1}{\epsilon}\right) \qquad (5.30)$$

Secondly, integrate the angular distribution of the surface energy loss over the scattering angle up to the maximum scattering angle β, which is limited by the objective lens aperture, as below:

$$\int_0^\beta \frac{2\pi\theta^2}{(\theta^2+\theta_E^2)^2}\,d\theta$$

$$= \left.\frac{-2\pi\theta}{\theta^2+\theta_E^2}\right|_0^\beta + \left.\frac{\pi\theta}{\theta^2+\theta_E^2}\right|_0^\beta + \left.\frac{\pi}{\theta_E}\operatorname{arctg}\left(\frac{\theta}{\theta_E}\right)\right|_0^\beta$$

$$= \frac{-\pi\beta}{\beta^2+\theta_E^2} + \frac{\pi}{\theta_E}\operatorname{arctg}\left(\frac{\beta}{\theta_E}\right)$$

Since in practice $\theta_E \ll \beta$, the above formula becomes:

$$\int_0^\beta \frac{2\pi\theta^2}{(\theta^2+\theta_E^2)^2}\,d\theta \simeq \pi\left(\frac{\pi}{2\theta_E} - \frac{1}{\beta}\right) \qquad (5.31)$$

Finally, the following expression for the surface component of the single-scattering distribution is obtained:

$$S_s(E) = 2I_o(dP_s/dE)$$

$$= \frac{1}{\pi a_o k_o T}\left(\frac{\pi}{2\theta_E} - \frac{1}{\beta}\right)\left[\frac{4\epsilon_2}{(\epsilon_1+1)^2+\epsilon_2^2} - \operatorname{Im}\left(\frac{-1}{\epsilon}\right)\right] \qquad (5.32)$$

In Eq. (5.32) $k_o=\gamma m_o v/\hbar$ is the incident-electron wavenumber as before and the factor of two allows for the fact that the specimen has two surfaces.

The procedure for using Eq. (5.32) to correct the surface component of the single-scattering distribution is as follows.

First, on the assumption that S(E) derived from the Fourier-log deconvolution is dominated by the volume-loss component, Eq. (5.23) is used to provide a first estimate of specimen thickness. For this purpose, values of E_o, β and n are required. If the spectral data is acquired with a CTEM operated in image mode (image on the screen), the collection angle is determined by the radius of the objective aperture. A rough estimate of β can be obtained by dividing the aperture radius by the focal length of the objective lens; a more accurate value is achieved by recording the diffraction pattern of a crystalline material, removing the objective aperture during the photographic exposure as described in Chapter 2. Because β occurs within the logarithm term of Eq. (5.23), a 10% error in collection angle gives typically only a 3% or 4% change in the derived value of specimen thickness. As discussed earlier, n^{-2} can be taken as zero for a metal; for semiconductors, n^{-2} is considerably less than unity so the refractive index does not have to be known to high accuracy.

Secondly, also on the assumption that S(E) is dominated by the volume-loss component, Eq. (5.14) and the Kramers-Kronig relation [Eq. (5.18)] can be used to estimate Re[$1/\epsilon(E)$], and thus the real and imaginary parts of the dielectric function $\epsilon(E)$ (Daniels et al. 1970, Isaacson 1972, Wehenkel 1975, Colliex et al. 1976, and Trebbia 1979). This is accomplished using the Fourier-domain technique (Johnson 1974a) described in section 5.2.2 and the fast Fourier transforms described below in section 5.3.3.

Finally, using these values of $\epsilon_1(E)$ and $\epsilon_2(E)$ in [illegible] (5.32), the surface component $S_s(E)$ of the single-scattering distribution can be calculated and subtracted from S(E) to yield the volume-loss contribution. Employing $S_v(E)$ rather than S(E) in Eq. (5.23) leads to a revised estimate of specimen thickness.

Figure 5.1 shows the energy-loss spectrum of single-crystal silicon and polycrystalline evaporated aluminum. The dashed line shows the single-scattering distribution obtained by Fourier-log deconvolution; the peak remaining at 30 eV in aluminum arises from use of the delta-function approximation and from the double-plasmon process (Spence and Spargo 1971, Egerton et al. 1985). The dotted line represents the estimated volume-loss intensity, obtained from the single-scattering distribution by subtracting the surface component given by Eq. (5.32). Note that this subtraction increases the intensity at the volume-plasmon peak, since $S_s(E)$ becomes negative at higher values of E (Raether 1980). Figure 5.1 also shows that the surface-mode scattering tends to involve lower energy loss than corresponding bulk processes. The relative importance

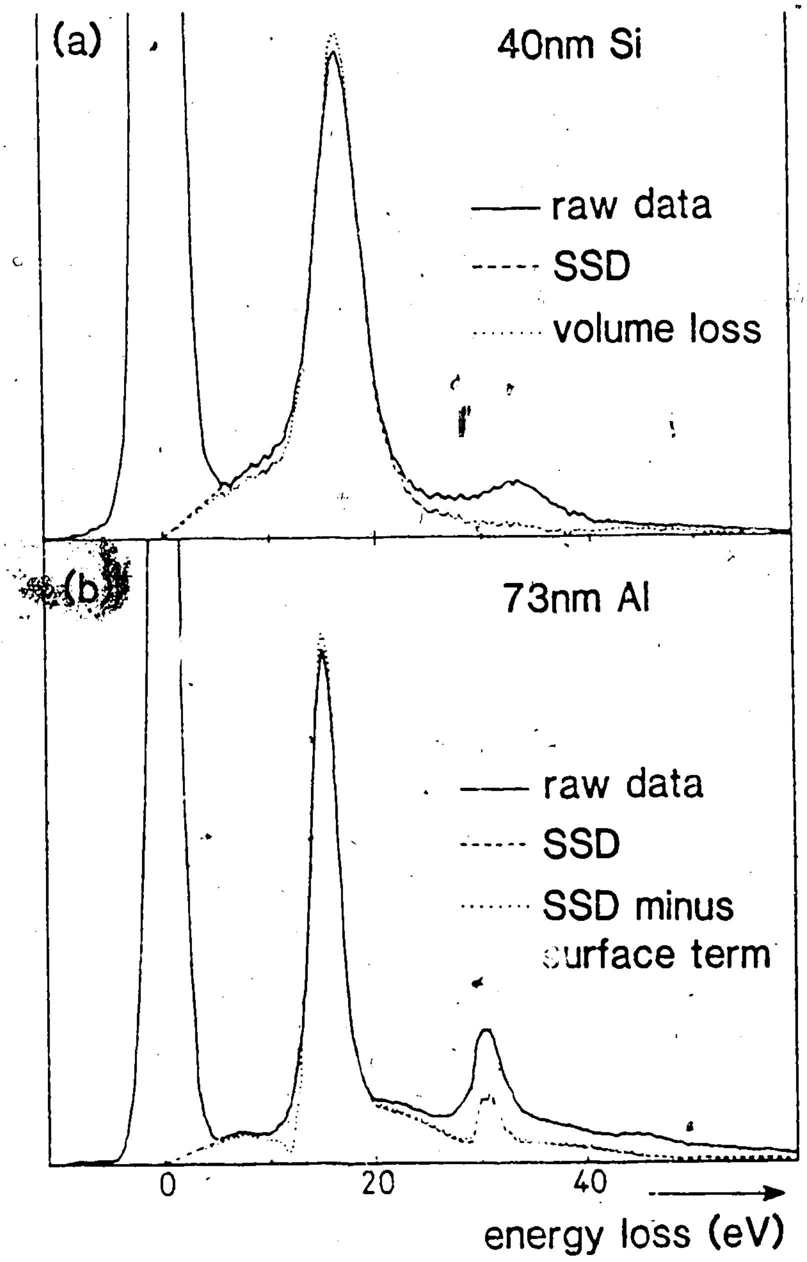

Fig. 5.1. Energy-loss spectra of (a) single-crystal silicon and (b) polycrystalline evaporated aluminum. The dashed line shows the single-scattering distribution obtained by Fourier-log deconvolution; the dotted line represents the estimated volume-loss intensity.

of the surface-scattering intensity distribution $S_s(E)$ is therefore greatest in the 0-10 eV region and in spectra recorded from very thin specimens.

5.3.3 FAST FOURIER TRANSFORM

The technique of fast Fourier transform (FFT) has been adopted in determining specimen thickness by the Kramers-Kronig sum rule, including the deconvolution step and the step for correction of the surface-mode scattering. This technique requires much less computing time than the technique of the normal Fourier tranform. Its concept is given here.

In processing data by digital computer, a continuous Fourier transform is approximated by letting the integrals go over to sums. One works therefore with a discrete set of data. The experimentally measured data is usually available only over a finite range; and thus the Fourier integrals will be of finite range. The spectral analysis of the sampled data over a finite range is referred to as the discrete Fourier transform (DFT) (Higgins 1976). The sampled data set X_k $(0<k<N)$ is represented by a set of Fourier coefficients A_r:

$$A_r = \sum_{k=0}^{N-1} X_k \exp(-i2\pi rk/N) \qquad (5.33)$$

for $r = 0, 1, \cdots, N-1$

Where N is the number of the data points. The discrete Fourier transform (5.33) has N terms in the sum and N coefficients, so that N^2 multiplications are required in computing the DFT.

The fast Fourier transform (FFT), developed by Cooley and Tukey (Cooley and Tukey 1965), does the same operation with only N $\log_2 N$ multiplications. The mathematics of the FFT involves first a splitting of the data set X_k into odd and even labeled points, Y_k and Z_k, then use of the periodicity of the exponential function to eliminate redundant operations.

Let

$$Y_k = X_{2k}$$

$$Z_k = X_{2k-1}$$

$$\text{for } k = 0,\ 1,\ \cdots,N/2-1$$

Then, Eq. (5.33) may be rewritten as:

$$A_r = \sum_{k=0}^{N/2-1} \{Y_k \exp(\frac{-i4\pi rk}{N}) + Z_k \exp[\frac{-i2\pi r(2k+1)}{N}]\} \qquad (5.34)$$

$$\text{for } r = 0,\ 1,\cdots,N-1$$

Bringing a constant phase factor out of the Z_k term, Eq. (5.34) takes the following form:

$$A_r =$$

$$\sum_{k=0}^{N/2-1}\left[Y_k\exp\left(\frac{-i4\pi rk}{N}\right) + \exp\left(\frac{-i2\pi r}{N}\right)\sum_{k=0}^{N/2-1} Z_k\exp\left(\frac{-i4\pi rk}{N}\right)\right] \tag{5.35}$$

This will generate the whole set of A_r if r is allowed to vary over the full range ($0 \le r < N$). Let r vary over half the range ($0 \le r < N/2$). We may write Eq. (5.35) as:

$$A_r = B_r + W^r C_r \tag{5.36}$$

$$\text{for } 0 \le r < N/2$$

where

$$B_r = \sum_{k=0}^{N/2-1} Y_k \exp\left(\frac{-i4\pi rk}{N}\right)$$

$$C_r = \sum_{k=0}^{N/2-1} Z_k \exp\left(\frac{-i4\pi rk}{N}\right)$$

$$W = \exp\left(\frac{-i2\pi}{N}\right)$$

However, since both B_r and C_r are periodic in the half-interval, generating A_r for the second half of the range may be done without further computation using the same B_r and C_r:

$$A_{r+N/2} = B_r - W^r C_r \tag{5.37}$$

$$\text{for } 0 \le r < N/2$$

Therefore, the work of computing an N-point transform A_r has been reduced to computing two N/2-point transforms B_r and C_r and the appropriate multiplicative phase factor W^r. This is already a saving of time since $2(N/2)^2<N^2$. The two N/2-point transforms are not computed yet; each is split further into two N/4-point tranforms. This procedure continues until N one-point transforms are obtained. It takes $\log_2 N$ of these splittings, so that generating the N one-point tranforms takes a total of, approximately, $N \log_2 N$ operations rather than the N^2 operations when the DFT algorithm is used.

Since the fast Fourier tranform (FFT) technique is used in computing the specimen thickness, the entire spectral processing program (200 lines of Fortran; Appendix A) is executed in only 0.2 sec on an Amdahl 4881 computer, or less than 10 sec with a PDP 11/23 minicomputer (Egerton and Cheng 1987).

5.4 EXPERIMENTAL RESULTS

Experimental investigation of Eq. (5.23) as a method of thickness measurement was performed to find out what degree of accuracy is obtainable under typical electron-microscope conditions and what are the best choices of the externally-variable parameters (incident energy, collection angle etc.). The range of material tested covers several metals, semiconductor silicon and semimetal carbon.

5.4.1 METALS

Most of the measurements were made on thin films of the metals Al, Cr, Ni, Cu, Ag and Au evaporated from tungsten or molybdenum wires (or boats) in a standard vacuum system and condensed onto unheated glass substrates. The methods for making the films, for taking the spectra, and for measuring the thickness of the film independently by weighing with a sensitive microbalance are described in Chapter 4.

Results for films of Al, Cr, Ni, Cu, Ag and Au are illustrated in Figs. 5.2(a)-5.2(f), where the straight lines of unit slope represent ideal agreement between the weighted thickness and that determined from the Kramers-Kronig sum rule.

Figure 5.3 shows the dependence of the measured thickness on the collection semi-angle β, which was varied by changing the objective-lens aperture. Open data points are the initial estimates of thickness; filled points are the revised estimates, based on the volume-loss intensity. Horizontal lines show the thickness determined by weighing; vertical lines indicate the scattering angles (for E_o = 100 keV) corresponding to the first two diffraction rings. The dashed curve represents the behaviour expected (for 137 nm Al) if the angular distribution of inelastic

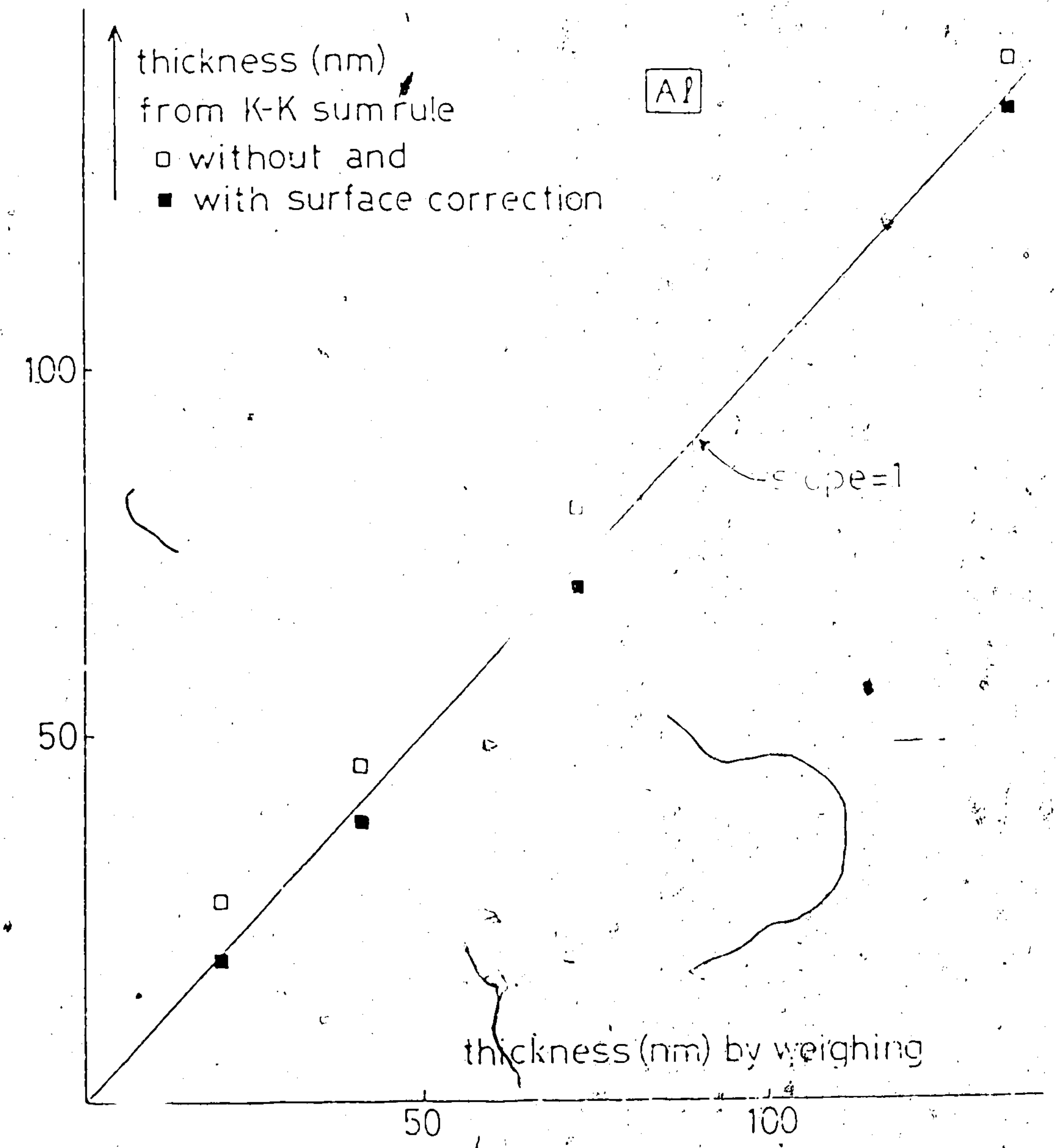

Fig. 5.2. Plots of film thickness determined by the Kramers-Kronig sum rule vs. film thickness determined by weighing for metals: (a) Al, (b) Cr, (c) Ni, (d) Cu, (e) Ag, and (f) Au. The open squares represent the initial estimate of thickness, neglecting surface-mode scattering; the filled squares include a first-order correction for surface scattering, based on Eq.(5.32). E_0 = 100 keV; β = 5.3 mrad.

(to be continued)

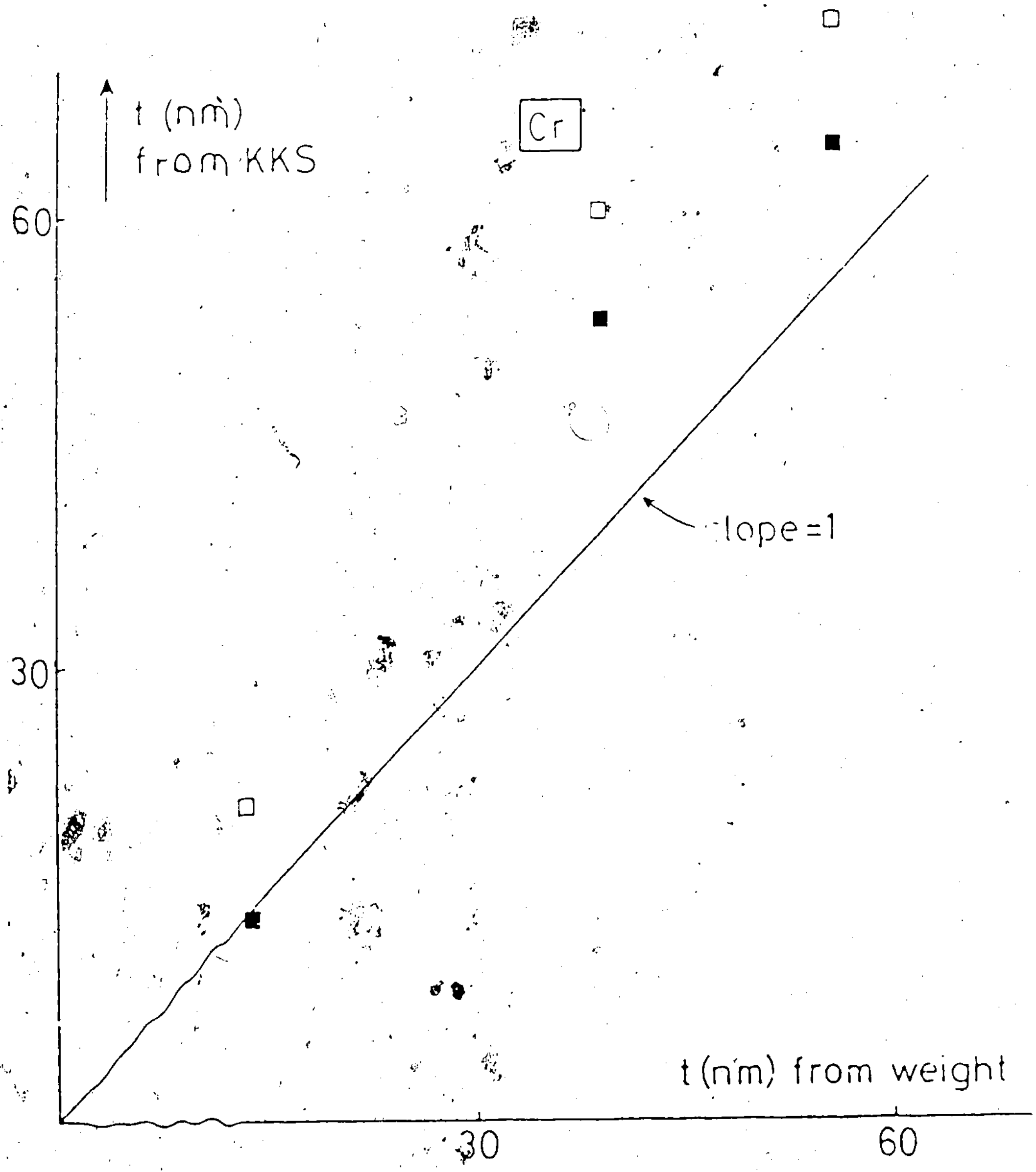

(Fig. 5.2 continued)

Fig. 5.2(b)

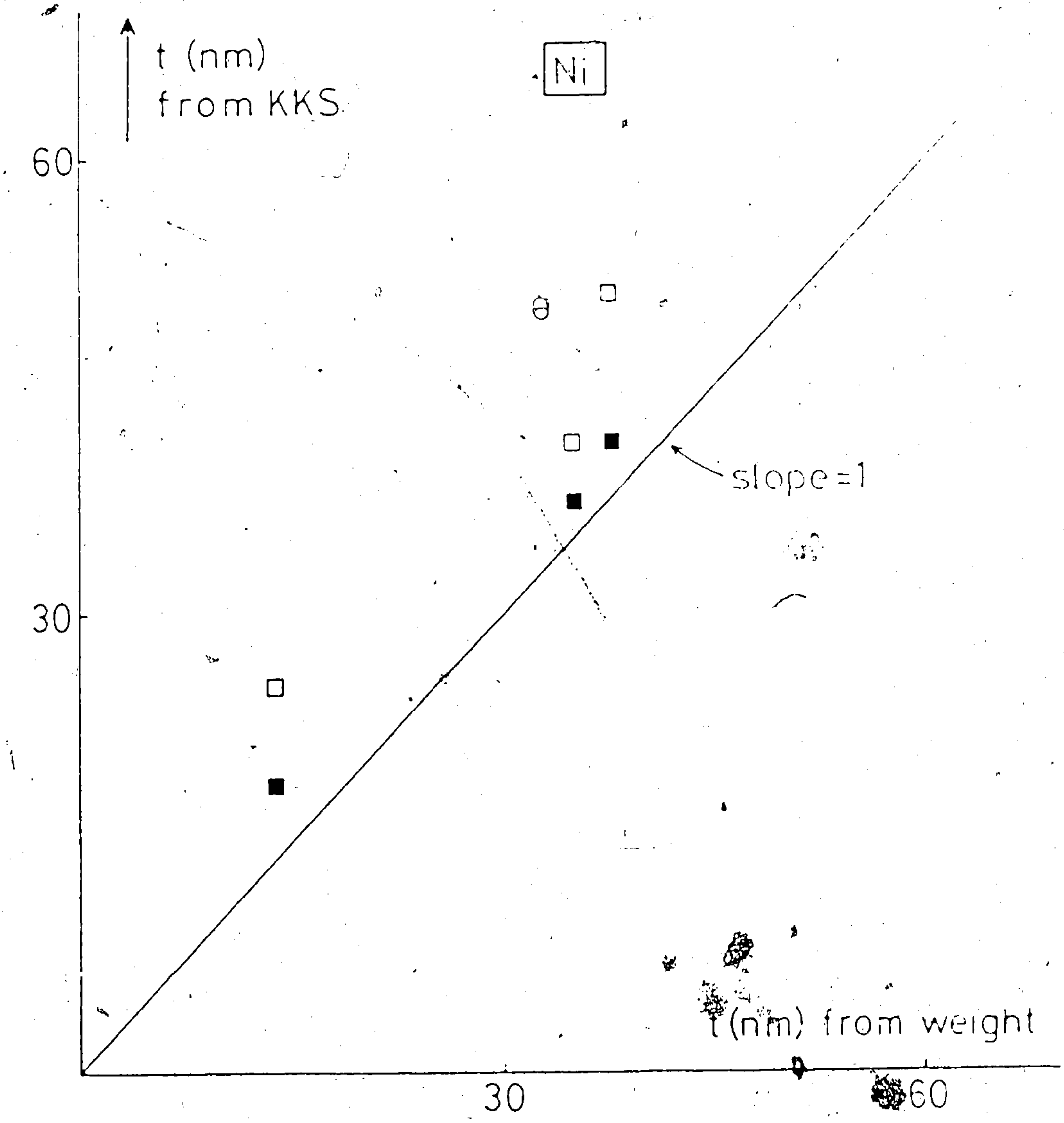

(Fig. 5.2 continued)

Fig. 5.2(c)

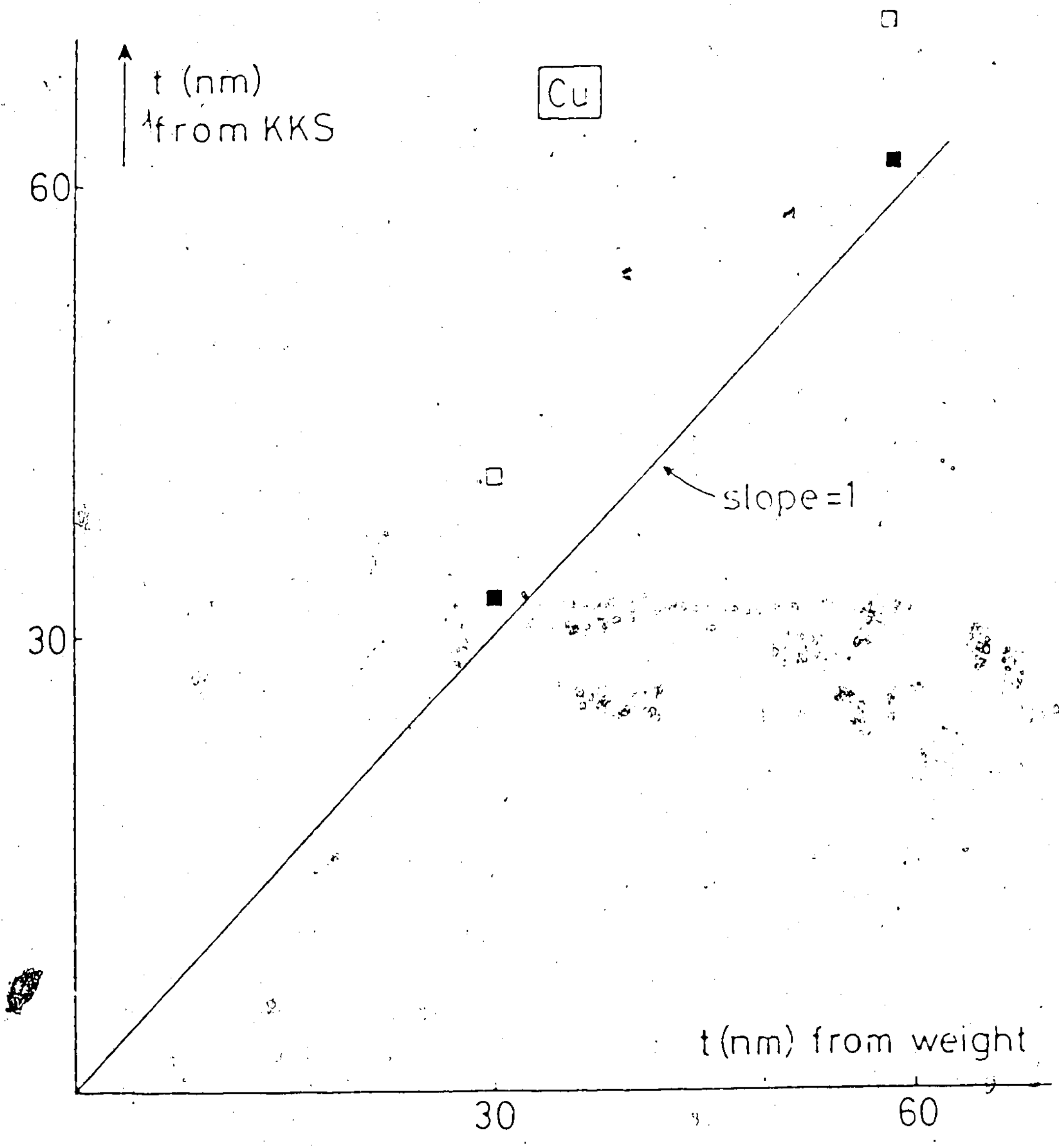

(Fig. 5.2 continued)

Fig. 5.2(d)

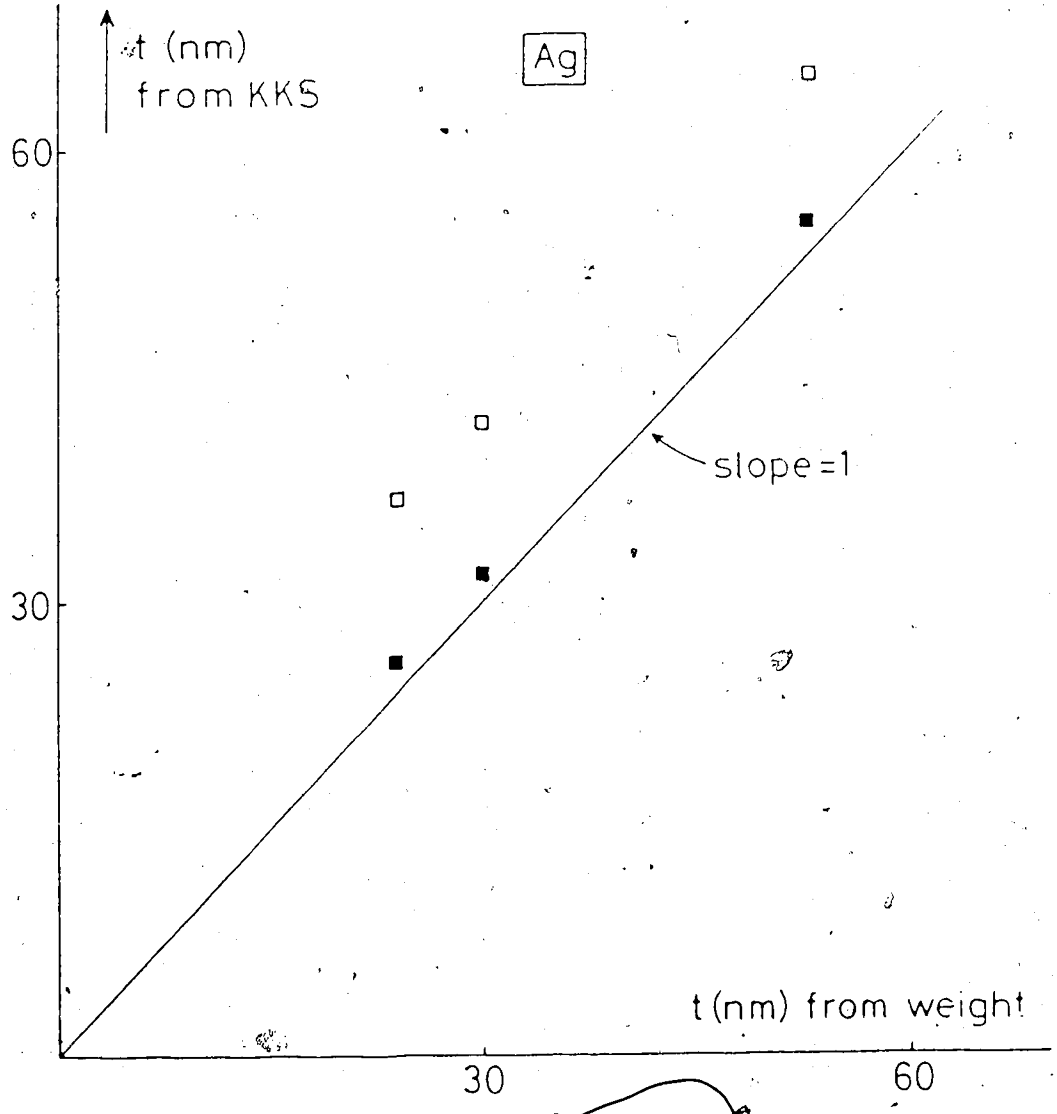

(Fig. 5.2 continued)

Fig. 5.2(e)

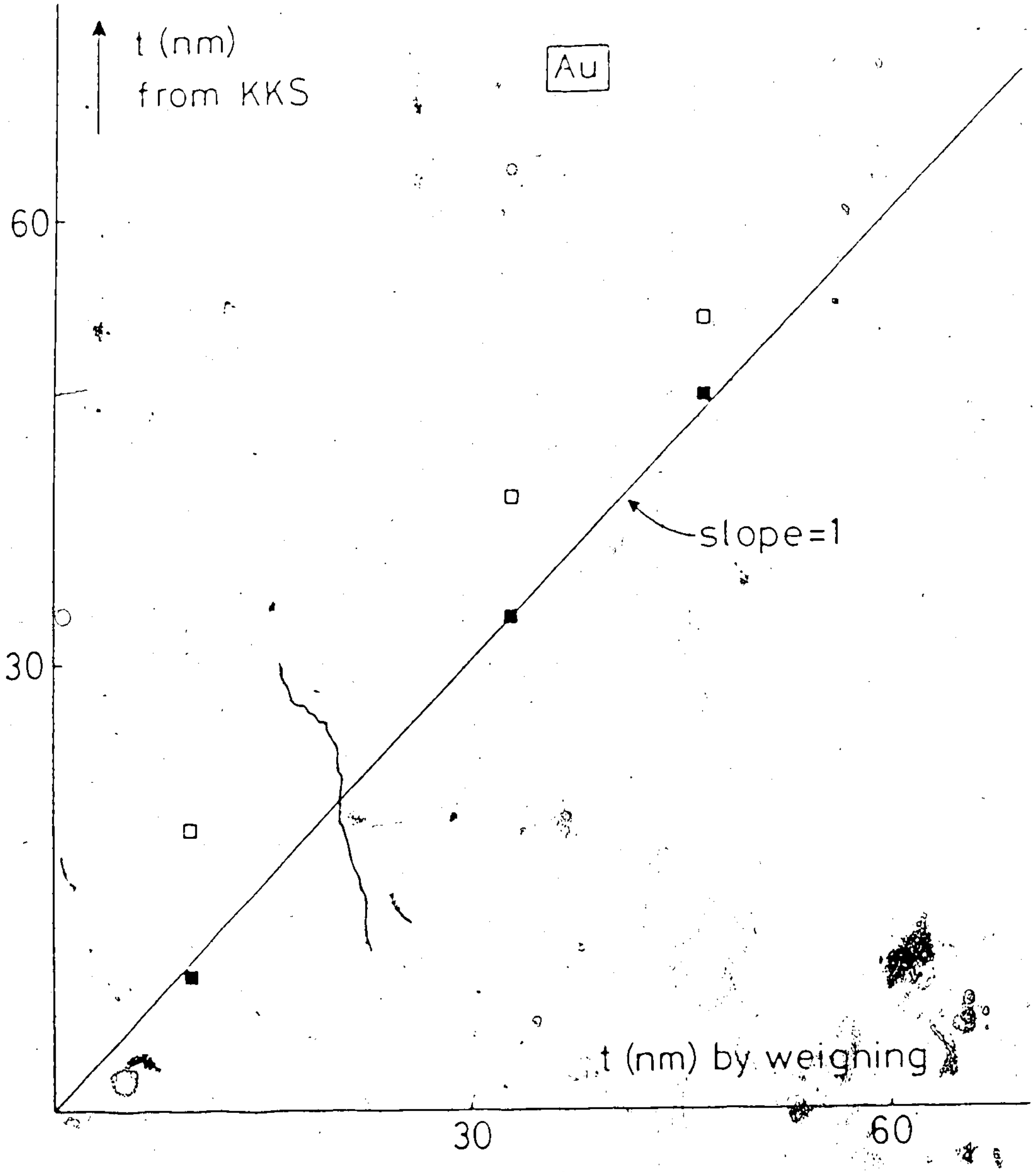

(Fig. 5.2 continued) Fig. 5.2(f)

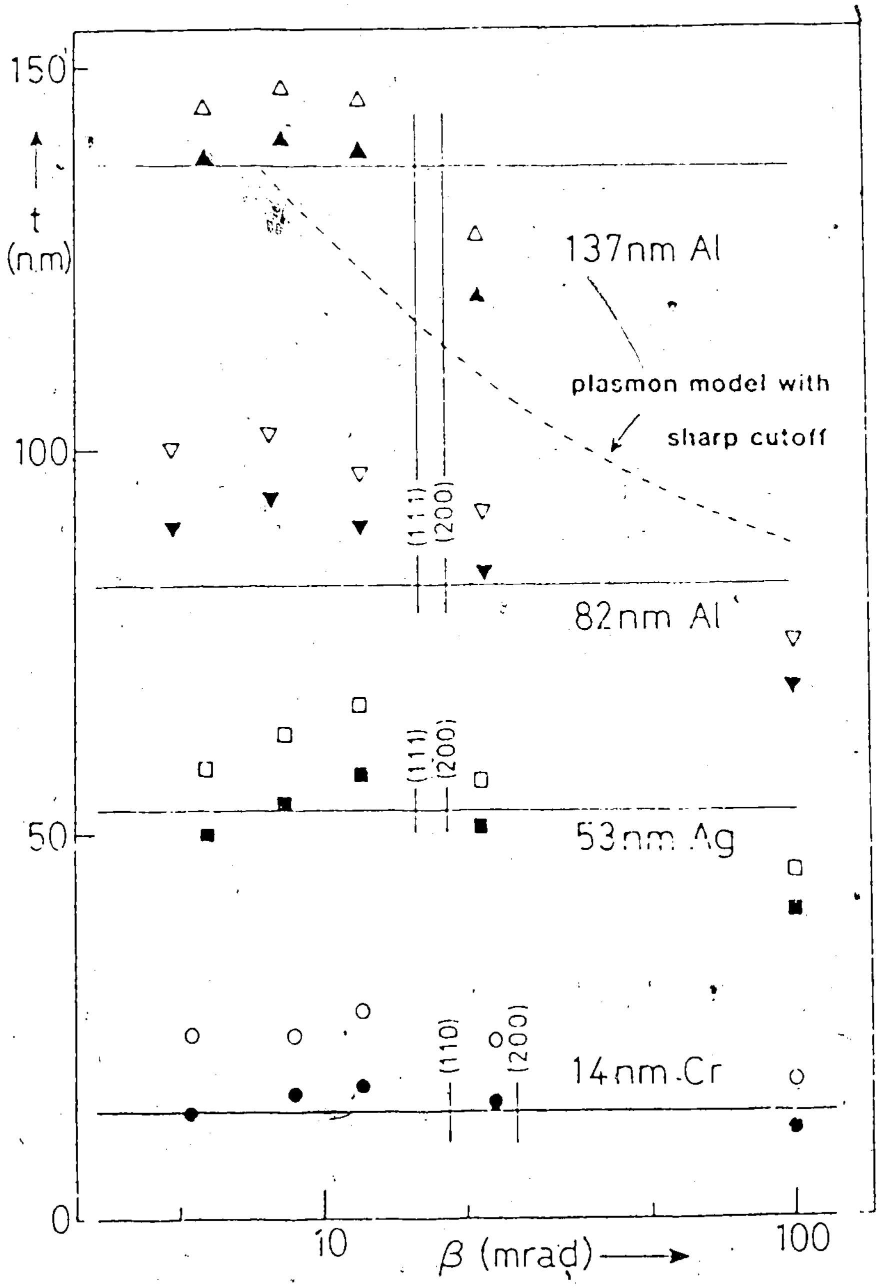

Fig. 5.3. Dependence of measured film thickness on the collection semi-angle β. See the text for details.

scattering had a sharp cutoff at the critical angle for plasmon excitation.

Theoretically, the logarithmic angular dependence in Eqs.(5.14) and (5.23) is correct only if the maximum collecting angle β is smaller than the cutoff angle θ_c (Egerton 1986). Therefore, the value of t should be an underestimate if β is too large. However, Eq. (5.23) ignores the fact that some electrons are scattered elastically as well as inelastically. In the case of a single-crystal or polycrystalline specimen, these electrons will contribute significantly to the inelastic intensity J(E) if strongly diffracted beams lie just outside the collection aperture, leading to an overestimate of t. If β is too small, Fourier-log deconvolution will tend to oversubtract the plural-scattering intensity, probably by about 10% for β = 5 mrad and E_o = 100 keV (Egerton 1986), although the resulting percentage underestimate of t will be only half as large as a result of the 1/E factor in Eq. (5.23).

These predicted trends are visible in Fig. 5.3. As β is increased, the measured thickness first increases slightly and then decreases. If the objective aperture is removed, giving an effective collection angle of the order of 100 mrad, the thickness is underestimated, although not to the extent predicted on the assumption that the oscillator strength drops abruptly to zero at the critical angle for plasmon excitation (about 8 mrad for aluminum). According to these experiments, realistic thickness values are obtained (at 100 keV incident energy) with any aperture semi-angle in the range 5-15 mrad. More generally, β should be comparable with the lowest-order Bragg angle (objective-aperture diameter half that of the innermost diffraction ring), as in core-loss microanalysis.

In all of the measurements, standard CTEM illumination conditions were used, where the effect of the incident-beam convergence can be neglected. In the case of fine probes, the convergence angle α may approach or exceed the collection angle β and a convergence correction should be applied, as in the case of energy-loss elemental analysis. An approximate correction would involve dividing t by the correction factor F_2 calculated for a characteristic angle θ_E appropriate to the mean energy loss (Egerton 1986). A more sophisticated procedure would be to incorporate an analytical formula for the collection efficiency (Scheinfein and Isaacson 1984) into the integral of Eq. (5.23).

Figure 5.4 shows the result of applying the Kramers-Kronig sum rule at different incident-beam energies. In the case of the calibrated aluminum sample, the measured thickness (with surface correction) remains within 10% of the weighed value for accelerating voltages in the range 20 keV to 100 keV. It seems reasonable to expect Eq. (5.23) to apply equally well at higher incident energies, except that above 300 keV retardation effects become appreciable

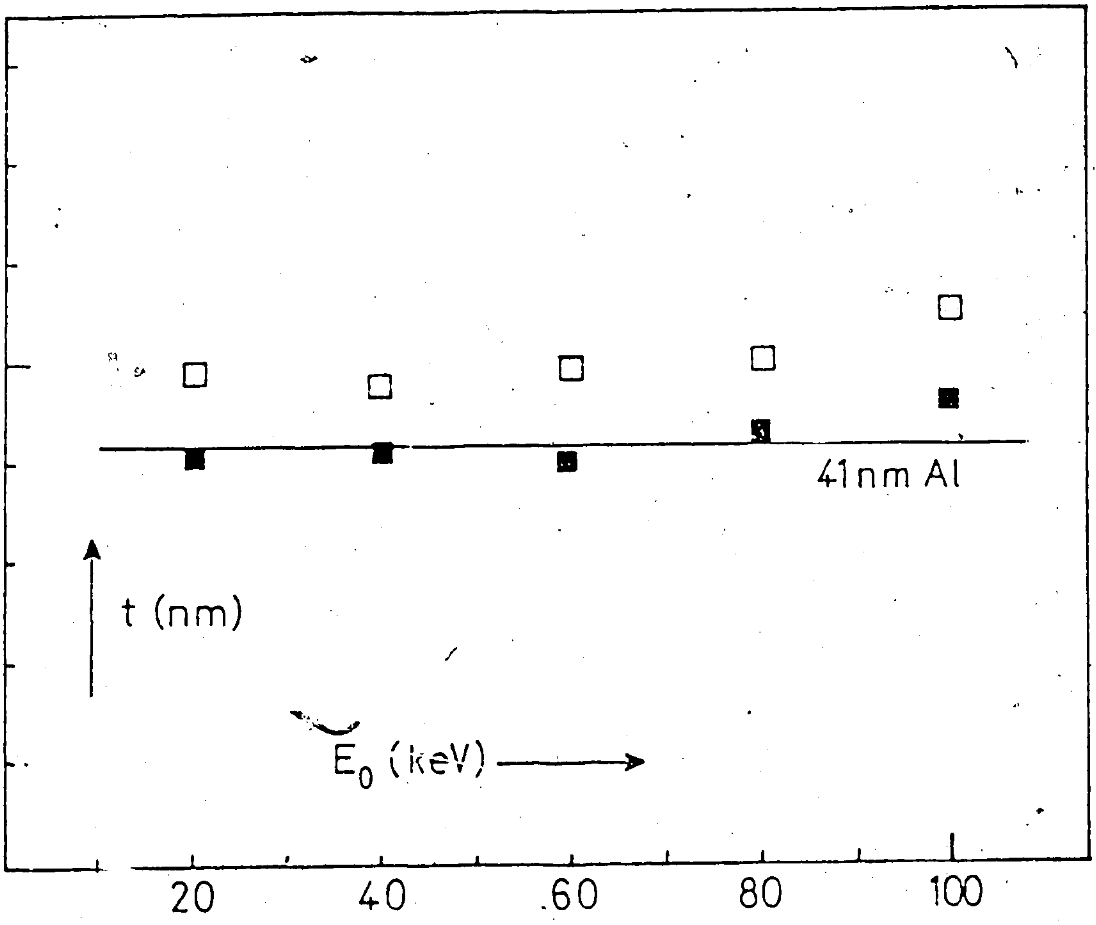

Fig. 5.4. Measured thickness of evaporated aluminum films, plotted as a function of incident-electron energy. The collection semi-angle, β = 4.8 mrad. The filled data points include the surface correction. The horizontal line indicates the weighed thickness of the aluminum film.

throughout the energy-loss spectrum and would modify the angular distribution of inelastic scattering (Egerton 1986).

The measurements on evaporated thin films of six metals are summarized in Table 5.1, where the apparent errors in thickness [the deviation of the experimental points from the lines of unit gradient in Figs. 5.2(a)-5.2(f)] has been divided into random and systematic components. The systematic error is the percentage by which the straight line in Figs. 5.2(a)-5.2(f), passing through the origin and representing a best fit to the experimental points, deviates in slope from unity. The random error represents the mean square deviation of the data points from this line. Random errors are around 6% and probably reflect the influence of statistical noise, instrumental instabilities etc. The systematic errors are all positive, indicating that the thickness obtained from Eq. (5.23) is greater than that measured by weighing.

Two factors might account for this systematic discrepancy. Firstly, after reweighing the glass substrate there could be additional oxidation of the metal film (for example when immersing the substrate in water in order to detatch the film) and this oxygen will increase the amount of inelastic scattering and therefore the value of t. Secondly, the films are polycrystalline and will contain internal 'voids' or regions of reduced density at grain boundaries. If these voids are sufficiently small (e.g. less

Table 5.1. Thickness measurements on evaporated thin films of Al, Cr, Ni, Ag and Au

Material	Melting point (°C)	Radom error (%)	Systematic error (%)
Al	660	±4	+[illegible]
Ag	960	±6	+6
Au	1064	±6	0
Cu	1083	±6	+10
Ni	1455	±7	+13
Cr	1857	±10	+22

than the localization volume associated with inelastic scattering) and uniformly distributed, the films can be considered to have lower physical density than a perfect single crystal. The reduced 'apparent density' of thin films is well known, although the measured reduction factor is highly variable (Blois and Rieser 1954, Wolter 1965, Chopra 1969) and probably depends on the methods of measurement, the grain size and the film thickness.

In support of these arguments, the systematic errors in Table 5.1 tend to increase with the melting point of the metal. High melting point generally implies small grain size, reduced 'density' and increased likelihood of internal oxidation within the film (Chopra 1969). In fact the chromium films (for which the systematic error was largest) were found to contain up to 30% of oxygen, based on analysis of the oxygen K-ionization edge visible at higher energy loss. Moreover, the systematic error is close to zero for the gold films, which were found by TEM observation to have a relatively large grain size (>30 nm) and which should be free of oxide. It is therefore quite possible that the systematic errors shown in Table 5.1 arise mainly from imperfections of the test samples, rather than from errors associated with the Kramers-Kronig method of thickness determination.

5.4.2 SILICON

A futher investigation on the accuracy of the Kramers-Kronig method of the thickness determination was made by comparing the thickness measurements made on specimems of single-crystal silicon, using the thickness fringe method. The thickness fringes appear at the Bragg condition, and the extinction distance can be calculated based on the dynamical theory (Hirsch et al. 1977, Spence 1980, Reimer 1984).

Suitable wedge-shaped single crystals of silicon were prepared using the chemical polishing technique (Cann 1973). First, commercial silicon wafers 0.25 mm in thickness, oriented in the (111) plane, were glued to a brass block. Then, a high speed drill whose inner diameter was slightly larger than 3 mm was used to drill silicon discs from the brass-silicon block with an abrasive paste dabbed between the brass drill and the surface of the silicon wafers. The obtained silicon discs (3 mm in diameter and 0.25 mm in thickness) were then placed directly, by a set of teflon coated tweezers, over an acid jet at a position which was approximately 2 mm above the nozzle of the jet. The composition of the acid was 9 parts of HNO_3 (70%) and 1 part of HF (48%). The acid jet ejected the acid with a speed of approximately 60 drops or 3 ml per minute. The polishing of one side of the silicon disc was allowed to continue until a definite dished shape appeared. The disc was then turned over and other side placed over the jet until perforation was observed. The silicon disc was then placed in a beaker containing the same acid mixture described above for about 10 sec to give a final polish to both sides before being alternately washed in distilled water and ethyl alcohol.

The silicon specimen, prepared as above, was examined in a JEM 100B electron microscope at an accelerating voltage of 100 kV. The orientation of the specimen with respect to the electron beam was varied by using a EM-BLG tilting specimen holder. In this holder, the specimen, mounted on gimbals, can be tilted up to ±30° in any direction by the vertical displacement of two driving shafts, as described in Chapter 2. In this way the specimen was oriented so as to approximately satisfy the Bragg condition for the (220) plane. Spectra were then recorded with the spectrometer entrance aperture located at the centre of successive bright thickness fringes running parallel to the edge of the specimen.

Figure 5.5 shows the diffraction pattern of the silicon sample taken from a relatively uniform wedge-shaped region of the sample. It indicates that the (220) Bragg condition has been nearly satisfied. Figures 5.6(a) and 5.6(b) show the thickness fringes of the single-crystal of silicon obtained in the bright and the dark field at the magnification of about 5×10^5. The energy-loss spectra of the silicon specimens at various thicknesses are shown in

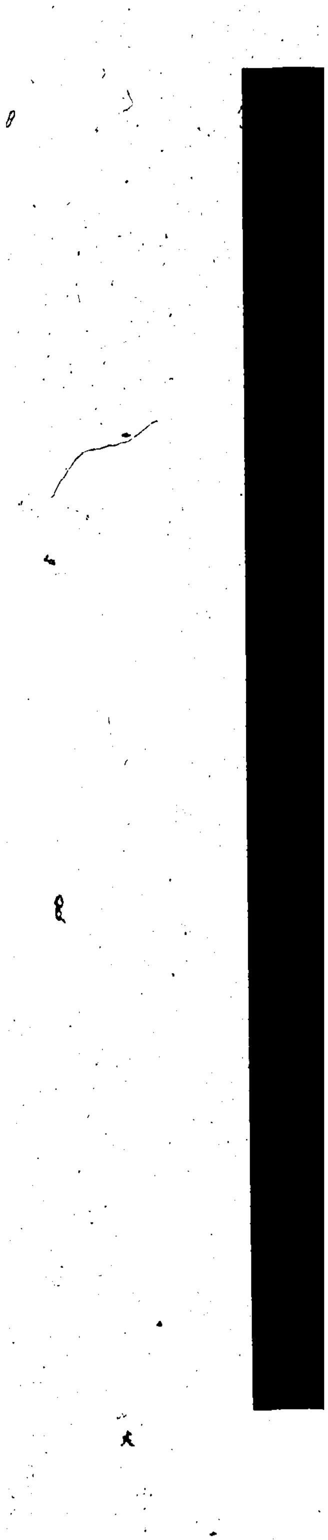

Fig. 5.5

single-cry

terns of the

Bragg condition.

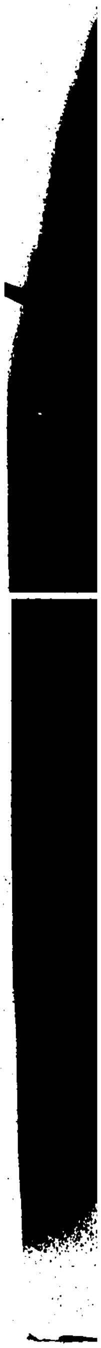

Fig.

obtai

and i

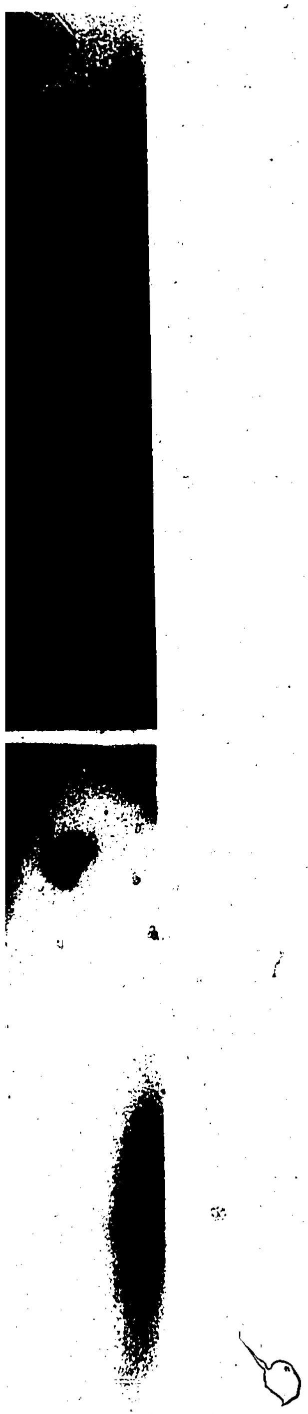

ystal silicon

ght field (a)

Figs. 5.7(a)-5.7(f). Figure 5.8 shows the Kramers-Kronig measurement of local thickness of a silicon specimen, plotted against local thickness given by the pendellösung fringes. The local specimen thickness (horizontal axis on Fig. 5.8) was taken as $(m/2)\xi^{w}_{220}$ where m is an integer (1,3 or 5 for the dark-field and 2, 4 or 6 for the bright-field image); $\xi^{w}_{220} = \xi_{220}/(1+w^2) = 73$ nm is an 'effective' extinction distance, calculated from the extinction distance $\xi_{220} = 77$ nm and the deviation parameter w measured from the electron-diffraction pattern (Hirsch et al. 1977). Using a computer program based on a more complicated model, provided by Dr. Sheinin in Physics Depaprtment, the University of Alberta, the same extinction distance was obtained. In Fig. 5.8 the sum rule appears to overestimate the local thickness at small t, but this discrepancy largely disappears if one assumes that each surface of the specimen was covered by about 5 nm of native oxide (Philipp and Taft 1982). Being amorphous, the oxide would not affect the thickness-fringe measurements but would increase the Kramers-Kronig estimate of thickness.

In applying equation (5.23) to silicon, the optical refractive index has been taken as n = 3.3 (Philipp and Ehrenreich 1963). Since the important factor is $1-n^{-2}$, a 10% error in the value of n would cause only a 2% change in thickness. A similar situation applies to many other semiconductors, n being relatively high. Most insulators (including organic compounds) have refractive indices less

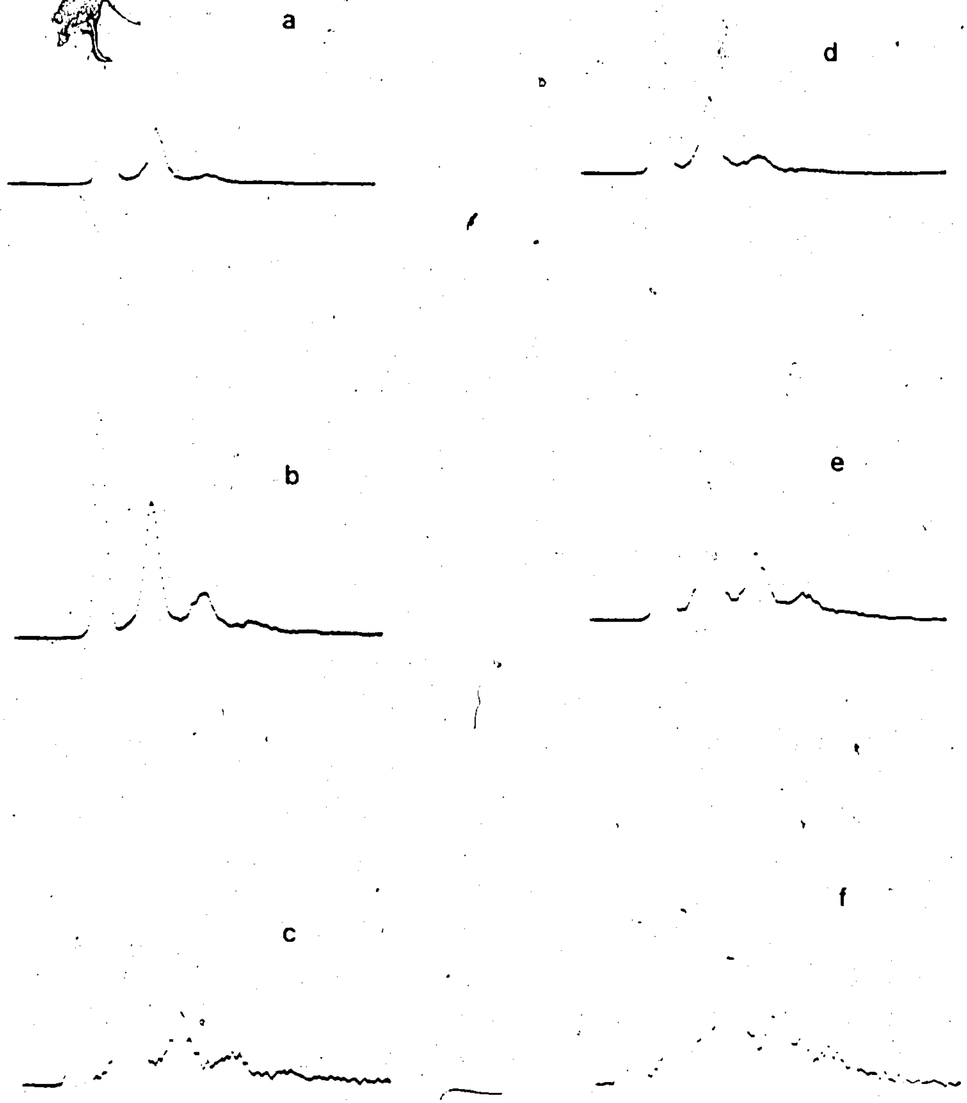

Fig. 5.7. Energy-loss spectrum of silicon specimens at various thickness corresponding to the dark field in Fig. 5.6(b): (a) the first fringe, (b) the second fringe, (c) the third fringe, and to the bright field in Fig. 5.6(a): (d) the first fringe, (e) the second fringe, (f) the third fringe.

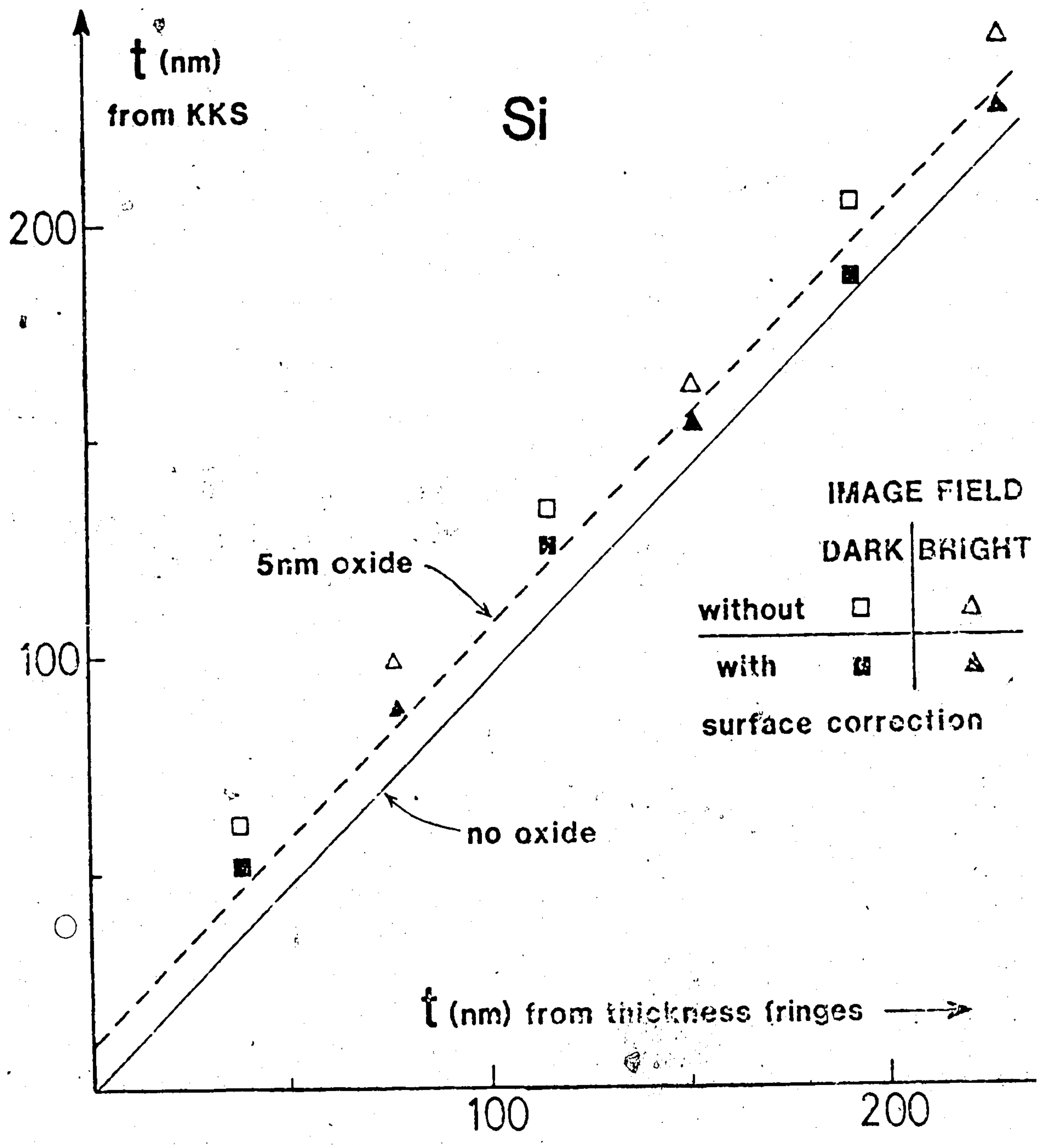

Fig. 5.8. The Kramers-Kronig measurement of local thicknesses of silicon specimens, plotted against local thickness given by the pendellösung fringes. E_o = 100 keV; β = 5.3 mrad. The dashed line represents exact agreement between the two methods, assuming a 5 nm layer of amorphous oxide on each surface.

than two, in which case the accuracy of n is more important.

5.4.3 CARBON

In the case of the semi-metal carbon, the thickness determined by the Kramers-Kronig method was compared with the thickness measured from the K-edge signal of carbon.

The preparation of the carbon films was described in Chapter 4. The following formula was adopted to calculate the thickness of the carbon film from the K-edge signal:

$$t = \frac{A}{N_a \rho \, \sigma_k(\Delta,\beta)} \, \frac{I_k(\Delta,\beta)}{I_\ell(\Delta,\beta)} \qquad (5.38)$$

where A is the atomic weight of the carbon atom; N_a is the Avogadro's number; ρ is the density of carbon; $\sigma_k(\Delta,\beta)$ is the partial cross-sction of the element as before (Chapter 3); and the terms $I_k(\Delta,\beta)$ and $I_\ell(\Delta,\beta)$ are the integrated intensity in the low-loss and the high-loss region of the spectrum as before (Chapter 3), respectively.

In applying Eq. (5.23) to the semi-metal, n^{-2} in Eq. (5.23) should be replaced by the more exact quantity $\mathrm{Re}[1/\epsilon(0)]$, in accordance with Eq. (5.22). In the case of evaporated carbon film, results obtained from the optical measurement, i.e. $\epsilon_1 = 3.0$ and $\epsilon_2 = 2.8$ at $E = 2$ eV

(Hagemann et al. 1974), have been used. This gives $\mathrm{Re}[1/\epsilon] = \epsilon_1/(\epsilon_1^2+\epsilon_2^2) = 0.$[illegible]$8$. However, examination of the $\mathrm{Im}[-1/\epsilon(E)]$ curve for carbon [Fig. 5.9(a)] reveals that the 0-5 eV region contains appreciable intensity, which is only partially included in the integral of Eq. (5.23) if the separation point (intensity minimum) occurs around 5 eV as in the experiments. The thickness will therefore be underestimated unless a suitable correction factor is applied.

Figure 5.10 presents the Kramers-Kronig measurement of local thickness of very thin films of evaporated carbon, plotted against the film thickness determined from the K-ionization edge. The horizontal coordinate represents film thickness determined from the K-ionization edge, taking a 70 eV integration window and (relativistic) hydrogenic partial cross sections, and assuming a film density of 1.9. The vertical coordinate was calculated from Eq.(5.23) with the lower limit of integration set to 8 eV and n^2 set to zero, the resulting thickness being multiplied by a correction factor of 1.5 before subtracting the surface correction: $\Delta t_s = 8$ nm. Deviations of the data points from the dashed line may reflect errors in measurement, in the partial cross section or in the density of amorphous carbon. The coefficient 1.5 is based on the fact that in the region 0-5 eV the integral $\int_0^5 \mathrm{Im}(-1/\epsilon)/E\, dE$ gives about 30% contribution to the integration over the whole energy range [see Fig. 5.9(a)]. No correction would be necessary for

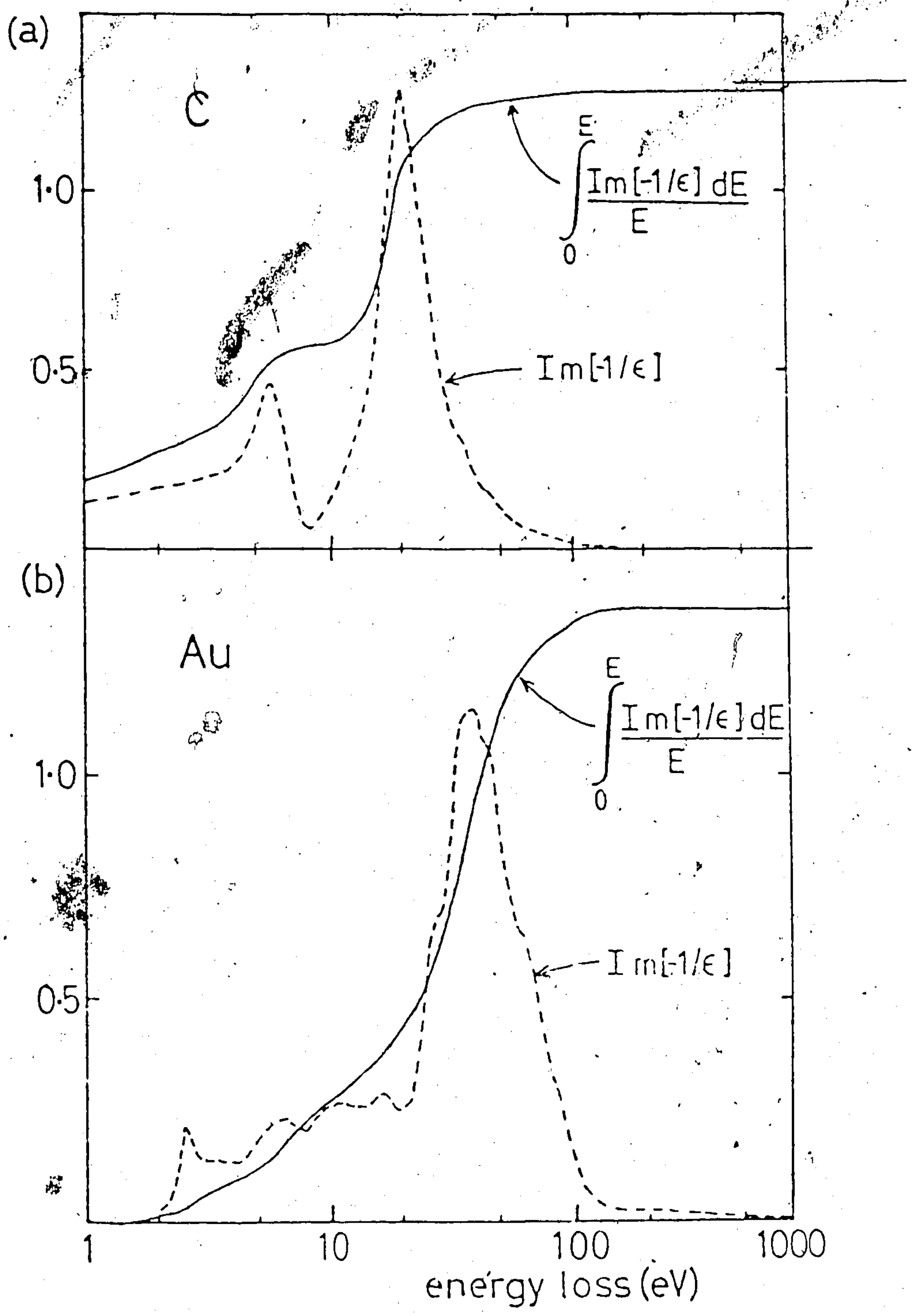

Fig. 5.9. Energy-loss function of (a) evaporated carbon and (b) evaporated gold, deduced from photoabsorption measurement. The solid curves represent the main energy dependence of the integral in Eq. (5.23) neglecting the E-dependence of the logarithmic term.

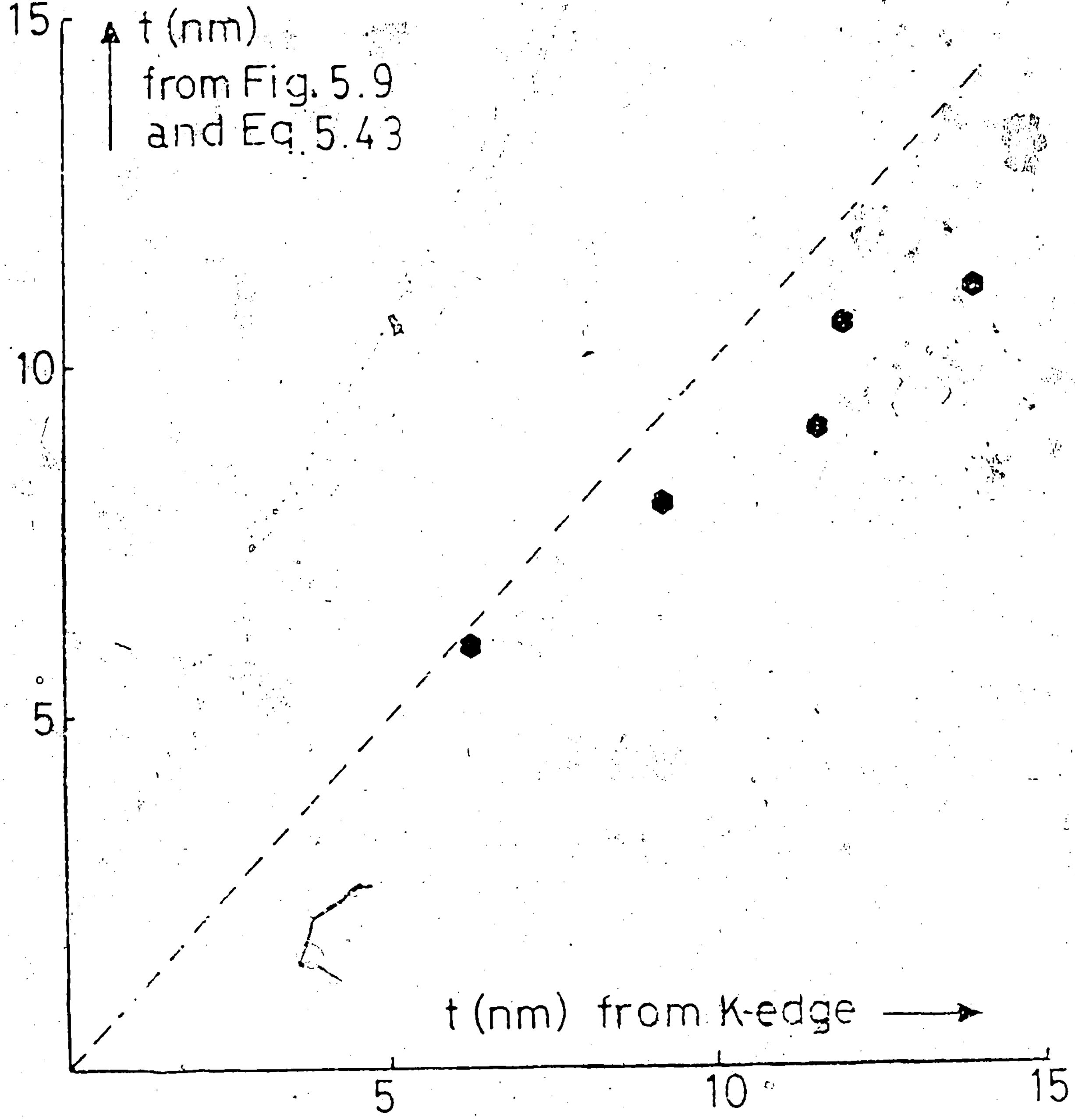

Fig. 5.10. Kramers-Kronig measurement of local thickness of very thin films of evaporated carbon, plotted against the film thickness determined from the K-ionization edge. See the text for details.

measurements performed with a spectrometer system (using, for example, a field-emission source) having sufficient energy resolution to give an intensity minimum below 2 eV.

The requirement for good energy resolution can be relaxed in the case of a metal, where ϵ_1 and ϵ_2 are both large below E = 5 eV so that Im($-1/\epsilon$) remains low. In gold, for example, the 1-5 eV region contributes less than 10% to the integral in Eq. (5.23), despite the presence of an energy-loss peak just below 3 eV, as seen in Fig. 5.9(b).

5.5 APPROXIMATIONS

The 1/E weighting factor in Eq. (5.23) ensures that the contribution of plural scattering to the integral is modest for $t<\lambda$, λ being the total-inelastic mean free path as before (50-150 nm for E_0 = 100 keV and typical values of β). This consideration suggests that the raw spectral intensity J(E) might be used in Eq. (5.23), in place of the single-scattering distribution S(E), together with a correction factor C which makes approximate allowance for plural scattering. In other words:

$$t \simeq \frac{2a_0T}{CI_0(1-n^{-2})} \int_0^\infty \frac{J(E)}{E \log_e(\beta/\theta_E)} \, d(E) \qquad (5.39)$$

where the reasonable additional assumption that $\beta^2/\theta_E^2 >> 1$ over the energy range where J(E)/E is significant has been made. The integral in Eq. (5.39) excludes the zero-loss intensity but includes an estimate of the inelastic contribution beneath the zero-loss peak, obtained by linear or cosine-bell interpolation below the first minimum.

A suitable correction factor C can be deduced by assuming S(E) to be sharply peaked at an energy E_p, as in the free-electron plasmon model (Egerton 1986):

$$C \simeq 1 + 0.3(t/\lambda) = 1 + 0.3\log_e(I_t/I_o) \qquad (5.40)$$

$$\text{for } t/\lambda < 1.2.$$

Table 5.2 gives the film thickness measured by weighing and by applying the Kramers-Kronig sum rule without and with the approximations. The use of Eqs.(5.39) and (5.42), rather than Eq. (5.23), removes the need for deconvolution and results in less than 10% change in measured thickness, for $t<150$ nm and $E_o = 100$ keV (see 3rd and 4th columns of Table 5.2).

Another possible simplification arises from the fact that correction of a spectrum for surface-mode scattering produces a decrease Δt_s in estimated thickness which appears to be independent (within our experimental error) of the specimen material and thickness [Figs. 5.2(a)-5.2(f)] and only slightly dependent on the collection angle and incident

Table 5.2. Film thickness measured by weighing (t_w) and by applying the Kramers-Kronig sum rule, without (t_1) and with (t_2) a correction for surface scattering and without and with the approximations

Film	Weighted	t_1(nm)		t_2(nm)	
	t_w(nm)	Eq. (5.23)	Eq. (5.39)	Eq. (5.32)	Eq. (5.41)
Al	20	28	27	19	19
	41	45	44	37	38
	73	81	77	70	69
	133	143	157	135	149
Cr	14	22	22	14	14
	39	62	64	54	56
	56	75	74	66	66
Cu	30	42	41	33	33
	59	72	72	63	63
Ni	14	26	25	19	17
	35	42	42	38	34
	38	52	50	42	42
Ag	24	37	36	26	28
	30	43	42	32	34
	53	65	65	55	53
Au	10	19	18	9	10
	33	41	40	33	32
	47	53	54	48	46

energy (Figs. 5.3 and 5.4). The local thickness of the sample may therefore be taken as:

$$t \simeq t_1 - \Delta t_s \tag{5.41}$$

where t_1 is the first estimate of thickness (ignoring surface effects) obtained from Eq. (5.23) or Eq. (5.39). An average over the results obtained from the metal films listed in Table 5.2 (for β = 5.3 mrad, E_0 = 100 keV) gives Δt_s = (8.4±1.6) nm, which can be taken as 8 nm for practical purposes.

The use of Eqs. (5.39) and (5.41) avoids both deconvolution and Kramers-Kronig analysis, allowing the data processing to be reduced to a few lines of computer code (see Appendix B). For $t/\lambda<1.2$, the accuracy of thickness determination does not appear to be significantly worse in comparison with the more exact procedure (compare columns 2, 5 and 6 of Table 5.2).

5.6 CONCLUSIONS

It has been shown how to apply the Kramers-Kronig sum rule to measure the absolute local thickness of a TEM specimen without knowing an inelastic mean free path. For 100 keV incident energy, the accuracy obtainable is typically ±10% or ±2 nm (whichever is larger) over the thickness range 10-200 nm. The fast-Fourier transform technique has been used to reduce the computing time required for deconvolution (to derive the single-scattering distribution) and for Kramers-Kronig analysis (to estimate the surface-scattering intensity). For film thicknesses below 100 nm, the use of a correction factor to allow for plural scattering and an experimentally based surface-scattering correction reduce the computing requirements even further without significant loss of accuracy. The measurements can be made on very small areas (e.g. 10 nm diameter), the radiation dose being low in comparison with those need to apply the continuum (Hall) method to an X-ray emission spectrum.

BIBLIOGRAPHY

Ahn,C.C. and O.L. Krivanek (1986). In: *44th Ann. Proc. Electron Microsc. Soc. Amer.*, ed. G.W. Bailey (San Francisco Press, San Francisco), 618.

Berriman,J., R.K. Bryan, R. Freeman and K.R. Leonard (1984). *Ultramicroscopy* 13, 351.

Bethe,H. (1930). *Ann. Physik* 5, 325.

Blackstock,A.W., R.H. Richie and R. Birkhoff (1955). *Phy. Rev.* 100, 1078.

Blois,M.S. and L.M. Rieser (1954). *J. Appl. Phys.* 25, 338.

Burge,R.E. and D.L. Misell (1968). *Phil. Mag.* 18, 251.

Cann,C.D. (1973). *Ph. D. Thesis*, University of Alberta.

Castro-Fernandez,R.F., C.M. Sellars and J.A. Whiteman (1985). *Phil. Mag.* A 52, 289.

Chen,C.H. (1976). *J. Phys. Solid State Phys.* 9, L321.

Cheng,S.C. (1983). *M. Sc. Thesis*, University of Alberta.

Cheng,S.C. (1987). *Ultramicroscopy*, 21, 291.

Cheng,S.C. and R.F. Egerton (1985). *Ultramicroscopy* 16, 279.

Cheng,S.C. and R.F. Egerton (1986). In: *44th Ann. Proc. Electron Microsc. Soc. Amer.*, ed. G.M. Bailey (San

Francisco Press, San Francisco), 716.

Cheng,S.C., P.A. Crozier and R.F. Egerton (1987). *J. Microsc.*, accepted.

Chopra,K.L. (1969). *Thin Film Phenomena* (McGraw-Hill, New York), 189.

Colliex,C. and C. Mory (1984). In: *Quantitative Electron Microscopy*, ed. J.N. Chapman and A.J. Craven (SUSSP Publications, Edinburgh), 149.

Colliex,C., M. Gasgnier and P. Trebbia (1976). *J. de Physique* 37, 397.

Cooley,J.W. and J.W. Tukey (1965). *Math. Comput.* 19, 297.

Craven,A.J. and T.W. Buggy (1984). *J. Microsc.* 136, 227.

Crewe,A.V., J.P. langmore and M. Isaacson (1975). In: *Physical Aspect of Electron Microscopy and Microbeam Analysis*, eds. B.M. Siegel and D.R. Beaman (Wiley, New York), 47.

Crozier,P.A. and R.F. Egerton (1986). In: *44th Ann. Proc. Electron Microsc. Soc. Amer.*, ed. G.W. Bailey (San Francisco Press, San Francisco), 714.

Daniels,J., C.V. Festenb[illegible] H. Raether and K. Zeppenfeld (1970). In: *Springer Tracts in Modern Physics* 54, 78 (Springer-Verlag, New York).

Disko,M.M. (1981). In: *Analytical Electron Microscopy--1981*, ed. R.H. Geiss (San Francisco Press, San Francisco), 214.

Disko,M.M. (1986). In: *Microbeam Analysis*, ed. A.D. Romig Jr and W.F. Chambers (San Francisco Press, San Francisco), 429.

Egerton,R.F. (1975). *Phil. Mag.* 31 199.

Egerton,R.F. (1978a). *Ultramicroscopy* 3, 243.

Egerton,R.F. (1978b). *Ultramicroscopy* 3, 39.

Egerton,R.F. (1979). *Ultramicroscopy* 4, 169.

Egerton,R.F. (1980). *In:* 38th Ann. Proc. Electron Microsc. Soc. Amer., ed. G.W. Bailey (Claitor's Publishing, Baton Rouge, Louisiana), 130.

Egerton,R.F. (1982). In: *Microbeam Analysis--1982*, ed. K.F.J. Heinrich (San Francisco Press, San Francisco, 1982), 43.

Egerton,R.F. (1986). *Electron Energy-Loss Spectroscopy in the Electron Microscope* (Plenum, New York).

Egerton,R.F. and S.C. Cheng (1982). *J. Microsc.* 127, RP3.

Egerton,R.F. and S.C. Cheng (1985). In: *43rd Ann. Proc. Electron Microsc. Soc. Amer.*, ed. G.W. Bailey (San Francisco Press) 398.

Egerton, R.F. and S.C. Cheng (1987). *Ultramicroscopy*, 21, 231.

Egerton, R.F. and P.A. Crozier (1985). In: *44th Ann. Proc. Electron Microsc. Soc. Amer.*, ed. G.W. Bailey (San Francisco Press), 620.

Egerton, R.F. and P.A. Crozier (1987). *Ultramicroscopy*, submitted.

Egerton, R.F. and M.J. Whelan (1974). *Phil. Mag.* 30, 739.

Egerton, R.F., J. Philips and M.J. Whelan (1975). In: *Development in Electron Microscopy and Microanalysis*, ed. J. Venables (Acad.Press, London), 137.

Egerton, R.F., B.G. Williams and T.G. Sparrow (1985). *Pro. Roy. Soc. Lond.*, **A398**, 395.

Egerton, R.F., S.C. Cheng and T. Malis (1987). In: *45th Ann. Proc. Electron Microsc. Soc. Amer.*, to be published.

Gatan, Inc., *Instruction Manual for Electron Energy Loss Spectrometer, Model 607* (Pittsburgh).

Hagemann, H.-J., W. Gudat and C. Kunz (1974). *DESY Report SR-74/7*, DESY, 2 Hamburg 52, W. Germany.

Hall, T.A. and B.J. Gupta (1983). *Quarterly Reviews of Biophysics* **16**, 279.

Henoc,J. (1980). In: *Microanalysis Scanning Electron Microscopy*, eds. F. Maurice, L. Meny and R. Tixier (Les éditions de physique, Orsay), 121.

Higgins,R.J. (1976). *Amer. J. of Phys.* **44**, 766.

Hirsch,P.B., A. Howie, R.B. Nicholson, D.W. Pashley and M.J. Whelan (1977). *Electron Microscopy of Thin Crystals* (Krieger, Huntington, New York).

Horstmann,H. and G. Meyer (1961). *Z. Phys.* **164**, 21.

Inokuti,M. (1971). *Rev. Mod. Phys.* **43**, 297. Addenda: *Rev. Mod. Phys.* **50**, 23.

Isaacson,M. (1972). *J. Chem. Phys.* **56**, 1803.

Isaacson,M., M. Ohtsuki and M. Utlaut (1979). In: *Introduction to Analytical Electron Microscopy*, eds. J.J. Hren, J.I. Goldstein and D.C. Joy (Plenum Press, New York), 343.

Isaacson,M. and M. Scheinfein (1985). In: *43rd Ann. Proc. Electron Microsc. Soc. Amer.*, ed. G.W. Bailey (San Francisco Press), 396.

Jackson,J.D. (1962). *Classical Electrodynamics*, 2nd ed. (John Wiley & Sons, New York).

Johnson,D.W. (1974a). In: *Electron Microscopy--1974* (8th Int. Congress, ed. J.V. Sanders and D.J. Goodchild, Australian Academy of Science, Canberra, 1974), 388.

Johnson,D.W. (1974b). *Ph. D. Thesis*, Melbourne.

Johnson,D.W. (1975). *J. Phys. A : Math. Gen. Phys.* 8, 490.

Johnson,D.W. and J.C.H. Spence (1974). *J. Phys. D : Appl. Phys.* 7, 771.

Jouffrey,B. and J. Sevely (1976). *Revue de Physique Appliqueé*, 11, 101.

Joy,D.C. (1979). In: *Introduction to Analytical Electron Microscopy* (Plenum Press, New York), 223.

Joy,D.C. and D.M. Maher (1980). In: *Scanning Electron Microscopy--1980, part 1* (SEM Inc., A.M.F. O'Hare, Illinois), 25.

Keil,P. (1968). *Z. Phys.* **214**, 266.

Kelly,P.M., A. Jostens, R.G. Blake and J.G. Napier (1975). *Phys. Stat. Sol. A* 31, 771.

Kihn,Y., J.-P. Perez, J. Sevely, G. Zanchi, and B. Jouffrey (1980). In: *Electron Microscopy--1980* (7th European Congress Foundation, the Hague), **4**, 42.

Kittel,C. (1976). *Introduction to Solid State Physics*, 5th ed. (John Wiley & Sons, New York).

Kloos,T. (1973). *Z. Phys.* **265**, 225.

Koppe,H. (1948). *Z. Phys.* **124**, 648.

Krivanek,O.L. and P.R. Swann (1981). In: *Quantitative Microanalysis with High Spatial Resolution* (The Metals Society, London), 136.

Kunz,C. (1966). *Z. Phys.* **196**, 311.

Landau,L.D. and E.M. Lifshitz (1960). *Electrodynamics of Continuous Media* (Pergamon Press, Oxford).

Leapman,R.D. (1982). In: *Microbeam Analysis--1982*, ed.K.F.J. Heinrich (San Francisco Press, San Francisco), 111.

Leapman,R.D., C.E. Fiori and C.R. Swyt (1984). *J. Microsc.* **133**, 239.

Lenz,F. (1954) *Z. Naturforsch.* **9A**, 185-204.

Maher,D.M. (1979). In: *Introduction to Analytical Electron Microscopy*, eds. J.J. Hren, J.I. Goldstein and D.C. Joy, (Plenum Press, New York), 259.

Malis,T., S.C. Cheng anf R.F. Egerton (1987). *J. of Electron Microscopy Technique*, submitted.

Hosoi,J., T. Oikawa, M. Inoue, Y. Kokubo and K.Hama (1981). *Ultramicroscopy* 7 147.

Munoz,R. (1983). *M. Sc. Thesis*, University of Alberta.

Oikawa,T, J. Hosoi, M. Inoue and T. Honda (1984). *Ultramicroscopy* **12**, 223.

Perez,J.-P, J. Sevely and B. Jouffrey (1977). *Phys. Rev. A*

16, 1061.

Philipp,H.R. and H. Ehreneich (1963). *Phys. Rev.* **129**, 1550.

Philipp,H.R. and E.A. Taft (1982). *J. Appl. Phys.* **53**, 5224.

Rae,D.A., V.D. Scott and G. Love (1981). In: *Quantitative Microanalysis with High Spatial Resolution* (The Metals Society, London), 57.

Raether,H. (1980). *Springer Tracts in Modern Physics*, vol. 88 (Springer-Verlag, New York).

Reed,S.J. (1972). *J. Phys. E.: Sci. Instrum.* 5, 994.

Reimer,L. (1984). *Transmission Electron Microscopy* (Springer Series in Optical Sciences, No. 36; Springer-Verlag, New York).

Ritchie,R.H. (1957). *Phys. Rev.* **106**, 874.

Ruark,A.E. and F.E. Brammer (1937).*Phys. Rev.* **52**, 3.

Scheinfein,M. and M. Isaacson (1984). In: *Scanning Electron Microscopy*, part 4, 1681.

Schnatterly,S.E. (1979). In: *Solid State Physics* (Academic Press, New York) vol.14, 275.

Shuman,H. (1981). *Ultramicroscopy* **6**, 163.

Spence,J.C.H. (1979). *Ultramicroscopy* **4**, 9.

Spence,J.C.H. (1980). *Experimental High-Resolution Electron*

Microscopy (Oxford University Press, New York).

Spence,J.C.H. (1985). *Ultramicroscopy* **18**, 165.

Spence,J.C.H. and A.E. Spargo (1970). *Physics Letters* **33A**, 116.

Spence,J.C.H. and A.E. Spargo (1971). *Phys Rev. Letters* **26**, 895.

Swanson,N. and C.J. Powell (1966). *Phys. Rev.* **145**, 195.

Swyt.C.R. and R.D. Leapman (1984). In: *Microbeam Analysis--1984*, eds. A.D. Romig and J.I. Goldstein (San Francisco Press, San Francisco, 1984), 45.

Tonomura,A. and H. Watanabe (1967). *Jap. J. Appl. Phys.* **6**, 1163.

Trebbia,P. (1979). *Thèse*, Université Paris-Sud.

Wehenkel,C. (1975). *J. de Physique* **36**, 199.

Wolter,A.R. (1965). *J. Appl. Phys.* **36**, 2377.

Zaluzec,N.J. (1980). In: *38th Ann. Proc. Electron Microsc. Soc. Amer.*, ed. G.W. Bailey. (Claitor's Publishing, Baton Rouge, Louisiana), 112.

APPENDIX A

FORTRAN PROGRAM FOR FOURIER-LOG DECONVOLUTION, KRAMERS-KRONIG ANALYSIS AND ITERATIVE SUBTRACTION OF THE SURFACE-SCATTERING INTENSITY

```
C
C     THE DIPOLE APPROXIMATION IS ASSUMED.
C
C     FOR M>MMIN,
C     A GAUSSIAN TAIL AA*EXP(-M*M/S2) OF THE ZERO-LOSS PEAK
C     IS SUBTRACTED FROM THE INELASTIC DATA, TAKING
C     PARAMETER AA AS THE HIGHT OF Z(E) AND S2 FROM AREA
C     A0=SQRT(PI/SQRT(S2)). IN THE REGION M=0 TO MMIN,
C     THE INELASTIC INTENSITY IS TAKEN AS A*X+B*X*X,
C     A AND B BEING FOUND FROM THE KNOWN SLOPE AND
C     INTENSITY AT M=MMIN (THE TRUE MINIMUM IN DATA).
C     ( X = J-1 )
C     ************** VERSION 16OCT85 *********************
C
C     INPUT DATA IS READ FROM A DATA FILE (NAME = D.????
C     IN THE FILE CATALOG) WHOSE FIRST LINE CONTAINS THE
C     FOLLOWING NUMBERS, EACH FOLLOWED BY A COMMA:
C     ND - THE NUMBER OF CHANNELS OF THE SUPPLIED SPECTRUM
C     NN - THE NUMBER OF CHANNELS USED IN FOURIER ANALYSIS
C          (MUST BE OF THE FORM 2**K AND NOT LESS THAN ND)
C     NLINES - THE NUMBER OF LINES OF OUTPUT DATA IN EACH
C              LOOP
C     NLOOPS - THE NUMBER OF ITERATIONS USED TO ESTIMATE
C              THE SURFACE-LOSS INTENSITY
C     EPC - THE ENERGY-LOSS INCREMENT PER CHANNEL
C     E0 - THE INCIDENT-BEAM ENERGY, IN KEV
C     BETA - THE COLLECTION SEMIANGLE, IN MILLIRADIANS
C     R1 - THE REFRACTIVE INDEX OF THE SPECIMEN
C          (FOR A METAL, ENTER A LARGE NUMBER SUCH AS 1000)
C
C     THE SECOND LINE IN THE DATA FILE CONTAINS AN
C     IDENTIFICATION LABEL, WHICH IS PRINTED OUT AT THE
C     TOP OF THE OUTPUT DATA
C
C     SUCCESSIVE LINES OF THE DATA FILE CONTAIN THE
C     EXPERIMENTAL SPECTRUM, IN THE FORM OF INTEGER
C     NUMBERS (CHANNEL COUNTS) EACH FOLLOWED BY A
C     COMMA. TO AVOID LOSS OF DATA POINTS, ND SHOULD
C     BE A MULTIPLE OF TEN.
C
C     TO RUN THE PROGRAM, $RUN FGKKS 5=D.????
C
```

```
      REA[illegible]01) ND,NN,NLINES,NLOOPS,EPC,E0,BETA,RI
  501 FORM[illegible](4I5,4F10.0)
      WRITE(6,501) ND,NN,NLINES,NLOOPS,EPC,E0,BETA,RI
      REAL LABEL(20)
      READ(5,503) LABEL
      WRITE(6,503) LABEL
  503 FORMAT(20A4)
      DIMENSION ID(1024)
      READ(5,502) (ID(I),I=1,ND)
  502 FORMAT(10I8)
      DIMENSION D(2048)
C     FIND FIRST MAXIMUM IN THE DATA ARRAY ID(I):
      IA=0
      NOISE=ID(1)+ID(2)+IABS(ID(1)-ID(2))
      DO 101 I1=1,ND
      IF(ID(I1).LT.NOISE) GO TO 101
      IF (ID(I1).LT.ID(I1-1)) GO TO 102
  101 IA=IA+ID(I1)
  102 NZ=I1-1
C     FIND FIRST MINIMUM AFTER ZERO-LOSS PEAK:
      DO 201 I2=I1,ND
      IF(ID(I2).GT.ID(I2-1)) GO TO 202
  201 IA=IA+ID(I2)
C     REMOVE THE GAIN CHANGE, IF ANY:
  202 DO 204 I3=I2,ND
      IF(ID(I3).LT.9*ID(I3-1)) GO TO 204
      ID(I3-1)=2*ID(I3-2)-ID(I3-3)
  203 ID(I3)=2*ID(I3+1)-ID(I3+2)
      G=FLOAT(ID(I3))/FLOAT(2*ID(I3-1)-ID(I3-2)-ID(1))
      GO TO 205
  204 G=1.
      I3=ND
  205 A0=FLOAT(IA-ID(1)*(I2-1))
      MMIN=2*(I2-NZ)-1
C     (MMIN CORRECTED TO CORRESPOND TO TRUE MINIMUM VALUE)
      MFIN=2*(ND-NZ)+1
      MG=2*(I3-NZ)+1
      MM=2*NN
      DN=FLOAT(ID(ND))*(FLOAT(2*ND
     @    -2*NZ+1)**3)/(FLOAT(MM))**3
C     CALCULATE PARAMETERS OF GAUSSIAN TAIL OF Z(E),
C     ASSUMING:
      AA=FLOAT(ID(I1-1)-ID(1))
      S2=A0*A0/AA/AA/3.14
      X1=FLOAT(MMIN-1)
      G1=AA/EXP(X1*X1/S2)
      B=(G1*(2.*X1*X1/S2+1.)-FLOAT(ID(I2-1)-ID(1))/X1/X1)
      A=G1*2.*X1/S2-2.*B*X1
      WRITE(6,678) A,B
  678 FORMAT(2F10.4)
      DO 302 J=1,MM,2
C     EXTRAPOLATE DATA TO ZERO AT END OF RANGE:
      D(J)=(FLOAT(ID(ND)-ID(1))+DN)*(FLOAT(2*ND-2*NZ+1)**3)
     @     /(FLOAT(J)**3)/G - DN/G -FLOAT(ID(1))
```

```
            IF(J.GE.MFIN) GO TO 302
            IF(J.LE.MMIN) GO TO 301
C           TRANSFER EXPERIMENTAL DATA INTO ARRAY D(J):
            D(J)=FLOAT(ID((J-1)/2+NZ))/G
            IF(J.GE.MG) GO TO 300
C           SUBTRACT ZERO LEVEL AND GAUSSIAN TAIL FROM LOW-E DATA:
            GTAIL=0.
            XX=FLOAT((J-1)*(J-1))/S2
            IF(XX.GT.150)GO TO 299
            GTAIL=AA/EXP(XX)
        299 D(J)=D(J)*G-GTAIL-FLOAT(ID(1))
        300 GO TO 302
C           ADD A*J+B*J*J FUNCTION FROM J=1 TO MMIN:
C       301 D(J)=A*FLOAT(J-1)+B*FLOAT((J-1)*(J-1))
        302 D(J+1)=0.
            WRITE(6,651)
        651 FORMAT('0',
           @'INELASTIC INTENSITY BEFORE DECONVOLUTION:')
            DO 601 I=5,ND,5
        601 WRITE(6,602) D(2*I-9),D(2*I-7),D(2*I-5),D(2*I-3),
           @D(2*I-1)
        602 FORMAT(5(F10.1))
C           PUT DELTA FUNCTION IN FIRST CHANNEL OF SHIFTED ARRAY:
            D(1)=A0
            CALL FFT(NN,+1,D)
C           PROCESS FOURIER COEFFICIENTS, REMOVING PHASE
C           DISCONTINUITIES:
            NPI=0
            THP=0.
            DO 403 I=1,MM,2
            TH=ATAN(D(I+1)/D(I))
            DTH=TH-THP
            THP=TH
            IF(DTH.LT.1.57)GO TO 401
            NPI=NPI+1
        401 IF(DTH.GT.-1.57) GO TO 402
            NPI=NPI-1
        402 TH=TH-FLOAT(NPI)*3.14159265
            D(I)=(0.5*A0*ALOG(D(I)*D(I)+D(I+1)*D(I+1))
           @      -A0*ALOG(A0))/FLOAT(NN)
            D(I+1)=A0*TH/FLOAT(NN)
C           (DIVIDING BY NN CORRECTS FOR SCALING FACTOR IN
C           INVERSE FFT)
        403 THP=TH
            CALL FFT(NN,-1,D)
            WRITE(6,652)
        652 FORMAT('0',
           @'SINGLE-SCATTERING INTENSITY AFTER DECONVOLUTION:')
            DO 611 I=5,ND,5
        611 WRITE(6,602) D(2*I-9),D(2*I-7),D(2*I-5),D(2*I-3),
           @             D(2*I-1)
            DIMENSION SSD(2048)
            DO 410 J=1,MM
        410 SSD(J)=D(J)
```

```
C     KRAMERS-KRONIG ANALYSIS OF THE SSD, USING THE FFT
C     SUBROUTINE
      DIMENSION DI(1024)
      TGT=E0*(1022.12+E0)/(511.06+E0)
C     APPLY APERTURE CORRECTION APC:
      LOOP=1
   99 SUM=0.
      AREA=0.
      DO 10 J=3,MM,2
      AREA=AREA+D(J)
      E=EPC*FLOAT(J-1)/2.
      APC=ALOG(1.+(BETA*TGT/E)**2)
      D(J)=D(J)/APC
   10 SUM=SUM+D(J)/E
      RK=SUM/1.571/(1.-1./RI/RI)*EPC
      TNM=332.5*RK/(A0*EPC)*E0*(1.+E0/1022.)/(1.+E0/511.)**2
      TOL=AREA/A0
      RLAM=TNM/TOL
      WRITE(6,61) TNM,TOL,RLAM,LOOP
   61 FORMAT('0','THICKNESS= ',F5.1,' NM',4X,'T/LAMBDA= ',
     @       F4.2,4X,'LAMBDA = ',F5.1,' NM',5X,'LOOP ',I2)
C     APPLY NORMALIZATION FACTOR RK AND STORE IMEPS IN
C     ARRAY DI:
      DO 20 J=1,MM,2
      D(J)=D(J)/RK
      D(J+1)=0.
   20 DI((J+1)/2)=D(J)
      CALL FFT(NN,+1,D)
      IM=2*NN-1
      DO 30 I=1,NN
C     TRANSFER SINE COEFFICIENTS TO COSINE LOCATIONS:
      D(2*I-1)=-2.*D(2*I)/FLOAT(NN)
   30 D(2*I)=0.
      DO 40 J=1,NN,2
C     CONVERT FROM AN ODD FUNCTION TO AN EVEN FUNCTION:
   40 D(NN+J)=D(NN+J)
      CALL FFT(NN,-1,D)
      DO 70 J=1,MM,2
C     CORRECT FOR TAIL OF THE REFLECTED PART OF THE EVEN
C     FUNCTION:
   70 D(J)=D(J)+1.-D(NN-1)/2.*(FLOAT(NN-1)/FLOAT(MM-J))**2
      WRITE(6,63)
   63 FORMAT(/' ',5X,'EV',4X,'RE(1/EPS)',3X,'IM(-1/EPS)',
     @      4x,'EPS1',6X,'EPS2',5X,'VOLUME',5X,'SURFACE'/)
      T=E0*(1.+E0/2./511.06)/(1.+E0/511.06)**2
      RK0=2590.*(1.+E0/511.06)*SQRT(2.*T/511.06)
      MLINES=2*NLINES
      DO 80 J=3,MM,2
      EN=FLOAT((J-1)/2)*EPC
      RE=D(J)
      DEN=D(J)*D(J)+DI((J+1)/2)*DI((J+1)/2)
      EPS1=D(J)/DEN
      EPS2=DI((J+1)/2)/DEN
      DEN2=(EPS1*EPS1+EPS2*EPS2-EPS1)**2+EPS2*EPS2
```

```
      SRFELF=4.*EPS2/((1.+EPS1)**2+EPS2*EPS2) - DI((J+1)/2)
      SRFINT=2.*RK/RK0/TNM*(1571.*TGT/EN-1000./BETA)*SRFELF
      D(J)=0.
      D(J+1)=0.
      IF(J.GE.NN) GO TO 44
      D(J)=SSD(J)-SRFINT
   44 IF(J.GE.MLINES) GO TO 46
      WRITE(6,66) EN,RE,DI((J+1)/2),EPS1,EPS2,D(J),SRFINT
   66 FORMAT(F8.1,6(F11.2))
   46 CONTINUE
   80 CONTINUE
      D(1)=0.
      D(2)=0.
      LOOP=LOOP+1
      IF(LOOP.LE.NLOOPS) GO TO 99
      STOP
      END
C
C
      SUBROUTINE FFT(NN,ISIGN,D)
      DIMENSION D(1024)
      N=2*NN
      J=1
      DO 5 I=1,N,2
      IF(I-J)1,2,2
    1 TR=D(J)
      TI=D(J+1)
      D(J)=D(I)
      D(J+1)=D(I+1)
      D(I)=TR
      D(I+1)=TI
    2 M=N/2
    3 IF(J-M)5,5,4
    4 J=J-M
      M=M/2
      IF(M-2)5,3,3
    5 J=J+M
      MM=2
    6 ML=MM-N
      IF(ML)7,10,10
    7 IS=2*MM
      TH=6.283185/FLOAT(ISIGN*MM)
      ST=SIN(TH/2)
      W1=-2.*ST*ST
      W2=SIN(TH)
      WR=1.
      WI=0.
      DO 9 M=1,MM,2
      DO 8 I=M,N,IS
      J=I+MM
      TR=WR*D(J)-WI*D(J+1)
      TI=WR*D(J+1)+WI*D(J)
      D(J)=D(I)-TR
      D(J+1)=D(I+1)-TI
```

```
   D(I)=D(I)+TR
 8 D(I+1)=D(I+1)+TI
   TR=WR
   WR=WR*W1-WI*W2+WR
 9 WI=WI*W1+TR*W2+WI
   MM=IS
   GO TO 6
10 RETURN
   END
```

APPENDIX B

FORTRAN PROGRAM FOR THICKNESS MEASUREMENT BY KRAMERS-KRONIG SUM RULE WITH APPROXIMATE CORRECTION FOR PLURAL SCATTERING AND FOR SURFACE-MODE SCATTERING FOR LARGER THICKNESS

```
C
C      DATA FOR 47NM GOLD FILM, 2EV/CHANNEL, 100KEV, 5.3MRAD
C      COLLECTION:
C
       DIMENSION ID(70)
       ND=70
       EPC=2.
       BETA=5.3
       E0=100
       RI=1000
       DATA ID/1,1,9,381,14393,1805,238,238,222,234,263,258,
      @359,302,294,288,409,459,482,386,425,499,468,426,454,
      @409,396,365,334,352,282,332,311,296,292,251,278,285,
      @241,248,205,216,218,206,216,199,188,168,157,164,145,
      @121,127,128,115,118,124,82,107,94,82,86,91,76,82,61,
      @52,57,56,57
C
C      ESTIMATE INSTRUMENTAL BACKGROUND LEVEL AND ASSOCIATED
C      NOISE:
       IB=(ID(1)+ID(2))/2
       NOISE=IB+1+IFIX(SQRT((FLOAT(16*IB))))
C      FIND FIRST MAXIMUM IN THE DATA ARRAY ID(I)
       IA=0
       DO 101 I1=1,ND
       IF (ID(I1).LE.NOISE) GO TO 101
       IF (ID(I1).LE.ID(I1-1)) GO TO 102
   101 IA=IA+ID(I1)
   102 NZ=I1-1
C      FIND FIRST MINIMUM AFTER ZERO-LOSS PEAK:
       DO 201 I2=I1,ND
       IF (ID(I2).GT.ID(I2-1)) GO TO 205
   201 IA=IA+ID(I2)
   205 NSEP=I2-1
       ESEP=FLOAT(NSEP-NZ)*EPC
       AO=FLOAT(IA-IB*NSEP)
C      LINEAR INTERPOLATION FROM NZ TO NSEP:
       DO 301 I=NZ,NSEP
   301 ID(I)=IB+(ID(NSEP)-IB)*(I-NZ)/(NSEP-NZ)
       TGT=E0*(1022.12+E0)/(511.06+E0)
C      ALLOW FOR E**-3 EXTRAPOLATED INTENSITY:
       SUM=FLOAT(ID(ND)-IB)/ALOG(BETA*TGT/(ND-NZ)/EPC)/3./EPC
       AL=FLOAT((ID(ND)-IB)*(ND-NZ))/2.
```

```
C       APPLY KRAMERS-KRONIG SUM RULE:
        DO 15 I=I1,ND
        E=EPC*FLOAT(I-NZ)
        APC=ALOG(BETA*TGT/E)
        SUM=SUM+FLOAT(ID(I)-IB)/E/APC
     15 AI=AI+FLOAT(ID(I)-IB)
        TOL=ALOG((AI+A0)/A0)
        C=1.+0.3*TOL
        TKEV=E0*(1.+E0/1022.)/(1.+E0/511.)**2
        TNM=105.8*TKEV/C/A0/(1.-1./RI/RI)*SUM-8.
        RLAM=TNM/TOL
        WRITE(6,61) TNM,TOL,RLAM,ESEP
     61 FORMAT('0',' T=' ,f5.1,'NM',3X,'T/LAMBDA= ',F4.2,3X,
       @'LAMDA = ',F5.1,'NM',3X,'SEPARATION POINT=',F4.1,'EV')
        STOP
        END
 T= 47.3NM T/LAMBDA=0.68 LAMBDA=69.4NM SEPARATION POINT=8.0EV
```